Population Fluctuations, Nonequilibrium Flows and Instabilities in Some Model Systems

By

Somdeb Ghose

PHYS10200605010

The Institute of Mathematical Sciences, Chennai

A thesis submitted to the

Board of Studies in Physical Sciences

In partial fulfillment of requirements

For the Degree of

DOCTOR OF PHILOSOPHY

of

HOMI BHABHA NATIONAL INSTITUTE

July, 2013

Certificate will be Upload soon.

STATEMENT BY AUTHOR

This dissertation has been submitted in partial fulfillment of requirements for an advanced degree at Homi Bhabha National Institute (HBNI) and is deposited in the Library to be made available to borrowers under rules of the HBNI.

Brief quotations from this dissertation are allowable without special permission, provided that accurate acknowledgement of source is made. Requests for permission for extended quotation from or reproduction of this manuscript in whole or in part may be granted by the Competent Authority of HBNI when in his or her judgement the proposed use of the material is in the interests of scholarship. In all other instances, however, permission must be obtained from the author.

Somdeb Ghose

DECLARATION

I, hereby declare that the investigation presented in the thesis has been carried out by me. The work is original and has not been submitted earlier as a whole or in part for a degree / diploma at this or any other Institution / University.

Somdeb Ghose

DEDICATIONS

To my uncle, Sushil Kumar Banerjee. This is for you Dada.

ACKNOWLEDGEMENTS

If Jorge Cham's PhD Comics are to be believed, then the life of a graduate student is one of endless misery controlled by a satanic overlord, the Supervisor! Somehow, I have trouble believing this, for my own experiences have taught me that the exact opposite is true. In Ronojoy Adhikari I have found a friend, philosopher and (literally) guide, who has, over the past few years, somehow managed to tolerate me and my idiosyncrasies which generally involve lavish doses of procrastination. He has been there through thick and thin, skillfully guiding me through the wonderful journey-quest that has resulted in this hundred-odd page document. His expertise in the research and teaching of physics is evidenced by his patience and skill in explaining complex concepts in extremely simple ways, and his ability to find a novel and exciting way to solve a problem. The energy and enthusiasm that he brings to the study of physics is infectious, and has been a great boon for me over the years. He has also been a steady support at the personal level, and I am forever grateful for the support and encouragement during my father's medical crisis. Thank you, Ronojoy, for being such a wonderful guide and a friend.

Special thanks must go to G. Baskaran, R. Simon, P. Ray, G. Date, S. Sunder, S. R. Hassan and S. Saurabh for tips, suggestions, criticisms and analytical remarks. I have benefited greatly from these interactions. My collaborations with P. B. Sunil Kumar and A. Dua have been greatly enjoyable and stimulating, and has been extremely fruitful for my research. I have learnt a lot from all of you, and I thank you all for that.

I would like to thank my fellow students for their steadfast friendship and support throughout my stay at IMSc. I have greatly benefited from fun and stimulating discussions, both of the academic and non-academic varieties, with Sandeep Goyal, Rajeev Singh, Prem Prakash Pandey, P.V. Sriluckshmy, Amit K. Bhattacharjee, Abhrajit Laskar, Anoop

Varghese, Rohan Poojary, Madhushree Basu, Kavita Gangal, Soumyajit Pramanick, A. B. Belliappa, Jalpa Soni, Sayantan Ghosh, Gayathri Jayaraman, Rajesh Singh, Karteek Sreenivasaiah and Neeldhara Misra, among many others. Thanks to you, it has been equally fantastic, brilliant and cool!

I would also like to thank my physics teachers from Presidency College for a rewarding three years of bachelor studies, as well as those from South Point High School and MBSV school for the first dozen years of academics. I owe a lot to Partha Pratim Ray and Mallar Ray, teachers at South Point, for their inspirational teaching of physics. Special thanks to Arnab Roy, Shamashis Sengupta, Indrani Chakroborty, Manjari Gupta and Rakhi Paul for the physics and the fun at Presidency College. Special thanks also to Johnny Cage for being there.

Finally, I must thank my father for instilling in me a scientific curiosity from early childhood, my uncle for helping hone my mathematical skills, my aunt for her untiring love and support, and my mother for being a superhero! Saludo!

LIST OF PUBLICATIONS

This thesis is based on the following publications.

Published

1. **Ghose, S.** and Adhikari, R. (2010). *Endogenous Quasicycles and Stochastic Coherence in a Closed Endemic Model*. Physical Review E, **82**, 021913. Arxiv Preprint, 1007.3068.

2. Saha, S., **Ghose, S.**, Adhikari, R. and Dua, A. (2011). *Nonrenewal Statistics in the Catalytic Activity of Enzyme Molecules at Mesoscopic Concentrations*. Physical Review Letters, **107**, 218301. Arxiv Preprint, 1110.6044.

3. Jayaraman, G., Ramachandran, S., **Ghose, S.**, Laskar, A., Saad Bhamla, S., Sunil Kumar, P.B. and Adhikari, R. (2012). *Autonomous Motility of Active Filaments due to Spontaneous Flow-Symmetry Breaking*. Physical Review Letters, **109**, 158302. Arxiv Preprint, 1204.1416.

4. **Ghose, S.** and Adhikari, R. (2014). *Irreducible Representations Of Oscillatory And Swirling Flows In Active Soft Matter*. Physical Review Letters, **112**, 118102. Arxiv Preprint, 1308.1369

In Preparation

1. **Ghose, S.**, Jayaraman, G., Laskar, A., Sunil Kumar, P.B. and Adhikari, R. (2013). *Stokesian hydrodynamics of chemomechanically active filaments*. In preparation.

List of corrections and changes as suggested by the Thesis and Viva Voce Examiners

Synopsis

- Corrected typos.
- Changed the symbol Υ for vortlet to Ψ to conform to rest of thesis.

Chapter 3, Nonrenewality and molecular memory in enzyme kinetics due to intrinsic noise

- Section 3.1, page 36 : Added explanation of Lineweaver-Burk plot.
- Section 3.1, page 37 : Typo fixed. "An important exception is in glycolysis where ~~substrate~~ **enzyme** concentrations exceed those of ~~enzymes~~ **substrates**"
- Section 3.2, page 38, right after Eq 3.4 : "This is a linear master equations, and can ~~theoretically~~ **, in principle,** be solved analytically."
- Section 3.6, page 45, right after Eq 3.6 : Added text defining the Fano factor.
- Section 3.6, page 46, right after Eq 3.8 : Added text regarding the signs of the memory indicators.

Chapter 4, Oscillations in an epidemic model due to intrinsic noise

- Section 4.6, page 70 : The necessity of the violation of detailed balance for the existence of quasicyles has been observed earlier in predator-prey systems : text and reference added to this regard.

Chapter 5, Irreducible representations of active matter flows

- Section 5.4, page 82 : "The constraints imposed by incompressibility, biharmonicity and spherical symmetry imply that only ~~a few~~ **the first three** irreducible parts contribute."

- Section 5.4, page 82 : "This requires us to enumerate all **rank** 3 irreducible multipoles $p \leq 2$ and the **rank** 4 pseudoseptorial multipole for $p = 3 \ldots$"

- Section 5.4, page 82 : Text added to explain why only the pseudoseptor for $p = 3$ is required.

- Fixed typo after Eq. 5.19, page 88.

- Section 5.10, page 96 : Fixed typos in Eq. 5.36.

- Section 5.11, page 96 : References added after "Symmetric states of active stress have been considered previously in the literature ..."

- Section 5.11, page 97 : References and text added with respect to antisymmetric stresses in passive nematics.

Chapter 6, Instabilities of active and sedimenting passive filaments

- Section 6.2, page 102, right after Eq. 6.4 : Added text to explain long-range order.

- Section 6.3, page 104 : Lowercase **r** appears twice, once in Eq. 6.10 and once just abve it. That should be uppercase **R**. Fixed.

- Section 6.3, page 104, right after Eq. 6.11 : Reworded to clarify relation between κ and ϵ. Using this relation, κ is used instead of ϵ in the sequel.

- Section 6.5, page 108, just before Eq. 6.22 : "... denotes small displacements from the ~~fixed point~~ **steady state** ...".

Chapter 7, Conclusions

- Page 115, reworded : "In the continuum limit, ~~this can lead to~~ **the irreducible formalism can be used for** the study of marangoni effects in active interfaces and active drops."

Appendix A

- Page 117 : Added text explaining why index notations are provided in the appendix.

References

- Fixed formatting errors in and updated (where necesary) References 47, 49, 51, 52, 65.

The corrections and changes suggested by the Thesis and Viva Voce Examiners have been incorporated in the thesis.

Guide

Contents

Synopsis 1

List of Figures 9

1 Introduction 11

2 Mathematical preliminaries 19

2.1 Stochastic preliminaries 19

2.1.1 Counting and point processes 19

2.1.2 Markov processes 21

2.1.3 The master equation 22

2.1.4 Steady state, detailed balance and cyclic balance 23

2.1.5 Solutions of birth-death master equation 24

2.2 Hydrodynamic preliminaries 25

2.2.1 Equation of motion of viscous fluid 25

2.2.2 Boundary integral formulation of Stokes equation 27

I Stochastics 31

3 Nonrenewality and molecular memory in enzyme kinetics due to intrinsic noise 35

3.1 Michaelis-Menten enzyme kinetics 36

3.2 Michaelis-Menten stochastic analysis 37

3.3 First-order distributions 39

3.4 Moments of first-order distributions . . . 41
3.5 Second-order distributions and memory . . . 43
3.6 Antibunching of intervals and memory indicators . . . 44
3.7 Slowing down of kinetics . . . 47
3.8 Validity of PFO kinetics . . . 48
3.9 Conclusion . . . 49

4 Oscillations in an epidemic model due to intrinsic noise 51
4.1 Mathematical modelling of epidemics . . . 52
4.2 SIRS linear deterministic analysis . . . 53
4.3 SIRS linear stochastic analysis . . . 57
4.4 Noise-induced oscillations: Endogenous Quasicycles . . . 62
4.5 Quality of noise-induced oscillations: Stochastic coherence . . . 66
4.6 Detailed balance violation necessary for quasicycles . . . 69
4.7 Non-normality increases variance . . . 71
4.8 Conclusion . . . 72

II Hydrodynamics 75

5 Irreducible representations of active matter flows 77
5.1 Chemomechanically active flows around swimming microorganisms . . . 78
5.2 Boundary integral representation of Stokes equation . . . 79
5.3 Expansion of surface stress in irreducible Cartesian basis . . . 80
5.4 Fundamental irreducible components of active Stokes flow . . . 82
5.5 Visualization of uniaxially parametrized multipolar flows . . . 84
5.6 Relation between surface stress and velocity multipoles . . . 85
5.7 Irreducible description of active particle motion . . . 89
5.8 Power dissipated into the fluid . . . 90
5.9 Oscillatory flows around Chlamydomonas . . . 91
5.10 Swirling flows . . . 94

5.11 Active stress densities 96
5.12 Conclusion 97

6 Instabilities of active and sedimenting passive filaments **99**
6.1 Stokes flow due an active filament 99
6.2 Equation of motion for an active filament 101
6.3 Continuum equation of motion in the free-draining approximation 103
6.4 Hydrodynamic interactions necessary for active filament oscillations . . . 105
6.5 Linearized discrete equation of motion of an active filament 107
6.6 Spectral analysis of a passive sedimenting filament 108
6.7 Conclusion 111

7 Conclusions **113**

A Useful ingredients **117**
A.1 Cartesian to spherical polar unit vector transformations 117
A.2 Green's function and derivatives 119
A.3 Definitions and embeddings of irreducible stress multipoles 120
A.4 Active Stokes flow relations in index notation 121

Bibliography **123**

List of Figures

3.1 Stochastic trajectory for $N = 2$ enzymes. 39

3.2 Nonrenewality of multienzyme kinetics due to nonidentical distribution of waiting times. 40

3.3 Multiexponentiality of the distribution of the first waiting times. 40

3.4 Comparison between numerics and analytics for turnover times. 41

3.5 Breakdown of Michaelis-Menten kinetics for multiple enzymes. 42

3.6 Convergence of multienzyme kinetics to single enzyme behaviour for large values of $k_a = k_1 S$. 42

3.7 Breakdown of the MM equation for multienzyme kinetics, demonstrated by first moments of higher turnover times. 43

3.8 Anticorrelation of intervals and nonindependence of joint distributions. . 44

3.9 Variation of anticorrelation with N measure using memory indicators. . . 45

3.10 Slowing down of multienzyme kinetics. 47

3.11 Validity of the pseudo-first-order approximation. 48

4.1 Underdamped and overdamped decay of perturbations in deterministic system. 55

4.2 Plot of $|\mathrm{Im}(\lambda)/\mathrm{Re}(\lambda)|$ of the linearized Jacobian matrix $\mathbf{A}$ against the dimensionless parameters β/γ and α/γ. 56

4.3 Numerical simulation of susceptibles overlaid on deterministic underdamped decay. 57

4.4 Normalized power spectral density for susceptibles and infected. 64

4.5 Normalized autocorrelation of susceptibles and infected. 65

4.6 Quality factor for the susceptibles plotted against population size Ω (main panel) and against Ω^{-1} (inset). 67

4.7 Coefficient of Variation for the susceptibles plotted against population size Ω (main panel) and against Ω^{-1} (inset). 68

4.8 Absolute value of the ratio of the imaginary and real parts of the eigenvalues of the linearized Jacobian matrix plotted against population size. . 69

4.9 Enhanced variance of time-traces of S and I 72

5.1 Fundamental irreducible active flows due to the stresslet, the potential dipole and the septlet. 86

5.2 Swirling flows due to the irreducible vortlet and spinlet. 87

5.3 Cross-sections of long-range hydrodynamic flows around a spherical active particle of radius a generated by a linear combination of time-dependent stresslet $\mathbf{S}$, potential dipole $\mathbf{d}$ and septlet $\mathbf{\Gamma}$. 92

5.4 Estimation of the centre of mass velocity of Chlamydomonas reinhardtii. . 93

5.5 Power dissipated and swimming efficiency of Chlamydomonas, computed using a linear combination of a stresslet, a potential dipole and a septlet. . 95

6.1 Variation of the first few eigenvalues of the sedimenting filament with sedimentation number $\mathcal{S}$, plotted for various values of length L. 109

6.2 Bow-shaped fixed point of the sedimenting elastic filament. 110

Synopsis

Living entities perpetually exist away from equilibrium, a condition necessary for the proper functioning of crucial biological and biochemical processes. Tools from nonequilibrium physics are thus ideally suited to the study of such systems. In this thesis, we study nonequilibrium effects in a variety of model systems. In the first part of the thesis, we focus on counterintuitive effects of intrinsic noise as a result of fluctuations in finite-sized populations. We find that, at the macroscale, intrinsic noise can generate and sustain oscillations in a model of epidemic spreading. At the microscale, intracellular biochemical reactions catalyzed by mesoscopic concentrations of enzymes exhibit phenomena that qualitatively differ from those due to a single enzyme or a deterministically large concentration of the same.

In the second part of the thesis, we study the dynamics of microscopic particles in a viscous fluid that are autonomously motile due to the conversion of chemical energy to mechanical motion. Momentum conservation and the lack of inertia at the microscale ensure that the flows around such chemomechanically active particles are force-free and torque-free. We present an intuitive analytical method to study such active flows in terms of its fundamental irreducible components and to reconstruct essential features of flows around various swimming microorganisms using these "atomic" flows. Filaments constructed using a collection of such active particles, interacting through local elastic potentials and nonlocal hydrodynamics, show instabilities that develop into complex flow patterns and result in complicated translational and rotational motions. Stability analysis reveals that

hydrodynamic interactions are crucial for the development of such instabilities. We describe these in greater detail below.

Stochastics

Oscillations in an epidemic model due to intrinsic noise

Infectious diseases have been one of the primary causes of mortality in human beings over the course of history, recent examples being worldwide outbreaks of viral pandemics such as SARS and H1N1. In this light, a mathematical study of the spatiotemporal spread of epidemics in a macroscopic population of susceptible individuals is a problem of great relevance. As early as the middle of the eighteenth century, D. Bernoulli used a nonlinear ordinary differential equation to study the effect of cow-pox inoculation on the spread of smallpox. The susceptible-infected-recovered (SIR) model, proposed by Kermack and McKendrick in the first part of the twentieth century , also utilizes ordinary differential equations and remains one of the classic deterministic models applicable for exceedingly large population sizes. In reality however, population sizes are finite, and the resultant fluctuations can give rise to phenomena which cannot be captured by deterministic mean-field models. This necessitates the use of stochastic models. Bartlett, one of the first to realize this, implemented a stochastic version of the SIR model to describe the observed periodic recurrence of measles.

Here we study a well-known variant of the SIR model where the recovered population have temporary immunity to the endemic disease, and the total population size is finite and remains constant. We write down a stochastic birth-death master equation for this closed, homogeneously mixed SIRS model. Simulating it using exact numerics , we find that the endemic fixed point is unstable to intrinsic noise. This leads to sustained oscillations with asymptotically decaying phases, which distinguishes such oscillations from those due

to external periodic forcing and confirms that these *endogenous quasicycles* arise from purely intrinsic fluctuations. The regularity of these oscillations varies nonmonotonically with the size Ω of the population, being most coherent at some intermediate population value Ω_c. This counterintuitive phenomenon, called stochastic coherence or coherence resonance, has been previously observed in theory and experiment, and could explain the regularity of biological clocks operating in noisy environs, where the presence of a finite amount of noise improves the accuracy of the clock.

In addition to numerics, we have also studied the model analytically within the linear noise approximation . Taking advantage of the conservation of population and the non-zero fixed point value, we marginalize the master equation and carry out a two-stage linearization procedure on our model, reducing it to the standard multivariate Ornstein-Uhlenbeck form, where the linearized drift and diffusion matrices in the resultant Fokker-Planck equation represent the deterministic and stochastic parts of the dynamics respectively. The linear and Gaussian character of the multivariate OU process allows us to predict stochastic behaviour from the deterministic part of the dynamics, in a spirit similar to the Onsager regression method of equilibrium statistical mechanics. Our analysis shows that quasicycles are possible only if the eigenvalues λ of the linearized drift matrix are complex, which is possible only if the system violates the detailed balance condition. This is ensured by endemicity, and we are thus assured of sustained oscillations. We also find that quasicycles can only be reliably detected if the ratio $|\mathrm{Im}(\lambda)/\mathrm{Re}(\lambda)| \sim 1$. The variation of this ratio with system size shows a peak at Ω_c, thus permitting us to predict stochastic coherence both qualitatively and quantitatively from a purely deterministic analysis. Finally, we trace the violation of the detailed balance to the non-normal nature of the system dynamics, which results in an enhancement of fluctuation amplitudes of the population. The twin phenomena of noise-induced oscillations and stochastic coherence can generally be expected in nonequilibrium stochastic birth-death systems that can be subjected to a similar analysis.

Nonrenewality and molecular memory of enzyme kinetics due to intrinsic noise

Biological processes critical to life rely crucially on the catalytic activity of enzymes. Thus the mathematical study of the spatiotemporal kinetics of intracellular enzymatic reactions is, like the study of epidemics, one of great relevance and importance. Wurtz, O'Sullivan and Thomson, Brown, Henri, the pioneers in this field, studied this problem near the end of the nineteenth century and the beginning of the twentieth . Building on their work , Michaelis and Menten proposed, exactly a hundred years ago, a reaction mechanism for enzyme catalysis , whereby enzymes bind reversibly with substrates to form intermediates which then dissociate reversibly to form the desired product. At very large concentrations of reactants, the rate of formation of products is given by the classic Michaelis-Menten (MM) equation. The actual intracellular concentrations of such reacting molecules are, however, quite small. The inherent stochasticity of a single chemical reaction and the discrete change in the number of reactant molecules combine to generate spontaneous, intrinsic fluctuations known as molecular noise. This necessitates a stochastic approach to the problem. Over the past decade, Xie and coworkers have analytically, numerically and experimentally studied the kinetics of the stochastic problem involving a single enzyme molecule and numerous substrates . They have found that enzymatic turnovers generate a renewal point process where the waiting time τ between product formation events is independently and identically distributed, and that the inverse mean time to the first turnover, $\langle T_1 \rangle^{-1}$, obeys the MM equation.

Here we study the stochastic enzyme kinetics problem for mesoscopic concentrations of reacting molecules. We formulate a birth-death master equation for the homogeneously mixed system and solve it using exact numerics. We measure the turnover time T_p to the formation of the pth product, and thus obtain the waiting time $\tau_p = T_p - T_{p-1}$ as the time between successive reaction events. The first-order distributions of waiting times, $w(\tau_p)$, though identical for all p when the number of enzyme molecules $N = 1$, vary

for different p when $N > 1$. The second-order joint distributions, $w(\tau_p, \tau_{p+q})$ show that successive distributions are not independent. Taken together, these results mean that enzymatic turnovers form a nonrenewal process for multiple enzymes. We also find that the mean of the turnover time for N enzymes, $\langle T_{p,N} \rangle$, no longer obeys the MM equation, and is also higher than the expected time to the first reaction for N pooled renewal processes, $T_{p,N} > (1/N)T_{p,1}$. The latter indicates a slowing down of multienzyme kinetics, a possible effect of the cooperativity between the various reactants.

In addition, we find that waiting times for multiple enzyme molecules are anticorrelated, where a short first interval is more likely to be followed by a long second interval and vice versa. This memory effect shows a systematic variation with enzyme number, being strong and short-lived for fewer enzymes but weak and long-lived for more enzymes. It is absent for single enzymes, and is negligible for a very large number of enzymes. The overall effect of the anticorrelations is to reduce the variance in the product turnovers when compared with a Poisson process. This may be biologically relevant to ensure a uniform rate of turnover in the steady state. Remarkably, therefore, this molecular memory of multiple enzymes acts as a regulatory mechanism for the intrinsic noise.

Hydrodynamics

Irreducible representations of active matter flows

The collective dynamics of microscopic particles that swim in viscous fluids by converting chemical energy to mechanical work is a topic of current interest in non-equilibrium statistical mechanics. Biological and biomimetic examples of such "active" particles include molecular motors, active nanobeads and swimming microorganisms such as bacteria and algae. The force-free and torque-free Stokes flows around such particles decay as r^{-2} in the far-field, the dominant contribution coming from the symmetric stress dipole,

the stresslet. Recent experiments using particle image velocimetry, that resolve the flow around swimming microorganisms in unprecedented spatial and temporal detail, reveal near-field features that cannot be captured by a purely stresslet description. For example, the microscopic alga *Chlamydomonas reinhardtii* exhibits complex flows that has easily identifiable qualitative features like stagnation points and strong lateral circulations that vary periodically with time. Both Chlamydomonas and *Volvox carteri* rotate about their axis and thus must generate swirling flows while swimming. The flow around a generic translating and rotating microswimmer is then time-dependent with both axisymmetric and swirling components. Existing theories either fail to capture swirling components, or represent the flow as an expansion in velocity point multipoles that does not account for the finite size of the particles in a simple fashion.

Here we represent Stokes flow in the bulk as an integral over the boundary S of the finite-sized active particle, where a single layer density $\mathbf{q}(\mathbf{r})$ is convolved with the dyadic Green's function $\mathbf{G}(\mathbf{r})$. Chemomechanical activity can regulate either the velocity $\mathbf{u}^S$ or the stress $\boldsymbol{\sigma}^S$ on S, and thus requires Dirichlet or Neumann boundary conditions, respectively. For a spherical particle of radius a, we expand the single layer surface density in terms of irreducible Cartesian tensors, obtaining a succinct and manifestly rotation invariant expression for the flow. Resolving the tensorial stress multipoles into their irreducible forms, we decompose active flow into its fundamental, mutually independent components, which include the familiar stresslet $\mathbf{S}$ and the potential dipole $\mathbf{d}$. The new irreducible multipoles introduced here are the second rank pseudodeviatoric torque dipole $\boldsymbol{\Psi}$ or the "vortlet", the third rank septorial stresslet dipole $\boldsymbol{\Gamma}$ or the "septlet", and the third rank pseudoseptorial multipole $\boldsymbol{\Lambda}$ or the "spinlet". The flows due to $\mathbf{d}$ and $\boldsymbol{\Psi}$ decay as r^{-3}, that due to $\boldsymbol{\Lambda}$ decays as r^{-4} and that due to $\boldsymbol{\Gamma}$ decay as r^{-5}. The vortlet and the spinlet produce swirling flows which have not been considered before. This expansion in irreducible Cartesian multipoles of the surface stress provides the most general representation of Stokes flow around a finite-sized spherical microswimmer.

Using the orthogonality of the irreducible Cartesian tensors, we obtain simple linear relationships between the velocity and stress multipoles and thus identify the multipoles necessary and sufficient and for translation and rotation. Knowing the rigid body motion we are thus able to reconstruct, using a minimal set of irreducible multipoles, the complex time-dependent flows observed in experiment. The irreducible representation further allows us to write down simple expressions for the active power dissipated and swimming efficiencies in terms of these fundamental multipoles.

We capture the essential features of the flow around a Chlamydomonas using a combination of a stresslet, a potential dipole and a septlet, parametrized uniaxially with time-varying strengths. Using a uniaxially parametrized septlet, we are able to capture the the short-ranged swirling flow field responsible for the self-rotation of microswimmers such as Chlamydomonas and Volvox. In both the translational and rotational cases, we compute the power dissipated and the appropriate swimming efficiencies and find good agreement with experiment.

Furthermore, we exploit the rotational invariance manifest in the Cartesian tensor expansion to derive a general constitutive equation for the stress tensor of an active micropolar continuum. In particular, our constitutive equation contains antisymmetric states of active stresses which, to the best of our knowledge, have not been considered previously. Since angular momentum conservation dictates that such states of stress can exist only when the medium has an internal "spin" angular momentum over and above the orbital angular momentum, we use conservation equations to couple linear and spin angular momentum. This implies that self-rotating particles, through their hydrodynamic interaction, can set up spontaneous macroscopic flows in suspension.

The simplicity of the various expressions presented here for a single active particle allows this method to be extended, in a straightforward manner, to the many-body case, where the hydrodynamic interactions among a collection of N active particles can be easily computed. This provides an exact many-body solution for the collective problem

which is computationally tractable.

Instabilities in Stokes flow due to hydrodynamic interactions of an active filament

The active single-particle analysis has been extended (Jayaraman et al., PhysRevLett, 2012; Laskar et al., SciRep, 2013) to the study of the dynamical behaviour of a semiflexible filament, composed of active point beads coupled by local elastic and self-avoiding potentials, the activity here restricted to the stresslet. Such active filaments are unstable to transverse perturbations in the presence of hydrodynamic interactions. These give rise to complex flows that, depending on whether the filament is free at both ends or clamped at one, produce either a combination of translational and rotational motion or purely rotational motion, respectively (Jayaraman et al., PhysRevLett, 2012; Laskar et al., SciRep, 2013). Motivated by these results, here we have carried out a continuum spectral analysis of the active filament under the free-draining approximation for various boundary conditions. Expressing the equation of motion as a fourth-order partial differential equation, separating variables and taking Fourier transforms, we obtain a dispersion relation and thus an expression for the wavefunction for the spatial part. This yields, for various combinations of boundary conditions, a characteristic equations and thus instability conditions in terms of a parameter α representing the relative activity. We find, however, that the fourth-order differential operator we consider is self-adjoint for any combination of boundary conditions, whether free, hinged, clamped or sliding, implying that the spectrum cannot be complex. Thus we conclude that though active filaments can become unstable in the absence of hydrodynamic interactions, oscillatory modes will not be exhibited. The above result suggests that the stability analysis of an active filament involving hydrodynamic interactions requires a spectral decomposition of the discrete equation of motion, which is expected to yield a complex spectrum indicating the presence of oscillatory modes.

We have calculated the linearized Jacobian of an active filament containing stokeslets and stresslets, and have used it to carry out a stability analysis of a *sedimenting passive* filament. We find that such a filament becomes unstable beyond a critical value of the "sedimentation number", defined as $\mathcal{S} = L^2 f_{ext}/\kappa$, where L is the length of the filament, f_{ext} is the external force and κ is the bending constant. Crucially, such instabilities are not seen in the absence of hydrodynamic interactions, highlighting their importance for active as well as passive flows.

Chapter 1

Introduction

What is Life? This is one of the oldest questions in the universe, or at least as long as sentient beings like us human beings have been around to marvel at life, the universe, and everything else that comes along with it. If Douglas Adams were to be believed, a simple, but at the same time enormously complicated, answer to this question would be "42" [1]. He explains further, in one of his rare philosophical moments, uttering, "*Life . . . is like a grapefruit. It's orange and squishy, and has a few pips in it, and some folks have half a one for breakfast.*"

It is thus quite plain that this is a question best left to philosophers and poets, people who are best equipped to extract the meaning of life out of five orange pips. This question can, however, also be asked in a very different context, resulting in a very different set of people trying to provide a very different answer. Erwin Schrödinger, otherwise known for quantum mechanics and confused cats, put forth an excellent series of arguments about what this strange phenomenon could be. The result was a seminal book, first published in 1943, aptly titled *What is Life?* [2].

In this book, Schrödinger attempts to answer the question using physics. He characterizes "living matter" as something that "evades the decay to equilibrium". Clearly, isolated physical systems, left to its own devices, will gain entropy and reach equilibrium when

they have reached their maximum entropy states. Living systems, on the other hand, actively try to stay away from equilibrium or "death" through constant exchanges with its environment. Schrödinger introduced the concept of "negative entropy" which living systems continually gather from their surroundings to counteract the debilitating effects of positive entropy. As he puts it, "*... the device by which an organism maintains itself stationary at a fairly high level of orderliness (= fairly low level of entropy) really consists in continually sucking orderliness from its environment.*"

Clearly, then, one must look at nonequilibrium physics to provide answers to the questions of life. The physics of systems in equilibrium has been comprehensively studied, is very well understood and is a staple in graduate courses (for example, [3]). This is also true for systems that are only slightly out of equilibrium, where the fluctuation-dissipation theorem holds sway, connecting the response of system near equilibrium to the equilibrium fluctuations of the relevant dynamic variables. Systems that are quite far from equilibrium are, however, much less understood, and the basic principles that govern such systems are beginning to be uncovered. Nonequilibrium phenomena are quite ubiquitous, and can be observed in systems that span an immense range of spatial and temporal scales. Decoherence in open quantum systems, photosynthesis in plants, the movement of swarms of birds or fish, the formation and evolution of swirling storm systems, the clustering of matter in the universe resulting in various galactic shapes are examples of nonequilibrium phenomena that span timescales from the nanosecond to billions of years.

In spite of this diversity, there is little doubt that the most fascinating nonequilibrium systems that the universe has to offer involve life and living organisms. The fundamental units of all known forms of life are cells. These highly active systems stay far from equilibrium through the exchange of energy due to metabolic processes as well as due to molecular motors that transduce chemical energy from ATP molecules into mechanical motion and are responsible for cell locomotion and intracellular transport of nutrients. Molecular motors are part of a large class of biomolecules called enzymes, highly selec-

tive protein catalysts that make metabolism viable by speeding it up greatly and ensuring specificity of reactions. Enzymes are also involved in the synthesis of DNA as well as in gene expression within a cell, processes whose nearly faultless execution is fundamentally critical to life. However, the internal environment of the cell is extremely noisy and is thus not a conducive environment for delicate processes. Apart from extrinsic sources of noise such as random fluctuations in temperature and pH, intrinsic noise arising out of the inherent stochasticity and discreteness of chemical reactions among finite number of molecules also contribute to the hostile intracellular environment. Since the number of intracellular reacting molecules is finite and often quite small, the level of noise is also quite high. This is because the central limit theorem states that a system of N elements exhibit statistical fluctuations of the order of $\sqrt{N}$, and thus relative fluctuations $1/\sqrt{N}$ must increase with decreasing N. Noise introduces stochasticity in gene expression, leading to mutations that can prevent normal functioning of the living organisms. To counteract this, several regulatory processes have evolved, including transcription factors that activate or repress gene expression, or negative feedback loops that function as low-pass filters that attenuate high-frequency noise and increase stability [4]. We shall encounter an example of such noise-regulation in a stochastic model of enzyme kinetics in Chapter (3) of this thesis, where intervals between successive enzyme catalyzed events will be seen to be anticorrelated, resulting in a possible stabilization of noise-induced variance.

However, the effects of noise on life are not always adverse. It provides a source of variability that can be exploited for survival needs. Phenomena such as the escape from metastable states, commonly encountered in enzyme kinetics, would not be possible without noise. Noise also gives rise to phenotypic heterogeneity, a phenomenon where individuals with identical genetic makeup exhibit varied physiological, biophysical, morphological and behavioural traits [5]. Phenotypic heterogeneity is responsible for identical twins having different fingerprints, or for cloned cats to look entirely different from each other [6]. Scattered pattern of photoreceptors in the developing retina of the fruitfly Drosophila arise because of the random switching on and off of a certain gene, allowing the fruitfly

to detect both blue and green light [7]. Bacteria such a E. coli exploit phenotypic heterogeneity to survive; if even a small percentage of a population of E. coli is resistant to a certain antibiotic, then the survivors are free to persist and create a new population immune to that antibiotic [8]. The bacterium B. subtilis utilizes the activation due to noise of a positive feedback that increases its survival probability, which drops with decreasing noise level [9, 10, 11].

Noise can have surprising counterintuitive effects as well. It can induce phenomena that are qualitatively different from that exhibited by a corresponding deterministic system by affecting the latter in nontrivial ways. For example, noise is sometimes seen to have constructive rather than destructive effects. The phenomena of stochastic resonance [12, 13], noise-induced spatial pattern formation [14] and noise-induced oscillations [15] are some examples of this behaviour. In Chapter (4) of this thesis we shall come across a model of epidemic spreading that, though deterministically stable, exhibits noise-induced oscillations. Even more surprisingly, we see that the regularity of such oscillations reach a maximum at an intermediate value of the strength of the intrinsic noise, indicating that order is actually enhanced by noise. Such phenomena are, unsurprisingly, observed only when the system is far from equilibrium, thus strongly suggesting that noise, and especially of the intrinsic variety, might be indispensable for the proper functioning of biological processes such as cellular clocks. As Schrödinger puts it, "*For it is simply a fact of observation that the guiding principle in each cell is embodied in a single atomic association existing only in one copy (sometimes two) and a fact of observation that it results in producing events which are paragons or orderliness [. . .] the situation is unprecedented, it is unknown anywhere else except in living matter.*"

The continuous conversion of energy through metabolism that keeps the interior of cells far from equilibrium, and thus alive, also helps them move. Examples of such autonomous propulsion are molecular motors (at the subcellular level) and bacteria (at the cellular level) [16, 17]. Recently, biomimetic elements which convert chemical energy into trans-

lational [18, 19] or rotational [20, 21] motion have been realized in the laboratory. While the detailed mechanisms leading to autonomous propulsion in these biological and soft matter systems show a wonderful variety [22], their collective behaviour tends to be universal and can be understood by appealing to symmetries and conservation laws [23]. This realization has led to many studies of the collective properties of suspensions of hydrodynamically interacting autonomously motile particles [24, 25].

There are ample instances in biology, however, where the conversion of chemical to mechanical energy is not confined to a particle-like element but is, instead, distributed over a line-like element. Such a situation arises, for example, in a microtubule with a row of molecular motors converting energy while walking on it. The mechanical energy thus obtained not only produces motion of the motors but also generates reaction forces on the microtubule, which can deform elastically in response. Hydrodynamic interactions between the motors and between segments of the microtubule must be taken into account since both are surrounded by a fluid. This combination of elasticity, autonomous motility through energy conversion and hydrodynamics is found in biomimetic contexts as well. A recent example is provided by mixtures of motors which crosslink and walk on polymer bundles. A remarkable cilia-like beating phenomenon is observed in these systems [26, 27]. A polymer in which the monomeric units are autocatalytic nanorods provides a nonbiological example of energy conversion on linear elastic elements. Though such elements are yet to be realized in the laboratory, active elements coupled to passive components through covalent bonds have been synthesized [19] and may lead to new kinds of nanomachines [20].

In the continuum, complex active fluids composed of dilute suspensions of motile bacteria behave very differently from their passive counterparts. While a passive colloidal suspension will always have higher viscosity than the pure solvents, adding active bacteria can actually reduce the viscosity [28]. At higher densities, the fluid can become almost non-viscous [29]. High density bacterial suspensions can exhibit large-scale oriental co-

herence as well as high degrees of correlations in velocity and vorticity [24]. Spontaneous chaotic flow, or bacterial turbulence, is another aspect of such active fluids [24]. Active filaments exhibit dynamic nonequilibrium patterns such as asters or vortices [16] in the cell cytoskeleton.

We undertake to begin to understand such complex behaviour in living matter that are far from minimal by first reducing it into minimal but fundamental components. Thus we begin by studying flows generated due to a single active particle such as unicellular swimming microorganisms. At this low Reynolds number regime, the Stokes equation governs the flow. Such flows could be generated in the bulk either by the swimming motion of flagella or the squirming motion of a ciliary envelope, both of which create effective surface stresses and velocities. This suggests, naturally, the use of the boundary integral representation of Stokes flow. The goal of the second "hydrodynamic" part of the thesis is to solve this boundary integral and obtain the desired flow.

The thesis is organized as follows. In Part [I] of the thesis, we focus on counterintuitive effects of intrinsic noise as a result of fluctuations in finite-sized populations. In Chapter (3), we find that, at the microscale, intracellular biochemical reactions catalyzed by mesoscopic concentrations of enzymes exhibit phenomena that qualitatively differ from those due to a single enzyme or a deterministically large concentration of the same. We find that intervals between successive enzyme-catalyzed reaction events are anticorrelated, and the degree of anticorrelation shows a maximum at some intermediate noise strength. In Chapter (4) we find that, at the macroscale, intrinsic noise can generate and sustain oscillations in a model of epidemic spreading. The regularity of such quasicyclic oscillations shows a maximum at some intermediate strength of the noise amplitude, a phenomenon known as stochastic coherence.

In Part [II] of the thesis, we study the dynamics of microscopic particles in a viscous fluid that are autonomously motile due to the conversion of chemical energy to mechanical motion. Momentum conservation and the lack of inertia at the microscale ensure that the

flows around such chemomechanically active particles are force-free and torque-free. In Chapter (5), we present an intuitive analytical method to study such active flows in terms of its fundamental irreducible components and to reconstruct essential features of flows around various swimming microorganisms using these "atomic" flows. In Chapter (6) we set up the equations of motion of a filament constructed out of a collection of such active particles and interacting through local elastic potentials and nonlocal hydrodynamics. Such filaments show instabilities that develop into complex flow patterns and result in complicated translational and rotational motions. Stability analysis reveals that hydrodynamic interactions are crucial for the development of oscillatory modes in the autonomous motion of active filaments, and lead to instabilities in sedimenting passive filaments.

Chapter 2

Mathematical preliminaries

In this chapter we present, in brief, some of the mathematical tools and techniques used in this thesis.

2.1 Stochastic preliminaries

Here we present a few mathematical preliminaries that will be useful for the first part of the thesis which deals with stochastic phenomena.

2.1.1 Counting and point processes

Discrete stochastic processes in continuous time can be analyzed either in the counting process description or in the point process description. In the former, the number of events n_t that have occurred in a certain time interval t is specified. In the latter, the times T_p of the occurrence of the events are specified, where T_p is the time taken for the p-th event to occur starting from the origin. Often the inter-event times or the holding times $\tau_p = T_p - T_{p-1}$ are specified instead of the event times T_p themselves. This implies, of course, that $T_p = \sum_{k=1}^{p} \tau_k$, where $T_0 = 0$ by convention. The point process is completely defined by the

joint probability density $w(\mathbf{T}) = w(T_1, T_2, \ldots T_n)$, which gives the probability that there is exactly one event in each of the non-overlapping infinitesimal intervals $(T_1\ ,\ T_1 + dT_1\ )$, $\ldots$, $(T_n\ ,\ T_n + dT_n)$. This is similar to the Stratonovich distribution functions [30, 31], and is related to the product densities due to Ramakrishnan and those due to Janossy [32, 33, 34, 31].

Formally, the p-th event time can be defined as $T_p = \inf\{t > 0 : n_t \geq p\}$ for $p = 1, 2, \ldots$, where 'inf' stands for infimum [35]. Thus we find that $n_t = 0$ iff $T_1 > t$, and that, more importantly, $n_t < p$ iff $T_p > t$. The converse of the latter relation holds true as well; $T_p \leq t$ iff $n_t \geq p$. As a result, the cumulative distribution of T_p bears the following relation to that of n_t [35]

$$P(T_p \leq t) = P(n_t \geq p, t) = 1 - P(n_t < p, t) \tag{2.1}$$

Since $n_t \in \mathbb{Z}^+$, and the states $\{n_t = 1\}$, $\{n_t = 2\}$, $\ldots$, $\{n_t = p\}$ are mutually exclusive, we have $P(n_t < p, t) = P(n_t = 0, t) + P(n_t = 1, t) + \ldots + P(n_t = p-1, t)$. Using this we rewrite Eq. (2.1) as

$$P(T_p \leq t) = 1 - \sum_{n_t=0}^{p-1} P(n_t, t) \tag{2.2}$$

Differentiating both sides with respect to time, we have the relation

$$w(T_p) = -\sum_{n_t=0}^{p-1} \frac{\partial P(n_t, t)}{\partial t}\bigg|_{t=T_p} \tag{2.3}$$

This relation can in principle be extended to multivariate distributions. If the evolution of a stochastic system in counting description is known, then the point process description can be obtained using Eq. (2.3).

2.1.2 Markov processes

Let us change notation slightly and define n_i to be the number of events that have occurred in time t_i, and let the set $\{t_i\}$ be an ordered set of successive times, that is, $t_1 < t_2 < \ldots < t_N$. The counting process is completely described by the N-variate joint distribution $P_N(n_1, t_1; \ldots; n_N, t_N)$. The stochastic process is Markovian if the following relation is true [31],

$$P_{1|N-1}(n_N, t_N \,|\, n_1, t_1; \ldots; n_{N-1}, t_{N-1}) = P_{1|1}(n_N, t_N \,|\, n_{N-1}, t_{N-1}), \tag{2.4}$$

where $P_{1|N-1}$ is the probability of the N-th event conditioned on the previous $N-1$ events, that is, on the entire stochastic path that the system has followed. In a Markov process, the entire history of the process does not matter, and a stochastic event depends only on the previous event. For a Markov process with three events occurring at $t_1 < t_2 < t_3$ and completely described by the joint distribution $P_3(n_1, t_1; n_2, t_2; n_3, t_3)$, one can write using Eq. (2.4) [31]

$$\begin{aligned} P_3(n_1, t_1; n_2, t_2; n_3, t_3) &= P_2(n_1, t_1; n_2, t_2)\, P_{1|2}(n_3, t_3 \,|\, n_1, t_1; n_2, t_2) \\ &= P_1(n_1, t_1)\, P_{1|1}(n_2, t_2 \,|\, n_1, t_1)\, P_{1|1}(n_3, t_3 \,|\, n_2, t_2) \end{aligned} \tag{2.5}$$

where we have used Bayes theorem, $P_2(A, B) = P_1(A)P_{1|1}(B\,|\,A) = P_1(B)P_{1|1}(A\,|\,B)$. Marginalizing over n_2 and using Bayes theorem once again we obtain the Chapman-Kolmogorov equation,

$$P_{1|1}(n_3, t_3 \,|\, n_1, t_1) = \sum_{n_2} P_{1|1}(n_3, t_3 \,|\, n_2, t_2)\, P_{1|1}(n_2, t_2 \,|\, n_1, t_1) \tag{2.6}$$

If the initial condition $P_1(n_1, t_1)$ and the transition probability $P_{1|1}(n_2, t_2 \,|\, n_1, t_1)$ obey the Chapman-Kolmogorov equation as well as the marginalization

$$P_1(n_2, t_2) = \sum_{n_1} P_{1|1}(n_2, t_2 \,|\, n_1, t_1) P_1(n_1, t_1), \tag{2.7}$$

then by repeated application of Eq. (2.5) they uniquely define a Markov process.

2.1.3 The master equation

A stationary Markov process is homogeneous in time where the conditional probability depends only on the time interval, $P_{1|1}(n_2, t_2 \,|\, n_1, t_1) = P_{1|1}(n_2 \,|\, n_1, \tau)$ where $\tau = t_2 - t_1$. The differential form of the Chapman-Kolmogorov equation for a stationary Markov process is called the master equation [31],

$$\frac{\partial P_{1|1}(n \,|\, n_0, t)}{\partial t} = \sum_{n'} \Big\{ W(n \,|\, n') P_{1|1}(n' \,|\, n_0, t) - W(n' \,|\, n) P_{1|1}(n \,|\, n_0, t) \Big\} \tag{2.8}$$

where the W are the transition probability rates, and n_0 is the state of the system at initial time. The master equation is thus a probability balance equation, and can be thought of as a discrete version of a continuity equation in configuration space, where the rate of change in probability of a particular state is equal to the net efflux of probability from that state. Although the master equation describes the time evolution of a stochastic process, it itself is a deterministic equation in the probabilities. It is a satisfactory description of fluctuations and corresponding jump transitions brought about by intrinsic noise.

If the stationary Markov process is defined by continuous variables $x(t)$, then the entire formalism given here will still hold given that summations are replaced by integrals. For example, the master equation will be

$$\frac{\partial P_{1|1}(x \,|\, x_0, t)}{\partial t} = \int \Big\{ W(x \,|\, x') P_{1|1}(x' \,|\, x_0, t) - W(x' \,|\, x) P_{1|1}(x \,|\, x_0, t) \Big\} \, dx'. \tag{2.9}$$

An example of such a process is the Ornstein-Uhlenbeck process [36, 31] defined by

$$P_1(x_1) = \frac{1}{\sqrt{2\pi}} \exp\left(-\frac{x_1^2}{2}\right) \tag{2.10a}$$

$$P_{1|1}(x_2 \,|\, x_1, \tau) = \frac{1}{\sqrt{2\pi\,(1 - e^{-2\tau})}} \exp\left[-\frac{(x_2 - x_1 e^{-\tau})^2}{2\,(1 - e^{-2\tau})}\right] \tag{2.10b}$$

2.1.4 Steady state, detailed balance and cyclic balance

If the net inflow of probability into a state in configuration space equals the net outflow, that is, if

$$\sum_{n'} W(n \,|\, n') P_{1|1}(n' \,|\, n_0, t) = \left(\sum_{n'} W(n' \,|\, n)\right) P_{1|1}(n \,|\, n_0, t) \tag{2.11}$$

then we have a steady state with $\partial_t P_{1|1}(n \,|\, n_0, t) = 0$. A steady state is said to be in equilibrium if the transitions between each pair of states n and n' balance individually, that is, if

$$W(n \,|\, n') P_{eq}(n') = W(n' \,|\, n) P_{eq}(n) \tag{2.12}$$

where $P_{eq}(n)$ is the equilibrium probability and can be determined from equilibrium statistical mechanics. This is the detailed balance condition, and it follows from microscopic reversibility. Conversely, a steady state can also be out of equilibrium, where detailed balance does not hold, and probability currents spanning the entire state space can occur. In Ch. (4) we shall encounter such a condition of *cyclic balance* which will make noise-induced oscillations possible out of equilibrium.

2.1.5 Solutions of birth-death master equation

The systems we shall study in this thesis have discrete random variables whose values change by unity for every stochastic event. The master equation for such "birth-death" or "one-step" processes takes the relatively simpler form

$$\begin{aligned}\frac{\partial P_{1|1}(n\,|\,n_0,t)}{\partial t} &= \sum_{n'}\Big\{W(n\,|\,n')P_{1|1}(n'\,|\,n_0,t) - W(n'\,|\,n)P_{1|1}(n\,|\,n_0,t)\Big\}\left(\delta_{n',n+1}+\delta_{n',n-1}\right)\\ &= W(n\,|\,n+1)P_{1|1}(n+1\,|\,n_0,t) + W(n\,|\,n-1)P_{1|1}(n-1\,|\,n_0,t)\\ &\quad - \Big\{W(n+1\,|\,n) + W(n-1\,|\,n)\Big\}P_{1|1}(n\,|\,n_0,t)\\ &= t^-(n+1)P_{1|1}(n+1\,|\,n_0,t) + t^+(n-1)P_{1|1}(n-1\,|\,n_0,t)\\ &\quad - \Big\{t^+(n)+t^-(n)\Big\}P_{1|1}(n\,|\,n_0,t) \qquad (2.13)\end{aligned}$$

where $t^+(n)$ is the birth rate and $t^-(n)$ is the death rate. The Poisson process is an example of a pure birth process with constant rate, $t^-(n) = 0$ and $t^+(n) = \lambda$ with λ constant. Such a birth-death master equation is often called a chemical master equation, indicating its usefulness in systems where the interactions are either chemical reactions or can be written as such.

A master equation is called linear if the associated transition probabilities $W(n\,|\,n')$ are linear. Such a master equation can, in principle, be solved exactly, perhaps by the use of generating functions. Nonlinear master equations, on the other hand, resist analytical solutions. Such equations must either be approximated to a Fokker-Planck equation (FPE) or dealt with numerically. The FPE is a continuous version of the jump process master equation, describing the evolution of the probability density of the corresponding diffusion process, and is equivalent to the corresponding Langevin or stochastic differential equation [31, 37, 38]. The first-order approximate FPE corresponding to the master equation can be written down by systematically expanding in inverse powers of a large parameter Ω such as the system size [31], the Ω chosen so that the sizes of individual jumps are relatively small.

Exact solutions of the master equation are also possible using numerical means, of which the Doob-Gillespie algorithm is the most popular. Joseph Doob [39], building on earlier work by Kolmogorov [40] and Feller [41], proposed a method of obtaining stochastic trajectories from the corresponding master equation. It was implemented by Kendall [42] and Bartlett [43, 44] on the Manchester Mark I computer, and popularized by Gillespie [45, 46]. The algorithm assumes that collisions between reacting molecules are frequent, but not all collisions lead to reaction events, and those that do are mostly binary reactions. The reactants are also assumed to be well-mixed. Given that there are N simultaneous ongoing reactions indexed by μ, the algorithm proceeds by determining the probability density $P(\tau, \mu)$ using a Monte Carlo method, where $P(\tau, \mu)d\tau$ is the probability that given a certain state of the system at time t, the next reaction will occur in the infinitesimal time interval $(t + \tau, t + \tau + d\tau)$ and will be of the μ-th channel. The algorithm produces a stochastic trajectory whose distribution is exactly equal to that of the master equation.

2.2 Hydrodynamic preliminaries

Here we present a few mathematical preliminaries that will be useful for the second part of the thesis which deals with hydrodynamic phenomena.

2.2.1 Equation of motion of viscous fluid

The Navier-Stokes (N-S) equation describes the motion of viscous fluids. If $\mathbf{u}(\mathbf{r})$ be the velocity of the fluid of density ρ at some point $\mathbf{r}$, then the N-S equation is given by $\rho \dfrac{D\mathbf{u}}{Dt} = \boldsymbol{\nabla} \cdot \boldsymbol{\sigma}$, where $\boldsymbol{\sigma}$ is the stress tensor and $\dfrac{D}{Dt} = \dfrac{\partial}{\partial t} + \mathbf{u} \cdot \boldsymbol{\nabla}$ is the material derivative. The constitutive equation for the stress tensor is

$$\boldsymbol{\sigma} = -p\mathbb{I} + \boldsymbol{\eta} \odot \boldsymbol{\nabla}\mathbf{u} \tag{2.14}$$

where p is the pressure, $\mathbb{I}$ is the second rank identity matrix and η is the fourth rank viscosity tensor. The symbol $\odot$ indicates complete contraction, that is, $\boldsymbol{\eta} \odot \boldsymbol{\nabla}\mathbf{u} \rightarrow \eta_{ij\alpha\beta}\nabla_\alpha u_\beta$ in index notation. Here, and in the rest of the thesis, we shall follow the Einstein summation convention whereby repeated indices will indicate summation, unless otherwise stated. Resolving the viscosity tensor into a isotropic bulk component ζ and a symmetric traceless shear component η,

$$\eta_{ij\alpha\beta} = \zeta\delta_{ij}\delta_{\alpha\beta} + \eta\left(\delta_{i\beta}\delta_{j\alpha} + \delta_{j\alpha}\delta_{i\beta} - \frac{2}{3}\delta_{ij}\delta_{\alpha\beta}\right) \tag{2.15}$$

we have

$$\boldsymbol{\eta} \odot \boldsymbol{\nabla}\mathbf{u} = \zeta\left(\boldsymbol{\nabla}\cdot\mathbf{u}\right)\mathbb{I} + \eta\,\overline{\boldsymbol{\nabla}\mathbf{u}} \tag{2.16}$$

where the stapler symbol denotes the natural form of the corresponding tensor, that is, $\overline{\boldsymbol{\nabla}\mathbf{u}} \rightarrow \nabla_i u_j + \nabla_j u_i - \frac{2}{3}\delta_{ij}\nabla_\mu u_\mu$. Thus the Navier-Stokes equation can be written in the familiar form [47],

$$\rho\left\{\frac{\partial\mathbf{u}}{\partial t} + \left(\mathbf{u}\cdot\boldsymbol{\nabla}\right)\mathbf{u}\right\} = -\boldsymbol{\nabla}p + \eta\nabla^2\mathbf{v} + \left(\zeta + \frac{1}{3}\eta\right)\boldsymbol{\nabla}\left(\boldsymbol{\nabla}\cdot\mathbf{v}\right) \tag{2.17}$$

The equation simplifies considerably for incompressible fluids where the fluid flow is divergenceless, that is $\boldsymbol{\nabla}\mathbf{u} = 0$. The N-S equation thus becomes

$$\rho\left\{\frac{\partial\mathbf{u}}{\partial t} + \left(\mathbf{u}\cdot\boldsymbol{\nabla}\right)\mathbf{u}\right\} = -\boldsymbol{\nabla}p + \eta\nabla^2\mathbf{u} \tag{2.18}$$

The Reynolds number (Re) is a dimensionless number that qualitatively captures the flow regime. It is generally defined as the ratio of inertial forces to viscous forces and consequently quantifies the relative importance of these two types of forces for given flow conditions. At low Reynolds numbers, viscous forces dominate in the fluid. In this non-

inertial regime the Navier-Stokes equation becomes the Stokes equation given by

$$0 = -\nabla p + \eta \nabla^2 \mathbf{u} \tag{2.19a}$$

$$0 = \nabla \cdot \mathbf{u} \tag{2.19b}$$

2.2.2 Boundary integral formulation of Stokes equation

The singularly forced Stokes equation is [48]

$$0 = -\nabla p + \eta \nabla^2 \mathbf{u} + \mathbf{g}\delta(\mathbf{r} - \mathbf{r}') \tag{2.20}$$

with $\nabla \cdot \mathbf{u} = 0$. Here $\mathbf{g}$ represents a point force at $\mathbf{r}'$. The flow, pressure and stress are then given by

$$\mathbf{u}(\mathbf{r}) = \frac{1}{8\pi\eta}\mathbf{G}(\mathbf{r} - \mathbf{r}') \cdot \mathbf{g} \tag{2.21a}$$

$$P(\mathbf{r}) = \frac{1}{8\pi}\mathbf{p}(\mathbf{r} - \mathbf{r}') \cdot \mathbf{g} \tag{2.21b}$$

$$\sigma(\mathbf{r}) = \frac{1}{8\pi}\mathbf{T}(\mathbf{r} - \mathbf{r}') \cdot \mathbf{g} \tag{2.21c}$$

where $\mathbf{G}$, $\mathbf{p}$ and $\mathbf{T}$ are the Green's functions associated with the fluid velocity, the pressure and the stress. These are related through the equation [48]

$$T_{ijk}(\mathbf{r} - \mathbf{r}') = -p_j(\mathbf{r} - \mathbf{r}')\delta_{ik} + \left[\frac{\partial G_{ij}}{\partial r_k}(\mathbf{r} - \mathbf{r}') + \frac{\partial G_{kj}}{\partial r_i}(\mathbf{r} - \mathbf{r}')\right]. \tag{2.22}$$

and are individually given by [48]

$$G_{ij}(\mathbf{r}) = \frac{\delta_{ij}}{r} + \frac{r_i r_j}{r^3} \tag{2.23a}$$

$$p_i(\mathbf{r}) = \frac{2r_i}{r^3} \tag{2.23b}$$

$$T_{ijk}(\mathbf{r}) = -\frac{6r_i r_j r_k}{r^5} \tag{2.23c}$$

where $r = |\mathbf{r}|$.

The reciprocal theorem states that for two flows $\mathbf{u}$ and $\mathbf{u}'$ corresponding to stresses $\boldsymbol{\sigma}$ and $\boldsymbol{\sigma}'$, we have

$$\boldsymbol{\nabla} \cdot (\mathbf{u}' \cdot \boldsymbol{\sigma} - \mathbf{u} \cdot \boldsymbol{\sigma}') = 0 \tag{2.24}$$

Using Eqs. (2.21a) and (2.21c) in Eq. (2.24) we have

$$\boldsymbol{\nabla} \cdot \left[\mathbf{G}(\mathbf{r} - \mathbf{r}') \cdot \boldsymbol{\sigma}(\mathbf{r}) - \eta\, \mathbf{T}(\mathbf{r} - \mathbf{r}') \cdot \mathbf{u}(\mathbf{r})\right] = 0 \tag{2.25}$$

Taking a control volume V with boundary S, and putting the "source point" at $\mathbf{r}'$ *outside* it, we perform the volume integral and use the divergence theorem to convert this into a surface integral with the unit vector $\hat{\mathbf{n}}$ pointing *into* the flow. We get

$$\int_S \left[\mathbf{G}(\mathbf{r} - \mathbf{r}') \cdot \boldsymbol{\sigma}(\mathbf{r}) - \eta\, \mathbf{T}(\mathbf{r} - \mathbf{r}') \cdot \mathbf{u}(\mathbf{r})\right] \cdot \hat{\mathbf{n}}\, \mathrm{d}S = 0 \tag{2.26}$$

If instead we put the point $\mathbf{r}'$ *inside* the control volume, the flow at $\mathbf{r}'$ is given by

$$\mathbf{u}(\mathbf{r}') = -\frac{1}{8\pi\eta} \int_S \mathbf{G}(\mathbf{r} - \mathbf{r}') \cdot \mathbf{f}(\mathbf{r})\, \mathrm{d}S + \frac{1}{8\pi} \int_S \mathbf{T}(\mathbf{r} - \mathbf{r}') \cdot \mathbf{u}(\mathbf{r}) \cdot \hat{\mathbf{n}}(\mathbf{r})\, \mathrm{d}S \tag{2.27}$$

where $\mathbf{f} = \boldsymbol{\sigma} \cdot \hat{\mathbf{n}}$ is the surface traction. If however the point $\mathbf{r}'$ be now placed *on* the boundary S, the flow is given by

$$\mathbf{u}(\mathbf{r}') = -\frac{1}{4\pi\eta} \int_S \mathbf{G}(\mathbf{r} - \mathbf{r}') \cdot \mathbf{f}(\mathbf{r})\, \mathrm{d}S + \frac{1}{4\pi} \int_S^{\mathcal{PV}} \mathbf{T}(\mathbf{r} - \mathbf{r}') \cdot \mathbf{u}(\mathbf{r}) \cdot \hat{\mathbf{n}}\, \mathrm{d}S \tag{2.28}$$

where $\mathcal{PV}$ denotes the principal value. The first integral is the *single layer potential*, while the second integral is the *double layer potential* [49, 48, 50]. Exchanging $\mathbf{r}$ and $\mathbf{r}'$ and using the symmetry relation for the single and double layer Green's functions [48, 50],

the boundary integral representation of Stokes flow is

$$\mathbf{u}(\mathbf{r}) = -\frac{1}{8\pi\eta}\int_S \mathbf{G}(\mathbf{r}-\mathbf{r}')\cdot\mathbf{f}(\mathbf{r}')\,\mathrm{d}S' + \frac{1}{8\pi}\int_S \mathbf{T}(\mathbf{r}-\mathbf{r}')\cdot\mathbf{u}(\mathbf{r}')\cdot\hat{\mathbf{n}}'\,\mathrm{d}S' \tag{2.29}$$

$$\mathbf{u}(\mathbf{r}) = -\frac{1}{4\pi\eta}\int_S \mathbf{G}(\mathbf{r}-\mathbf{r}')\cdot\mathbf{f}(\mathbf{r}')\,\mathrm{d}S' + \frac{1}{4\pi}\int_S^{\mathcal{PV}} \mathbf{T}(\mathbf{r}-\mathbf{r}')\cdot\mathbf{u}(\mathbf{r}')\cdot\hat{\mathbf{n}}'\,\mathrm{d}S' \tag{2.30}$$

where $\mathbf{r} \in V$ for Eq. (2.29) and $\mathbf{r} \in S$ for Eq. (2.30).

We simplify matters by eliminating the double layer potential. We introduce a flow $\mathbf{u}'$ in the interior of the boundary S that is complementary to $\mathbf{u}$ exterior to S, with the boundary condition $\mathbf{u} = \mathbf{u}'$ on S. Then we can write down [48], by combining Eqs. (2.26) and (2.27)

$$\mathbf{u}(\mathbf{r}) = -\frac{1}{8\pi\eta}\int_S \mathbf{G}(\mathbf{r}-\mathbf{r}')\cdot\mathbf{q}(\mathbf{r}')\,\mathrm{d}S' \tag{2.31}$$

where the modified single layer density $\mathbf{q}$ is simply the traction jump across S, $\mathbf{q} = \mathbf{f} - \mathbf{f}'$.

Chapter 3

Nonrenewality and molecular memory in enzyme kinetics due to intrinsic noise

In this chapter, we study the stochastic process of enzymatic turnovers at concentrations between the extremes of the thermodynamically large and single-enzyme regimes. In the thermodynamic limit the process reduces to deterministic evolution governed by mass action kinetics, while in the single-enzyme limit it reduces to a renewal process. In both these cases, the rate of reactions is governed by the Michaelis-Menten (MM) equation. Our key findings are that for mesoscopic numbers of enzymes, the turnover process is of the non-renewal type with waiting times that are neither independent, nor identically distributed. We write down a chemical master equation and solve it numerically. We obtain the waiting time distributions and show that their inverse first moments do not obey the MM equation. Consecutive waiting times are anti-correlated, with short intervals more likely to be followed by long intervals and vice-versa. The correlations persist beyond consecutive turnovers and, depending on the number of enzymes, can become substantially long-ranged. Together, these results imply that the enzymatic turnovers at the mesoscale cannot be described by mean production rates (as in the thermodynamic limit) or mean waiting times (as in the single-enzyme limit), but must be described by

statistical measures which capture fluctuations over multiple time scales.

3.1 Michaelis-Menten enzyme kinetics

Biological processes rely crucially on the catalytic activity of enzymes. In 1913, following the work of Wurtz and several others [51, 52, 53, 54], Michaelis and Menten proposed [55] a reaction mechanism for catalysis where enzyme E binds reversibly with substrate S to form an enzyme-substrate complex ES which then dissociates irreversibly to form product P, while regenerating the enzyme,

$$E + S \underset{k_{-1}}{\overset{k_1}{\rightleftharpoons}} ES \xrightarrow{k_2} E + P. \tag{3.1}$$

For thermodynamically large numbers of reactants, deterministic mass action kinetics provides the temporal variation of the concentrations of enzyme, complex and product. The rate of product formation is given by the classic Michaelis-Menten (MM) equation, provided suitable adiabaticity conditions are satisfied [56, 57].

$$V = \frac{V_{max}[S]}{K_m + [S]} \tag{3.2}$$

is the MM equation, where V is the reaction rate, V_{max} is the (constant) maximum possible rate, $[S]$ is the substrate concentration, and K_m is the Michaelis constant. Writing this in terms of reciprocals, we have

$$\frac{1}{V} = \frac{K_m}{V_{max}} \frac{1}{[S]} + \frac{1}{V_{max}} \tag{3.3}$$

Thus plot of the inverse rate of the reaction with the inverse substrate concentration, a Lineweaver-Burk plot, is expected to be linear in the deterministic case. However, enzyme and substrate concentrations in biochemical catalysis are not thermodynamically large. *In vivo* enzyme concentrations vary from nanomolar to micromolar, while the substrates are

typically between a ten and ten thousand times more numerous [58]. An important exception is in glycolysis where enzyme concentrations exceed those of substrates [58]. *In vitro* enzyme concentrations vary from picomolar to nanomolar and substrates are typically a million times more numerous [59, 60]. At these low concentrations, the inherent stochasticity of a single chemical reaction and the discrete change in the number of reactant molecules combine to generate spontaneous, intrinsic fluctuations known as molecular noise [61]. The temporal variation of catalysis, then, is also influenced by molecular noise and is a stochastic process in time. Recent advances in single molecule spectroscopy have been able to unravel some features of this stochastic process for catalysis involving a single enzyme and numerous substrates [62, 63]. A striking feature is that the enzymatic turnovers generate a renewal point process where the waiting time τ between product formation events is independently and identically distributed. Remarkably, the inverse of the mean waiting time $\langle\tau\rangle^{-1}$ obeys the MM equation which, in this interpretation, is valid not only for thermodynamically large systems, but also at the single-enzyme level. Below we show that these phenomena no longer appear when multiple enzymes are involved.

3.2 Michaelis-Menten stochastic analysis

At the mesoscopic scale, enzymatic reactions governed by Eq. (3.1) form a discrete stochastic process in continuous time. As discussed in the introduction, Ch. (1), such a process can be analyzed in either the counting process description or the point process description. Here we formulate the problem in the former description but analyze it in the latter. The configuration set $\mathbf{n} = \{n_S, n_E, n_{ES}, n_P\}$, where n_S, n_E, n_{ES} and n_P are the numbers of the various molecular species involved, describes the state of the system at any time t. The evolution of the system can be expressed as a multivariate Markov counting process governed by a chemical master equation (CME), the solution to which gives the joint probabilities $P(\mathbf{n}, t)$ with the initial condition $P(\mathbf{n}, 0) = \delta_{n_E,N}\,\delta_{n_S,S}\,\delta_{n_{ES},0}\,\delta_{n_P,0}$, where $\delta_{x,y}$ is the Kronecker delta function. In the counting description, these proba-

bilities describe the system completely. We assume that the system is reaction-limited, i.e., diffusion plays no role in the dynamics, and that the system is well-mixed. Since substrates are more numerous than enzymes, the bimolecular second-order complexation step $E + S \xrightarrow{k_1} ES$ is replaced by a pseudo-first order complexation step with an effective rate constant $k_a = k_1 S$. We justify the validity of this pseudo-first-order approximation (PFO) later in the chapter. Under the PFO approximation, our reaction system reduces to $E \underset{k_{-1}}{\overset{k_a}{\rightleftharpoons}} ES \xrightarrow{k_2} E + P$, where $k_a = k_1 S$ is a constant. Thus, denoting the PFO probability as $P(n_E, n_{ES}, n_P, t)$, the CME is

$$\begin{aligned}\frac{\partial P(n_E, n_{ES}, n_P, t)}{\partial t} &= k_a(n_E + 1)\, P(n_E + 1, n_{ES} - 1, n_P, t) \\ &\quad + k_{-1}(n_{ES} + 1)\, P(n_E - 1, n_{ES} + 1, n_P, t) \\ &\quad + k_2(n_{ES} + 1)\, P(n_E - 1, n_{ES} + 1, n_P - 1, t) \\ &\quad - \left[k_a n_E + (k_{-1} + k_2) n_{ES}\right] P(n_E, n_{ES}, n_P, t) \end{aligned} \tag{3.4}$$

This is a linear master equations, and can, in principle, be solved analytically. An exact analytical solution was obtained by Saha et al. in [64, 65] using generating functions. We generate exact numerical trajectories of Eq. (3.4) using the Doob-Gillespie algorithm [39, 45, 46]. One such trajectory is shown in Fig. (3.1). For the numerical simulations we non-dimensionalize time in units of k_2 and choose rate constants as $k_a = k_2$ and $k_{-1} = \frac{1}{2}k_2$.

We describe the trajectories in Fig. (3.1) using the point process description. We define turnover times as $T_p = \inf\{t > 0 : n_P(t) \geq p\}$ for $p = 1, 2, \ldots$, which implies that $T_p \leq t$ if and only if $n_P(t) \geq p$. This provides the connection between the counting and point processes and relates the cumulative distribution of T_p to that of n_P by $P(T_p \leq t) = P(n_p \geq p, t)$ [35]. Waiting times are defined from the turnover times by $\tau_p = T_p - T_{p-1}$ with the convention that $T_0 = 0$. The point process is fully specified by the joint probability distributions w of either the T_p or the τ_p [34, 32, 35]. Here we focus on the first-order distributions of the time to the p-th turnover $w(T_p)$ and the interval between the p-th and $(p + 1)$-th turnovers $w(\tau_p)$. We use second-order distributions $w(\tau_p, \tau_{p+q})$ to

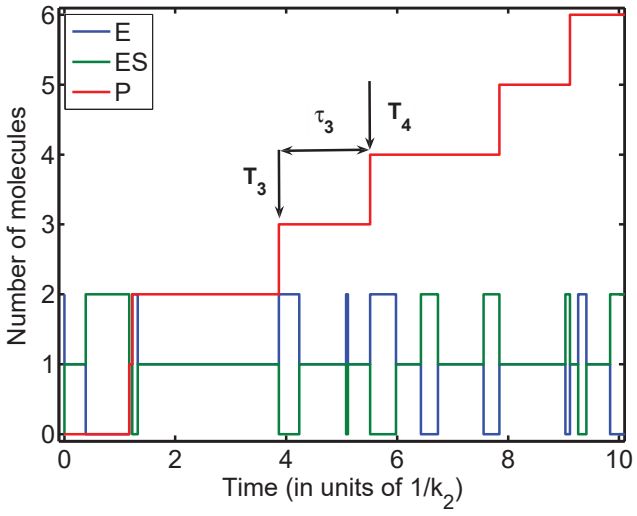

Figure 3.1: A trajectory of Eq. (3.4) for $N = 2$ enzymes. The p-th product is generated at time T_p. The waiting time between the p-th and $(p+1)$-th product is $\tau_p = T_{p+1} - T_p$.

study correlations between the p-th and $(p+q)$-th turnovers. We obtain these probability distributions by generating ensembles of typically 10^6 trajectories.

3.3 First-order distributions

We benchmark our numerics by plotting the distributions of waiting times for a single enzyme, $w(\tau_p; N = 1)$, for the first turnover event $p = 1$, the tenth $p = 10$ and the hundredth $p = 100$. As the inset of Fig. (3.2) shows, these three distributions overlap each other and with the analytical result [64, 65], implying that the waiting times are indeed identically distributed for $N = 1$. In Fig. (3.4), we compare distributions of the numerically obtained turnover times $w(T_p)$ for multiple enzymes with the corresponding analytical result [64, 65] and find very good agreement.

In the main panel of Fig. (3.2) we compare $w(\tau_p)$ for $p = 1, 10, 100$ for $N = 1000$ enzymes. We find that, unlike the single enzyme case, here the τ_p are no longer identically distributed. This clearly establishes the non-renewal nature of the turnover process when more than one enzyme participates in catalysis. We further find, from the $w(\tau_1)$ curve of

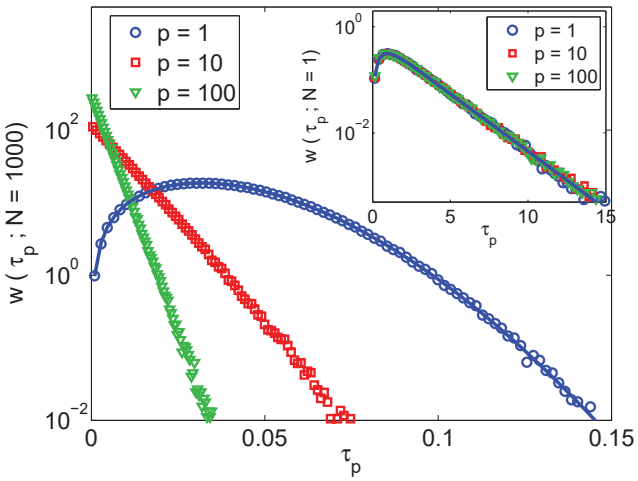

Figure 3.2: Nonrenewality of multienzyme kinetics. Waiting time distributions for $N = 1000$ and $N = 1$ enzymes. Solid lines are analytical results obtained from Eq. (3.5) while the symbols are simulation data. The waiting times are identically distributed for a single enzyme (inset), but vary with the turnover number p for multiple enzymes, implying nonrenewality.

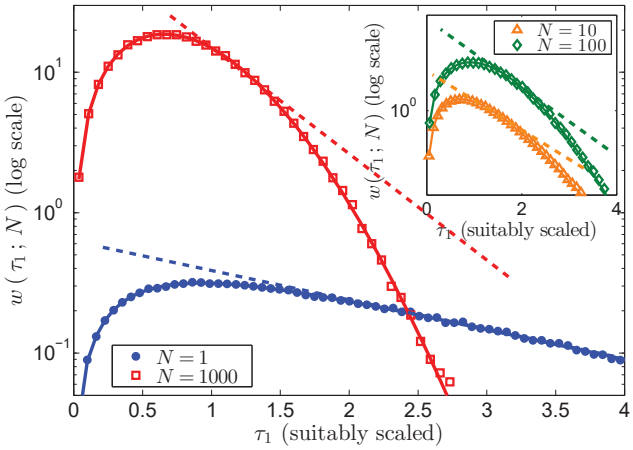

Figure 3.3: Multiexponentiality of the distribution of the first waiting times. Here we plot $w(\tau_1) = w(T_1)$ from numerics for $N = 1$ (blue filled circles), $N = 10$ (inset, orange triangles), $N = 100$ (inset, green diamonds) and $N = 1000$ (red squares). All curves for $N > 1$ have multiexponential tails, as shown by the dotted guide lines. The analytical curves (solid lines) are obtained from Eq. (3.5). Parameter values are $k_a/k_2 = 1$ and $k_{-1}/k_2 = 0.5$ and all times are in units of $1/k_2$.

Fig. (3.2) and the curves in Fig. (3.3) that these distributions have nonexponential tails. Surprisingly, starting with a Markovian master equation where waiting times between transitions are exponentially distributed, we obtain a waiting time between turnovers that

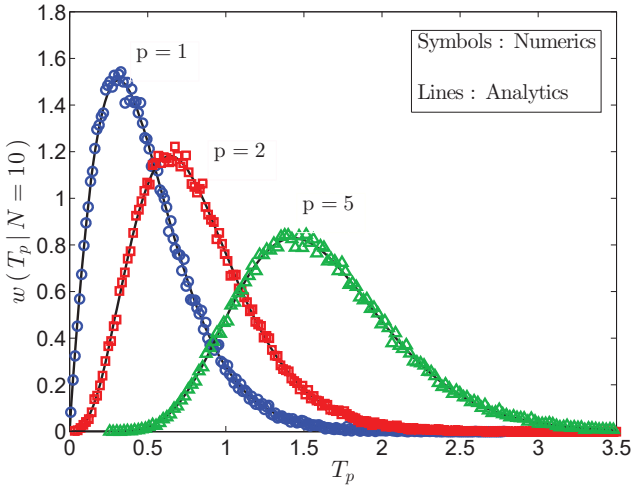

Figure 3.4: Comparison between numerics (symbols) and analytics (solid lines) for turnover times. Here the $p = 1$ analytical curve is obtained from Eq. (7) while the $p = 2$ and the $p = 5$ analytical curves are obtained from Eq. (6). Parameter values are $k_1/k_2 = 1$, $k_{-1}/k_2 = 0.5$ and all times are in units of $1/k_2$.

is multi-exponential. For this, it is crucial to have more than one enzyme in the system. The resulting point process for the products alone is then a combination of multiple internal states for the enzyme-substrate complex and is thus no longer Markovian. The multi-exponentiality of the waiting times is, therefore, consistent with the non-Markovian nature of the turnovers. For a single enzyme, though, with only one internal enzyme-substrate state, there is no multi-exponentiality, but only a mono-exponential rise and fall. This is in agreement with experimental [66, 63], numerical [62] and analytical [66, 64, 65] results.

3.4 Moments of first-order distributions

For a single enzyme, the inverse of the mean of the first waiting time follows the MM equation. For example, from the analytical expression for $w(T_1)$ [64, 65],

$$w(T_1) = \frac{k_2 k_a N}{(2A)^N}\left[e^{(A-B)T_1} - e^{-(A+B)T_1}\right]\left[(A+B)e^{(A-B)T_1} + (A-B)e^{-(B+A)T_1}\right]^{N-1} \tag{3.5}$$

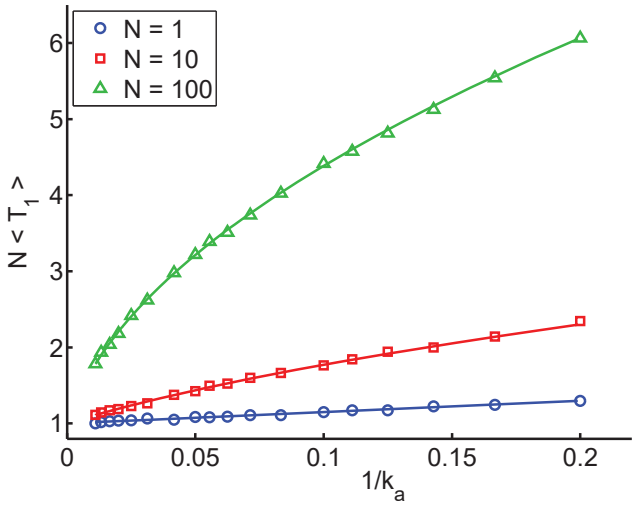

Figure 3.5: Breakdown of Michaelis-Menten kinetics for multiple enzymes. Here we plot the numerically obtained $\langle T_1 \rangle$ in Lineweaver-Burk fashion against the inverse rate constant k_a for $N = 1$ (blue circles), $N = 10$ (red squares) and $N = 100$ (green triangles). With more than one enzyme, the MM equation (circles) is obeyed only in the limit of infinite substrate concentration or equivalently for $1/k_a \to 0$ (see Fig. 3.6). The analytical curves (solid lines) are first moments of Eq. (3.5).

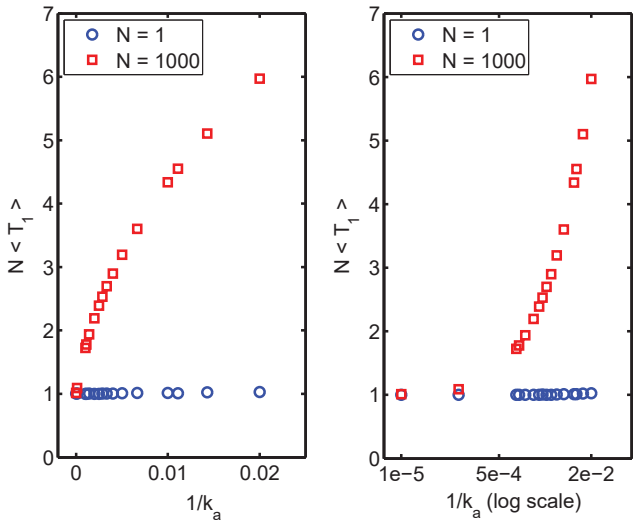

Figure 3.6: Convergence of multienzyme kinetics to single enzyme behaviour for large values of $k_a = k_1 S$. The plot on the left is $\langle T_1 \rangle$ plotted in Lineweaver-Burk fashion against $1/k_a$, as in Fig. (3.5), while the plot on the right shows the abscissa is log scale, clearly demonstrating that the plot for $N = 1000$ converges to that for $N = 1$ (the MM equation) as the effective number of substrate molecules approach deterministic limits.

it follows that $\langle T_1 \rangle = \int_0^\infty dT_1 \; T_1 w(T_1) = (S + K_M)/k_2 S$. This has lead Xie and coworkers to extend the validity of the MM equation to the single-enzyme level [66, 62, 63]. In Fig.

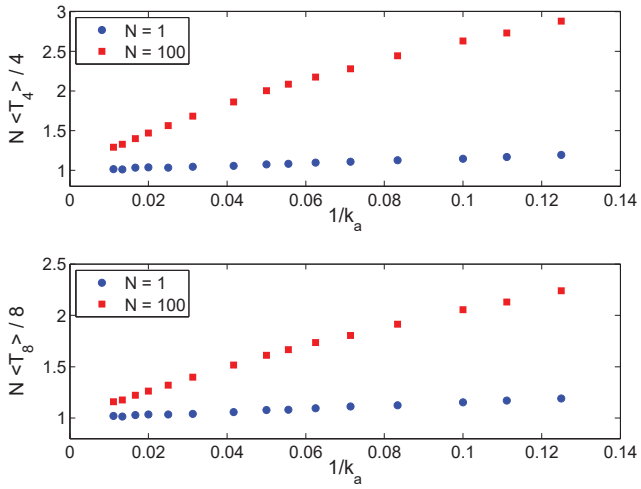

Figure 3.7: Breakdown of the MM equation for multienzyme kinetics, demonstrated by first moments of higher turnover times. Here we plot $\langle T_4 \rangle$ and $\langle T_8 \rangle$, scaled by the number of enzyme molecules as well as the turnover number p, for $N = 1$ (blue circles) and $N = 1000$ (red squares). While the MM equation holds for very large $k_a = k_1 S$, it fails to predict multienzyme kinetics at low k_a.

(3.5), we plot $\langle T_1 \rangle$ for $N = 1$ (blue circles) against $1/k_a$ in Lineweaver-Burk fashion and find the expected linear dependence.

Multiple enzyme kinetics presents a different picture, however. In Fig. (3.5), we further plot, in Lineweaver-Burk fashion, $N\langle T_1 \rangle$ for $N = 10$ (red squares) and $N = 100$ (green triangles). We find that the curves vary nonlinearly with $1/k_a$ and deviate away from the MM behaviour. This nonlinearity in $\langle T_1 \rangle$ for $N > 1$ arises from the multiexponentiality of $w(T_1)$. Thus, a turnover time interpretation of the MM equation is no longer valid for multiple enzymes. The mean turnover time converges to the MM estimate only in the limit of infinite substrate concentration or equivalently for $1/k_a \to 0$, as can be clearly seen in Fig. (3.6). Means $\langle T_p \rangle$ show similar behavior, as can be seen in Fig. (3.7).

3.5 Second-order distributions and memory

We compute the joint distributions $w(\tau_p, \tau_{p+q})$ of τ_p and τ_{p+q} and their Pearson correlation coefficient from numerical trajectories. In Fig. (3.8) we plot the correlation coefficient

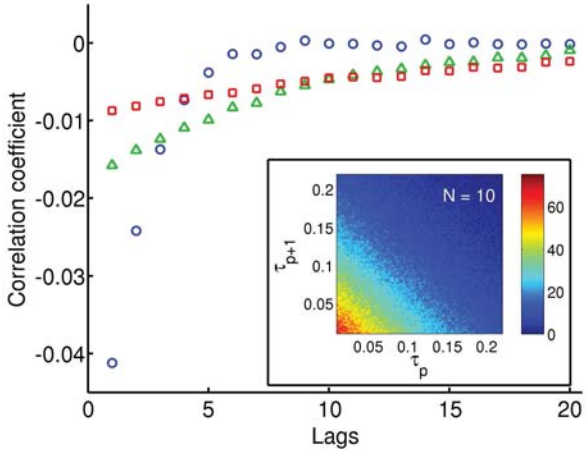

Figure 3.8: The Pearson correlation coefficient of τ_p and τ_{p+q} as a function of lag q for $N = 10$ (circles), $N = 50$ (triangles) and $N = 100$ (squares). The inset shows the joint distribution $w(\tau_p, \tau_{p+1})$ for $N = 10$.

against lag q, showing the joint distribution of consecutive intervals in the inset. The waiting times are anti-correlated, where a short first interval is more likely to be followed by a long second interval and vice-versa. This memory effect shows a systematic variation with enzyme number, being strong and short-lived for fewer enzymes but weak and long-lived for more enzymes. With long-lived memory, fluctuation statistics will vary with the size of the temporal window, and multiple measures will be required to characterize the turnover process. In future work, we plan to explore this systematically, by studying higher-order joint distributions. The overall effect of the anti-correlations is to reduce the variance in the product turnovers when compared with a Poisson process. This may be biologically relevant to ensure a uniform rate of turnover in the steady state.

3.6 Antibunching of intervals and memory indicators

We note that this anticorrelation in turnovers is similar to the phenomenon of antibunching in resonance fluorescence experiments, where the number of emitted photons obey sub-Poissonian statistics [67]. Unlike photons however, it is the *intervals* between turnovers

that are anticorrelated, indicated a possible antibunching phenomenon in the point process description.

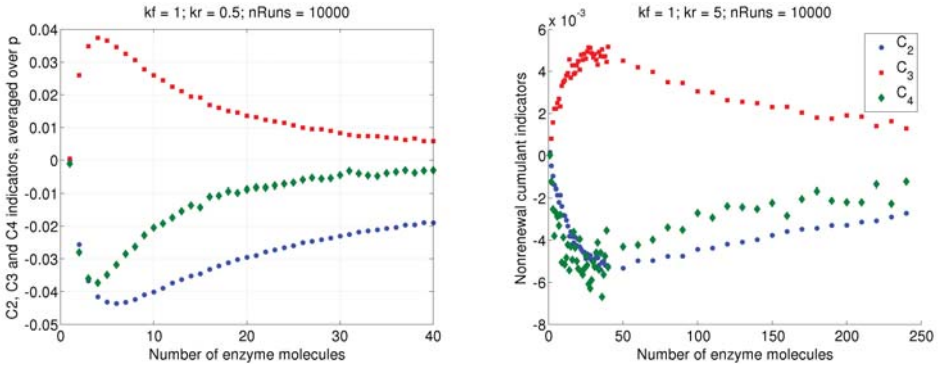

(a) $k_f = 1, k_r = 0.5$ (b) $k_f = 1, k_r = 5.0$

Figure 3.9: Scan of the memory indicators against enzyme number N. Indicators C_2 (blue circles) and C_4 (green diamonds) are negative whereas C_3 (red squares) is positive throughout, indicating that successive intervals are anticorrelated. The degree of anti-correlation is maximum for some intermediate N, and this value of N increases with the reverse parameter $k_r = k_{-1}/k_2$. There is no discernible effect on the position of the extremum of changing the value of the forward rate parameter $k_f = k_a/k_2$.

A typical problem faced in photon statistics is to quantify the bunching or antibunching of emitted or detected photons, where bunching indicates sub-Poissonian statistics and antibunching indicates super-Poissonian statistics. The Mandel Q-parameter [67] is an ideal indicator for quantifying deviations from Poissonian statistics. If there be $n(t)$ photons emitted/detected in a time interval t, then the the Q-parameter is defined by

$$Q = \frac{\langle\langle n(t)\rangle\rangle}{\langle n(t)\rangle} - 1. \tag{3.6}$$

Here $\langle n(t)\rangle$ is the mean, $\langle\langle n(t)\rangle\rangle = \langle n(t)^2\rangle - \langle n(t)\rangle^2$ is the variance, and thus $Q = F - 1$, where F is the Fano factor and is defined as the ratio of the variance to the mean. $Q = 0$ is a necessary and sufficient condition for Poissonity. Photons are bunched when $Q < 0$ and are antibunched when $Q > 0$.

The Q-parameter corresponds to a counting process and the statistics of events, rather than that of the intervals between them. The point process counterpart of the Q-parameter

is defined in the stationary regime in terms of multiple moments of successive waiting times [68],

$$\mathcal{M} = \frac{\langle \tau_p \tau_{p+1} \rangle}{\langle \tau_p \rangle^2} - 1, \tag{3.7}$$

where $\mathcal{M} > 0$ indicated correlation between intervals, whereas $\mathcal{M} < 0$ indicates anti-correlation. However, indicators based on multiple cumulants rather than multiple moments are better at quantifying correlation and thus the effect of molecular memory. We therefore propose the following three memory indicators in terms of the cumulants of $w(\tau_p, \tau_{p+1}, \ldots)$.

$$C_2 = \frac{1}{\langle \tau_p \rangle^2} \Big(\langle \tau_p \tau_{p+1} \rangle - \langle \tau_p \rangle \langle \tau_{p+1} \rangle \Big) \tag{3.8a}$$

$$C_3 = \frac{1}{\langle \tau_p \rangle^3} \Big(\langle \tau_p \tau_{p+1} \tau_{p+2} \rangle - 3 \langle \tau_p \tau_{p+1} \rangle \langle \tau_p \rangle + 2 \langle \tau_p \rangle \langle \tau_{p+1} \rangle \langle \tau_{p+2} \rangle \Big) \tag{3.8b}$$

$$\begin{aligned} C_4 = \frac{1}{\langle \tau_p \rangle^4} \Big(& \langle \tau_p \tau_{p+1} \tau_{p+2} \tau_{p+3} \rangle - 4 \langle \tau_p \tau_{p+1} \tau_{p+2} \rangle \langle \tau_p \rangle - 3 \langle \tau_{p+2} \tau_{p+3} \rangle \langle \tau_p \tau_{p+1} \rangle \\ & + 12 \langle \tau_p \tau_{p+1} \rangle \langle \tau_p \rangle \langle \tau_{p+1} \rangle - 6 \langle \tau_p \rangle \langle \tau_{p+1} \rangle \langle \tau_{p+2} \rangle \langle \tau_{p+3} \rangle \Big) \end{aligned} \tag{3.8c}$$

Here C_2 is like a multivariate version of the Fano factor. We numerically compute the values of these indicators in the stationary regime, having averaged over a large number of values of p. In Fig. (3.9), we plot these against N, and find that the two-point correlator C_2 and the four-point correlator C_4 are negative throughout, whereas the three-point correlator C_3 is positive throughout. We thus conclude that successive intervals are anti-correlated, and thus there is an *antibunching of intervals*. Curiously, the strength of the correlation reaches a maximum at an intermediate value of the enzyme number N. This is an interesting result when compared to resonance fluorescence experiments, where the strength of photon-photon correlation varied inversely as the number of photons [69]. We shall come across a similar phenomena in Chapter (4) when we study the coherence of noise-induced oscillations.

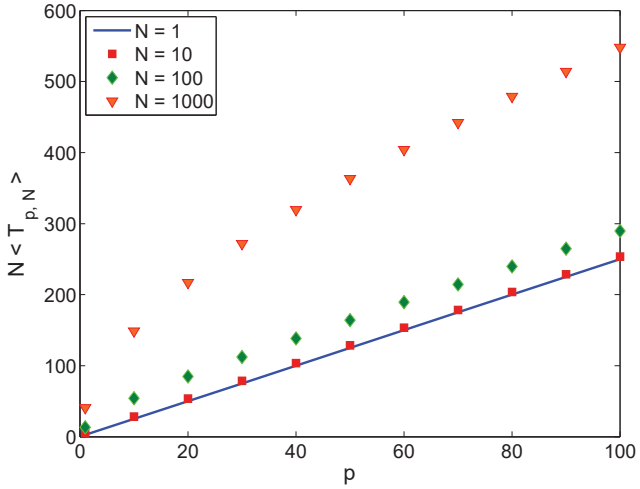

Figure 3.10: Plots of turnover times $\langle T_{p,N} \rangle$ scaled by the number of enzymes. If N renewal processes were pooled, then the time to the p-th turnover would increase linearly with p, as indicated by the black line. The N-enzyme non-renewal process shows nonlinear variation, as indicated by the symbols. We find that the higher the number of enzymes involved, the slower the turnover process gets. Parameter values are $k_1/k_2 = 1$, $k_{-1}/k_2 = 0.5$ and all times are in units of $1/k_2$.

3.7 Slowing down of kinetics

If we were to pool N independent single enzyme trajectories, each a renewal process, the mean turnover time of the resulting pooled process would be reduced exactly by a factor of N. However, for a nonrenewal process with N enzymes, Figs. (3.5) and (3.10) show that the mean time is larger than the pooled estimate, indicating a slowing down of the kinetics. In other words, we find that $\langle T_{p,N} \rangle > \dfrac{T_{p,1}}{N}$. This slowing down phenomenon might be related to the cooperative behaviour of the enzymes producing the anti-correlations between subsequent turnovers. However, the precise molecular mechanism by which this cooperativity is realized is a very interesting question, but cannot be answered within the mass action kinetics description we have employed here.

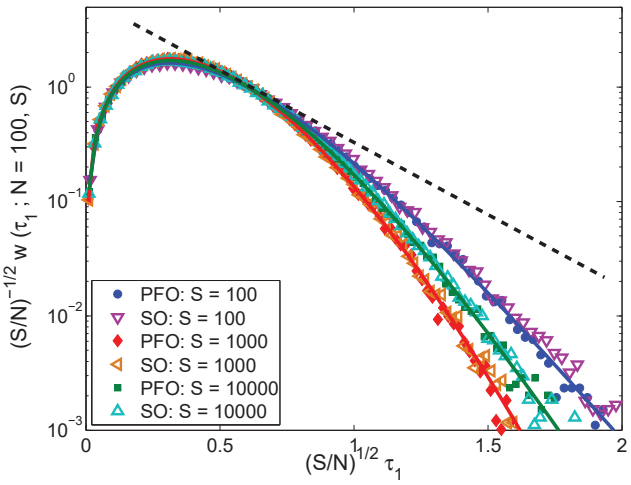

Figure 3.11: Validity of the pseudo-first-order approximation. Here we plot, in log-linear scale, the distribution of the first waiting time for $N = 100$ for various values of S. Filled and unfilled symbols are numerical simulations of pseudo-first order (PFO) and second order (SO) kinetics, respectively, whereas solid lines are analytical results for the PFO case [64, 65]. The black dashed line is a guide to the eye to indicate non-exponential tails. We find little difference between the two simulations, even for the $S \sim N$ case. The scaling of the abscissa and the ordinate by $(S/N)^{1/2}$ and $(S/N)^{-1/2}$ respectively makes the distributions collapse at early times. Parameter values are $k_1/k_2 = 0.01$, $k_{-1}/k_2 = 0.5$ and all times are in units of $1/k_2$.

3.8 Validity of PFO kinetics

To validate our pseudo-first order kinetics approximation, we compared turnover time distributions for both pseudo-first order kinetics (present work) and for second-order kinetics (the master equation for which was first presented by Bartholomay [70]). The comparison for $\langle T_1 \rangle$ is shown in Fig. (3.11). There is negligible difference between the two results, even when $S \sim N$. Differences continue to be negligible for early and intermediate turnovers. It is only at the very late stages that the difference between pseudo-first order and second-order kinetics becomes apparent, since the latter has an absorbing state at $S = N$, while the former does not. Therefore, from this comparison, the limitation of the pseudo-first order approximation becomes apparent only at late times. Since the MM equation is typically applied at early times, this difference at late times is of secondary importance to our work. In vivo concentrations of substrates and enzymes support this

treatment. Albe et al. list the substrate-enzyme ratios for about 140 enzymes [58]. In 88% of the cases, the ratios are one or larger. Of the 17 cases where substrate-enzyme ratios are smaller than one, 16 occur in glycolysis. This justifies our use of the approximation.

3.9 Conclusion

The non-renewal properties of enzymatic turnovers presented here can be verified by fluorescence experiments with well-mixed reactants. Fluctuations of intermediate states which must be summed over lead to multi-exponential waiting time distributions for the product and to the correlations between waiting times. These non-renewal aspects should appear in other models of catalysis which involve several types of enzyme-substrate intermediates. Fluctuations of intermediate states can also provide a model for dynamic disorder, which has previously been modelled by fluctuating reaction rates. For second-order kinetics with substrate fluctuations [70], we numerically compute low order waiting time distributions and find negligible differences with our results. This justifies our use of pseudo-first order kinetics, which remains a reliable approximation at early times even when substrates fluctuate. In conclusion, the main implication of our work is that enzyme kinetics must be approached as a non-renewal stochastic process in time with fluctuations at multiple time scales.

Chapter 4

Oscillations in an epidemic model due to intrinsic noise

In this chapter we analyze the generation of quasicycles due to internal noise, as well as the non-trivial variation of the quality of oscillation with respect to population size, in a closed epidemic model under the homogeneous mixing assumption. The closed system is relevant in many epidemiological situations, for instance in boarding houses [71], or island communities, where no inflows or outfluxes occur. Further, the conservation of population, as implied by a closed system, allows one to deal with a lower-dimensional problem. We exploit this in a systematic manner and show how the master equation can be marginalized using the conservation constraint. The existence of an endemic fixed point allows a two-stage linearization procedure to be carried out on the model. The linear noise approximation, followed by a further linearization about the endemic fixed point, reduces the model to the standard multivariate Ornstein-Uhlenbeck (OU) form. Exploiting the linear and Gaussian character of the multivariate OU process then allows for stochastic behaviour to be predicted from the deterministic part of the dynamics, in a spirit similar to the Onsager regression method of equilibrium statistical mechanics.

4.1 Mathematical modelling of epidemics

Two and a half centuries ago, D. Bernoulli [72] used a nonlinear ordinary differential equation to study the effect of cow-pox inoculation on the spread of smallpox. This was one of the earliest examples of the mathematical study of epidemics. This field of study continues to hold the interest of the scientific community especially in the light of recent outbreaks of viral pandemics like SARS and H1N1. Kermack and McKendrick in their seminal paper [73] put forward the classic Susceptible-Infected-Recovered (SIR) model of the spread of epidemics which, like most early epidemic models, assumes a homogeneously mixed population. More recent work focuses on the geotemporal spread of epidemics, especially on model networks [74, 75]. However, homogeneous mixing models still prove to be useful [76] and have been used to study various outbreaks of diverse size, fatality and chronology. Examples range from the study of the plague in the village of Eyam in 1665-66 [77] to the Bombay plague of 1905-06 [73] and the influenza epidemic in an English boarding school [71].

Mathematical models like the SIR model are usually analyzed deterministically and are only exactly valid when the size of the population under consideration is exceedingly large. Fluctuations due to finite population sizes or due to external causes can give rise to phenomena which cannot be captured by deterministic mean-field models and necessitates the use of stochastic models. Bartlett [78, 44] was one of the first to realize that a stochastic description was necessary to explain the periodic recurrence of measles, a phenomenon which could not be explained by deterministic models [79, 80]. Bartlett formulated [78] a stochastic version of the SIR model to describe the periodic recurrence of measles.

The mechanism for the generation of sustained oscillations in population dynamics has been analyzed within the stochastic framework [81] which concentrates on external fluctuations as the noise source. However, finite-sized populations give rise to fluctuations whose relative amplitude is of the order of the inverse of the square root of the size of the

population [2]. The role played by this internal noise, arising out of demographic stochasticity, in the generation of sustained oscillations has been studied in a prey-predator model using a master equation approach by McKane and Newman [15]. They have used the expansion method due to van Kampen [31] in their analysis, which provides a systematic way of deriving the phenomenological equations due to Bartlett [78]. Alonso *et al.* [82] used similar techniques in an open model of infectious diseases within the homogeneous mixing assumption, while Rozhnova and Nunes [83] applied systematic expansion to a closed epidemic model on networks, using a pair approximation. The oscillations generated and sustained by internal noise are called *endogenous resonant quasicycles* and are qualitatively different from stochastic oscillations forced by external periodicities which are *exogenous* [84]. The quality or coherence of these oscillations are intuitively expected to vary monotonically with the size of the population or equivalently, the relative noise amplitude. However, it has been observed in various theoretical models including the Fitz Hugh-Nagumo [85] and gene circuit models [86] that the regularity or coherence of oscillations is small for low and high noise amplitudes and reaches a maximum for an intermediate value. This phenomenon is called stochastic coherence or coherence resonance and has also been observed in optical laser experiments [87].

4.2 SIRS linear deterministic analysis

The classic SIR model for infectious diseases (S stands for susceptibles, I for infected and R for recovered) considers the population to be homogeneously mixed and constant in total number [73]. The SIRS model is a variant of the SIR model where the recovered section of the population lose their immunity after a delay and become susceptible. The nonlinear ODE system of the form $\dot{\mathbf{n}} = \mathbf{f}(\mathbf{n})$, where $\mathbf{n} = \{S, I, R\}$, describing the SIRS

model is constrained by the fixed population size Ω and is hence a closed system.

$$\begin{aligned} \dot{S} &= \alpha R - \beta S I \\ \dot{I} &= \beta S I - \gamma I \\ \dot{R} &= \gamma I - \alpha R \end{aligned} \tag{4.1}$$

The rate of infection is β, the rate of recovery is γ while α is the rate of loss of immunity. The fixed point ($\mathbf{n} = \mathbf{n}^*$) is given by

$$(S^*, I^*, R^*) = \left[\frac{\gamma}{\beta}, \frac{\alpha}{\beta}\left(\frac{\beta\Omega - \gamma}{\alpha + \gamma}\right), \frac{\gamma}{\beta}\left(\frac{\beta\Omega - \gamma}{\alpha + \gamma}\right)\right] \tag{4.2}$$

The steady state with zero infected is not of interest in the present study. The fixed point is endemic with non-zero infected in the steady state ($I^* > 0$) when the condition $\beta\Omega > \gamma$ is satisfied.

Since there is a constraint in the system, $S + I + R = \Omega$, the 3×3 system is effectively a 2×2 system with $R = \Omega - S - I$.

$$\begin{aligned} \dot{S} &= \alpha(\Omega - S - I) - \beta S I \\ \dot{I} &= \beta S I - \gamma I \end{aligned} \tag{4.3}$$

The dynamics of small perturbations, $\delta\mathbf{n} = \{\delta S, \delta I\}$, about the fixed point are described by the linear ODE system $\delta\dot{\mathbf{n}} = \mathbf{A} \cdot \delta\mathbf{n}$. Here $A_{ij} = \partial f_i / \partial n_j|_{\mathbf{n}=\mathbf{n}^*}$ is the Jacobian matrix at the fixed point and is given by

$$\mathbf{A} = \begin{bmatrix} -\alpha\left(\dfrac{\alpha + \beta\Omega}{\alpha + \gamma}\right) & -(\alpha + \gamma) \\ \alpha\left(\dfrac{\beta\Omega - \gamma}{\alpha + \gamma}\right) & 0 \end{bmatrix} \tag{4.4}$$

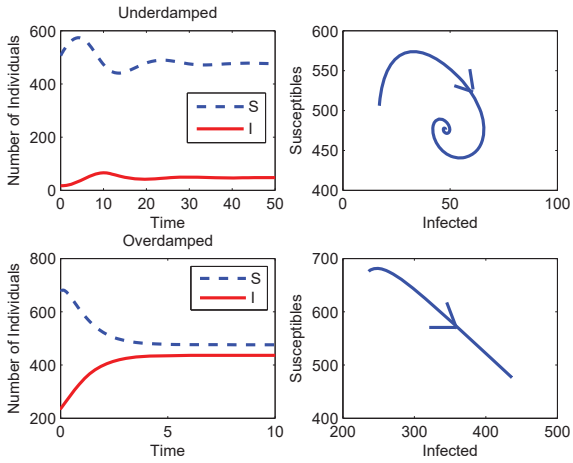

Figure 4.1: Underdamped and overdamped decay of perturbations. The top two plots show underdamped decay with parameter values $\beta = 0.0021, \alpha = 0.1, \gamma = 1.0$ and population size $\Omega = 1000$ (where the Jacobian has complex eigenvalues). The bottom two plots show overdamped decay with parameter values $\beta = 0.0021, \alpha = 5.0, \gamma = 1.0$ and population size $\Omega = 1000$ (where the Jacobian has real eigenvalues). The S vs I plot for underdamped decay shows a spiral while that for overdamped decay does not. The former is a stable spiral while the latter is a stable node.

Its eigenvalues are

$$\lambda_{\pm} = \frac{1}{2}\left[-\alpha\left(\frac{\alpha+\beta\Omega}{\alpha+\gamma}\right) \pm \sqrt{\alpha^2\left(\frac{\alpha+\beta\Omega}{\alpha+\gamma}\right)^2 - 4\alpha(\beta\Omega-\gamma)}\right] \tag{4.5}$$

the real parts of which are always negative for an endemic steady state since $\beta\Omega > \gamma$. Hence the endemic fixed point is always asymptotically stable. Perturbations about the fixed point decay monotonically if the eigenvalues are purely real and in an oscillatory fashion if they are complex. These correspond, respectively, to overdamped and underdamped decay. In Fig. (4.1), we plot both time traces and phase portraits of S and I showing the underdamped and overdamped cases. Fig. (4.2) is a state diagram of the model, showing the ratio $|\mathrm{Im}(\lambda)/\mathrm{Re}(\lambda)|$. The region of complex eigenvalues, corresponding to underdamped decay, is bounded by the contours labelled by $|\mathrm{Im}(\lambda)/\mathrm{Re}(\lambda)| = 0$.

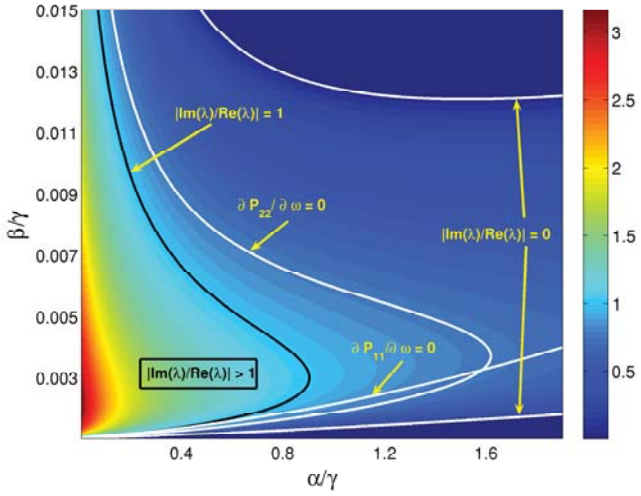

Figure 4.2: Plot of the absolute value of the ratio of the imaginary and real parts of the eigenvalues λ of the linearized Jacobian matrix $\mathbf{A}$ against the dimensionless parameters β/γ and α/γ and population size $\Omega = 1000$. The outermost white contours, labeled "$|\mathrm{Im}(\lambda)/\mathrm{Re}(\lambda)| = 0$", enclose the region where the eigenvalues are complex, which is a necessary condition for the existence of quasicycles. The imaginary parts of the eigenvalues are zero in the outermost two regions of the plot. The inner white contours, labeled "$\partial P_{11}(\omega)/\partial\omega = 0$" and "$\partial P_{22}(\omega)/\partial\omega = 0$", enclose the regions for which the PSD shows a peak. This is a sufficient condition for the existence of quasicycles. The innermost black contour, denoting $|\mathrm{Im}(\lambda)/\mathrm{Re}(\lambda)| = 1$ and marked as such, encloses the region where the quasicycles are of sufficient strength to be reliably detected. This region is labeled "$|\mathrm{Im}(\lambda)/\mathrm{Re}(\lambda)| > 1$", which is a necessary and sufficient condition for the reliable detection of quasicycles. Each condition presented above is stricter than the previous, leading to a nesting of regions of parameter space as regards the existence and detection of quasicycles.

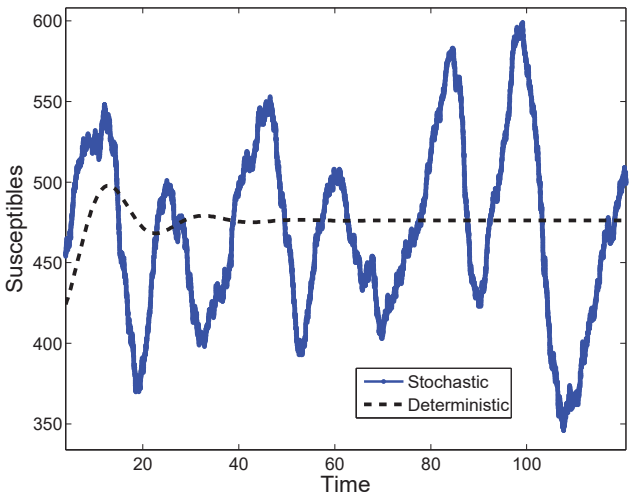

Figure 4.3: Numerical simulation of susceptibles overlaid on deterministic underdamped decay. Parameters are $\beta = 0.0021, \alpha = 0.1, \gamma = 1.0$ and population size $\Omega = 1000$. There are noise-induced oscillations in the stochastic case which are not seen in the deterministic analysis. The time period of oscillations is approximately 20 in units of $1/\gamma$ (simulations have been performed after non-dimensionalization). This corresponds well with the frequency seen (Fig. 4.4) in the PSD analysis for the same set of parameter values.

4.3 SIRS linear stochastic analysis

Relative fluctuations about the deterministic expected values vary as the inverse of the square root of the number of interacting entities and thus become important when the entities are few in number. Often one finds that this is indeed the case in biological systems [2]. Our present study concerns populations where fluctuations due to demographic stochasticity cannot be ignored and mean-field deterministic analysis fails to capture its non-trivial contributions. It then becomes necessary to employ stochastic methods to reliably understand the role of fluctuations.

We begin by writing down the birth-death master equation (ME) of the SIRS model. Let the state of the system at any time t be given by the vector $\mathbf{n} = (n_1, n_2, n_3)$ where n_i is the number of individuals in each class ($i = 1$ for S, $i = 2$ for I and $i = 3$ for R). The general

birth-death ME is then [37]

$$\frac{\partial P(\mathbf{n},t)}{\partial t} = \sum_{\alpha} \{t_{\alpha}^{-}(\mathbf{n}+\mathbf{r}_{\alpha})P(\mathbf{n}+\mathbf{r}_{\alpha},t) - t_{\alpha}^{+}(\mathbf{n})P(\mathbf{n},t)\} + \sum_{\alpha} \{t_{\alpha}^{+}(\mathbf{n}-\mathbf{r}_{\alpha})P(\mathbf{n}-\mathbf{r}_{\alpha},t) - t_{\alpha}^{-}(\mathbf{n})P(\mathbf{n},t)\} \tag{4.6}$$

Here $P(\mathbf{n},t)$ is the conditional probability for the system to be in the state $\mathbf{n}$ given some fixed initial state, t_{α}^{+} and t_{α}^{-} are the birth and death rate terms and $\mathbf{r}_{\alpha}$ is the vector denoting the change in the number of entities in the α-th reaction. For the SIRS model we have

$$\begin{aligned} &t_1^{+} = \beta n_1 n_2; \;\; t_2^{+} = \gamma n_2; \;\; t_3^{+} = \alpha n_3; \;\; t_1^{-} = t_2^{-} = t_3^{-} = 0 \\ &\mathbf{r}_1 = (-1,+1,0); \;\; \mathbf{r}_2 = (0,-1,+1); \;\; \mathbf{r}_3 = (+1,0,-1) \end{aligned} \tag{4.7}$$

The variable $N(t) = n_1(t) + n_2(t) + n_3(t)$ is constrained by the fixed population size Ω. Incorporating this constraint within the ME allows us to work with a 2×2 system. The partial time derivative of $P(N(t),t)$ vanishes if $N(t) = \Omega$ for all t. We marginalize with respect to one of the variables (here we choose n_3) taking the population size as parameter: $P(n_1,n_2,t\,|\,\Omega) = \sum_{n_3} \delta_{n_1+n_2+n_3,\Omega}\, P(\mathbf{n},t)$. Modifying the birth terms and the state change vectors appropriately, *i.e.* replacing n_3 by $\Omega - n_1 - n_2$ and writing the $\mathbf{r}_{\alpha}$ as 2×1 vectors, we get the marginalized ME.

$$\begin{aligned} \frac{\partial P(n_1,n_2,t\,|\,\Omega)}{\partial t} &= \beta(n_1+1)(n_2-1)P(n_1+1,n_2-1,t\,|\,\Omega) + \gamma\,(n_2+1)\,P(n_1,n_2+1,t\,|\,\Omega) \\ &+ \alpha\,(\Omega - n_1 - n_2 + 1)P(n_1-1,n_2,t\,|\,\Omega) - \{\beta n_1 n_2 + \gamma n_2 + \alpha\,(\Omega - n_1 - n_2)\}\,P(n_1,n_2,t\,|\,\Omega) \end{aligned} \tag{4.8}$$

The transition probability for the infection step is non-linear and as such the ME is not solvable analytically. However, it is possible to simulate the ME using the Doob-Gillespie stochastic simulation algorithm (SSA) [39, 45, 46]. This generates an exact sampled trajectory of the jump stochastic process described by the ME. We non-dimensionalize time by working in units of $1/\gamma$. Figure (4.3) shows the numerical simulation of the

susceptibles using the SSA, compared with a deterministic solution of the ODE system. The demographic fluctuations induce and sustain approximate cycles in the populations, a feature absent in the deterministic model.

In the absence of exact solutions, we try to characterize these fluctuations within an approximation method due to van Kampen [31] which replaces the jump process with a stationary multivariate Ornstein-Uhlenbeck process. The Gaussian nature of the process can then be utilized to obtain analytical solutions for the fluctuation properties, while the linear nature of the process can be utilized to make connections between the deterministic and fluctuating dynamics.

We expand the variables in the population size Ω (the large parameter of the approximation method) so that the size of the jumps decreases as the population is increased,

$$\mathbf{n} = \Omega\,\overline{\mathbf{n}} + \Omega^{1/2}\mathbf{x} \tag{4.9}$$

where $\overline{\mathbf{n}}$ is the mean value of $\mathbf{n}$ and $\mathbf{x}$ denotes the fluctuations around the mean. Assuming the fluctuations obey a diffusion process about the mean yields a Fokker-Planck equation (FPE) for the fluctuations,

$$\partial_t P(\mathbf{x},t) = -\partial_i \left[A_i(\mathbf{x})P(\mathbf{x},t)\right] + \frac{1}{2}\partial_i\partial_j\left[B_{ij}(\mathbf{x})P(\mathbf{x},t)\right] \tag{4.10}$$

where repeated indices indicate summation, $\partial_t = \partial/\partial t$ and $\partial_i = \partial/\partial x_i$. This is the linear noise approximation. The elements of the drift vector $\mathbf{A}(\mathbf{x})$ and the diffusion matrix $\mathbf{B}(\mathbf{x})$ are given, following the prescription in Gardiner [37], as

$$A_i(\mathbf{x}) = \sum_{\alpha=1}^{2} r_\alpha^i t_\alpha^+(\mathbf{x}) \qquad\qquad B_{ij}(\mathbf{x}) = \sum_{\alpha=1}^{2} r_\alpha^i r_\alpha^j t_\alpha^+(\mathbf{x}) \tag{4.11}$$

($i, j = 1, 2$ being the component indices). Linearizing a second time about the endemic

fixed point we get the FPE of a stationary multivariate Ornstein-Uhlenbeck process

$$\partial_t P(\mathbf{x}, t) = -\sum_{i,j}\left[A_{ij}\partial_i\left\{x_j P(\mathbf{x}, t)\right\} - \frac{1}{2}B_{ij}\partial_i\partial_j P(\mathbf{x}, t)\right] \tag{4.12}$$

where A_{ij} and B_{ij} are the elements of the linearized drift and diffusion matrices. For the SIRS model, their values are (from Eq. (4.11) after putting $\mathbf{x} = \mathbf{x}^*$)

$$\mathbf{A} = \begin{bmatrix} -\alpha\left(\frac{\alpha+\beta\Omega}{\alpha+\gamma}\right) & -(\alpha+\gamma) \\ \alpha\left(\frac{\beta\Omega-\gamma}{\alpha+\gamma}\right) & 0 \end{bmatrix} \tag{4.13}$$

$$\mathbf{B} = \frac{\alpha\gamma}{\beta}\left\{\frac{\beta\Omega-\gamma}{\alpha+\gamma}\right\}\begin{bmatrix} 2 & -1 \\ -1 & 2 \end{bmatrix} \tag{4.14}$$

We note that this linearized drift matrix $\mathbf{A}$ is identical to the linearized Jacobian matrix (Eq. 4.4) obtained from the deterministic analysis and hence the two matrices share the same spectrum. This allows us to predict, under the two-stage linearization procedure, the existence of non-trivial stochastic phenomena like noise-induced quasicycles and stochastic coherence purely from a deterministic analysis of the spectral structure of the linearized Jacobian. We shall discuss this important point in greater detail in Secs. 4.4 and 4.5. This also allows us to use the terms "linearized drift matrix" and "linearized Jacobian matrix" interchangeably.

The multivariate Ornstein-Uhlenbeck process has exact solutions for both stationary and transition probability densities. Both are multivariate Gaussians, fixed by the equal time covariance matrix $\Sigma_{ij} = \langle\langle x_i x_j\rangle\rangle$ and the matrix of time correlations $C_{ij}(\tau) = \langle\langle x_i(t)x_j(t+\tau)\rangle\rangle$, where the double angular brackets denote the cumulant [31]. $\mathbf{\Sigma}$ can be obtained by solving the steady state Einstein relation [37, 31].

$$\mathbf{A\Sigma} + \mathbf{\Sigma A}^T + \mathbf{B} = 0 \tag{4.15}$$

This has the form of a matrix Lyapunov equation, and can be solved using a method first proposed by Barnett and Storey [88] in the context of linear control systems. We note that Eq. (4.15) can be written as the sum of a matrix and its transpose $\mathbf{S} + \mathbf{S}^T = 0$ where $\mathbf{S}$ is the anti-symmetric matrix $\mathbf{A\Sigma} + \frac{1}{2}\mathbf{B}$. We can solve for $\mathbf{S}$ in terms of $\mathbf{A}$ and $\mathbf{B}$ using the relation

$$\mathbf{AS} + \mathbf{SA}^T = \frac{1}{2}\left(\mathbf{BA}^T - \mathbf{AB}\right) \tag{4.16}$$

which is obtained by eliminating $\mathbf{\Sigma}$ from the Einstein relation and using the definition of $\mathbf{S}$. Since $\mathbf{S}$ is anti-symmetric, it is specified by a single parameter when it is of size 2×2. This parameter can be obtained directly from Eq. (4.16), since both $\mathbf{A}$ and $\mathbf{B}$ are two-dimensional matrices and are known. For higher dimensions, matrix decompositions are convenient when solving for $\mathbf{S}$.

For the SIRS model (using Eqs. 4.13 and 4.14), we have

$$\mathbf{S} = \left\{\frac{\gamma(\beta\Omega - \gamma)(\alpha^2 + 2\alpha\gamma + 2\gamma^2 + \alpha\beta\Omega)}{2\beta(\alpha + \gamma)(\alpha + \beta\Omega)}\right\}\begin{bmatrix} 0 & -1 \\ 1 & 0 \end{bmatrix} \tag{4.17}$$

Knowing $\mathbf{S}$, $\mathbf{A}$ and $\mathbf{B}$ we can now write down the covariance matrix

$$\mathbf{\Sigma} = \mathbf{A}^{-1}\left(\mathbf{S} - \frac{1}{2}\mathbf{B}\right) \tag{4.18}$$

which for the SIRS model is

$$\mathbf{\Sigma} = \frac{\gamma}{\beta}\begin{bmatrix} \dfrac{\alpha^2 + \gamma^2 + \alpha(\beta\Omega + \gamma)}{\alpha(\alpha + \beta\Omega)} & -1 \\ -1 & \dfrac{\alpha(\alpha + \beta\Omega)^2 + \gamma(\alpha + \gamma)(\beta\Omega - \gamma)}{\beta(\alpha + \gamma)^2(\alpha + \beta\Omega)} \end{bmatrix} \tag{4.19}$$

Having obtained the matrix $\mathbf{\Sigma}$, the matrix of time correlations follows as

$$\mathbf{C}(\tau) = \langle\langle \mathbf{x}(t)\mathbf{x}(t+\tau)\rangle\rangle = e^{\tau \mathbf{A}}\mathbf{\Sigma} \tag{4.20}$$

The stochastic SIRS model, in the linear noise approximation, is completely specified by $\mathbf{\Sigma}$ and $\mathbf{C}(\tau)$. In the next section we use quantities derived from these to examine the model for signatures of oscillatory behaviour.

4.4 Noise-induced oscillations: Endogenous Quasicycles

The trace of the variation of the populations with time shown in Fig. (4.3) is strongly suggestive of sustained oscillations. This can be verified quantitatively by measuring the power spectral density (PSD) of the population time series. A peak in the PSD indicates the presence of oscillations. The PSD matrix, in terms of the linearized drift and diffusion matrices for a multivariate Ornstein-Uhlenbeck process is

$$\mathbf{P}(\omega) = (-i\omega\mathbb{I} + \mathbf{A})^{-1}\,\mathbf{B}\,(i\omega\mathbb{I} + \mathbf{A}^T)^{-1} \tag{4.21}$$

where $\mathbb{I}$ is the identity matrix. The diagonal elements of this matrix give an estimate of the periodicity in the relevant variables (here S and I). The $\mathbf{P}_{ii}$ for the SIRS PSD are

$$\mathbf{P}_{ii}(\omega) = 2d\left(\frac{\Gamma_i + \omega^2}{\omega^4 + q\omega^2 + r}\right) \tag{4.22}$$

where

$$d = \{\alpha\gamma(\beta\Omega - \gamma)/\beta(\alpha + \gamma)\}, \tag{4.23a}$$

$$\Gamma_1 = (\alpha + \gamma)^2, \tag{4.23b}$$

$$\Gamma_2 = \alpha^2 \left\{\alpha^2 + \gamma^2 + \beta\Omega(\beta\Omega - \gamma) + \alpha(\beta\Omega + \gamma)\right\}/(\alpha + \gamma)^2, \tag{4.23c}$$

$$q = \alpha \left\{\alpha^2(\alpha + 2\gamma) - 2\gamma^2(\beta\Omega - \gamma) + \alpha(\beta\Omega - 2\gamma)^2\right\}/(\alpha + \gamma)^2, \tag{4.23d}$$

$$r = \alpha^2(\beta\Omega - \gamma)^2 \tag{4.23e}$$

In Fig. (4.4) we plot the PSD for both S and I, comparing numerical simulation with Eq. (4.22). A peak is clearly visible for parameters corresponding to underdamped dynamics. The peak disappears for overdamped dynamics as shown in the inset. The peak frequency (around $\omega_p = 0.3$) corresponds to the period ($T = 20$) of the numerical time-trace (Fig. 4.3). The excellent agreement between numerics and analytics provides a post facto justification of the linear noise approximation for this problem.

The PSD has peaks at real frequencies if and only if the extremum condition $\partial P_{ii}(\omega)/\partial\omega = 0$ has real roots. The regions of parameter space for which this occurs are bounded by contours labelled "$\partial P_{11}(\omega)/\partial\omega = 0$" and "$\partial P_{22}(\omega)/\partial\omega = 0$" in Fig. (4.2). These are sufficient conditions for the existence of quasicycles. This approach has been used previously in the literature to detect quasicycles [15, 82, 83].

While Fourier analysis of a signal is a natural tool for studying oscillatory behaviour, a corresponding time-domain analysis must yield equivalent results. The time-correlation function forms the basis of a time-domain analysis, which for the multivariate Ornstein-Uhlenbeck process is given by Eq. (4.20). The temporal variation of the time correlation is fixed entirely by the drift $\mathbf{A}$ which is the deterministic part of the dynamics, while its scale is set by $\mathbf{\Sigma}$ which involves the stochastic part of the dynamics through $\mathbf{B}$. Defining a normalized time correlation $\mathbf{c}(\tau) = \mathbf{C}(\tau)\mathbf{\Sigma}^{-1}$, we find that $\mathbf{c}(\tau) = e^{\tau\mathbf{A}}$. This is of the form $c(\tau) \sim \exp[\mathrm{Re}(\lambda)\tau]\sin[\mathrm{Im}(\lambda)\tau)]$. This observation motivates the use of the ratio

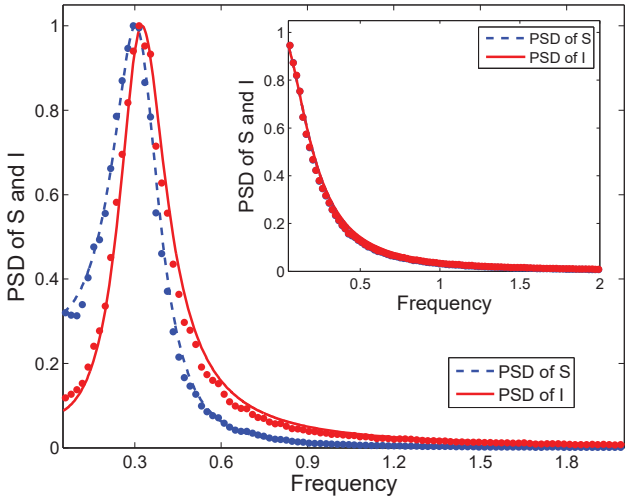

Figure 4.4: Normalized power spectral density for susceptibles and infected. There is excellent agreement between the analytically calculated (dashed blue for S, solid red for I) and numerically computed (blue dots for S, red dots for I) PSDs, thus justifying the linear noise approximation. The main graph is for parameter values $\beta = 0.0021, \alpha = 0.1, \gamma = 1.0$ at population size $\Omega = 1000$ which falls within the underdamped zone. The PSD peaks around frequency $\omega = 0.3$, which corresponds approximately to the time period of the numerical signal as well as that of the ACF for the same set of parameter values (see Figs. 4.3 and 4.5). The inset shows the PSD for the same size of the population at parameter values $\beta = 0.0012, \alpha = 2.5, \gamma = 1.0$ which falls within the overdamped zone and does not show any peak.

$|\mathrm{Im}(\lambda)/\mathrm{Re}(\lambda)|$ to reliably detect quasicycles within the linear noise approximation, where $\lambda = \mathrm{eig}(\mathbf{A})$. If the decay time scale, fixed by $\mathrm{Re}(\lambda)$, is too short compared to the oscillatory time scale fixed by $\mathrm{Im}(\lambda)$, the decay will dominate and oscillatory effects will not be discernible. This will be so even when the extremum condition has real roots. We thus propose a condition for clearly discernible quasicycles, namely $|\mathrm{Im}(\lambda)/\mathrm{Re}(\lambda)| \geq 1$. In Fig. (4.2) we plot the contour $|\mathrm{Im}(\lambda)/\mathrm{Re}(\lambda)| = 1$. The region $|\mathrm{Im}(\lambda)/\mathrm{Re}(\lambda)| > 1$ is bounded on the right by this contour. As this is more stringent than the extremum condition $\partial P_{ii}(\omega)/\partial\omega = 0$, it is entirely contained by the regions where the PSD has a peak. In Fig. (4.5) we emphasize this point by comparing the autocorrelation function (ACF) when the PSD has peaks at finite frequencies. When $|\mathrm{Im}(\lambda)/\mathrm{Re}(\lambda)|$ is small the oscillations are barely discernible, as seen from the rapid decay of the ACF. For $|\mathrm{Im}(\lambda)/\mathrm{Re}(\lambda)|$ of order unity clear signatures of oscillation are visible in the ACF.

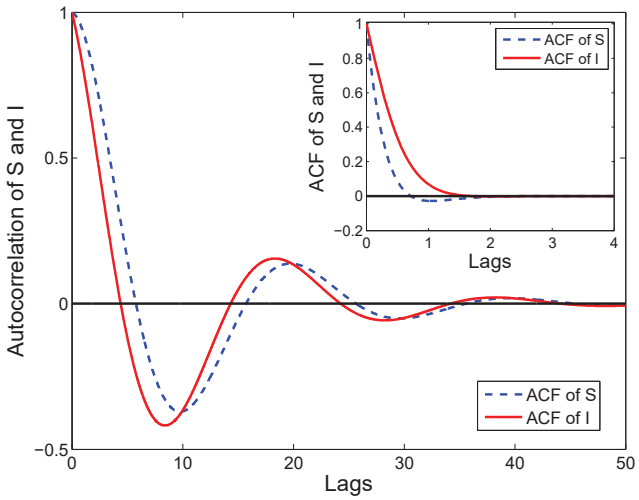

Figure 4.5: Normalized autocorrelation of susceptibles and infected for parameter values $\beta = 0.0021, \alpha = 0.1, \gamma = 1.0$ and population size $\Omega = 1000$ which falls within the $|\mathrm{Im}(\lambda)/\mathrm{Re}(\lambda)| > 1$ zone. The thick black line is the x-axis. There is clear oscillatory decay with a period of approximately 20 in units of $1/\gamma$ which agrees well with Figs. (4.3) and (4.4) for the same set of parameter values. The inset plot shows the ACF for parameter values $\beta = 0.009, \alpha = 1.2, \gamma = 1.0$ and population size $\Omega = 1000$ which falls within the zone bounded by the contours $\partial P_{11}(\omega)/\partial\omega = 0$, $\partial P_{22}(\omega)/\partial\omega = 0$ and $|\mathrm{Im}(\lambda)/\mathrm{Re}(\lambda)| = 0$, *i.e* the region where susceptibles should cycle according to the PSD analysis. The thick black line is once again the x-axis. There is a single zero-crossing of the ACF for S, which indicates non-oscillatory decay [84]. This shows the unreliability of PSD analysis in detecting quasicycles. These analytical plots have also been compared with numerical data (not shown here) with good agreement.

4.5 Quality of noise-induced oscillations: Stochastic coherence

Noise-induced oscillations, unlike genuine oscillations, are not phase coherent and as such are called quasicycles. The coherence or regularity of quasicycles can be quantified by several measures. Here we use the quality factor, which measures the sharpness of the peak of the PSD, and the coefficient of variation, which measures the regularity of the zero crossing of the signals.

The quality factor, Q, is a dimensionless parameter that characterizes an oscillator's bandwidth relative to its peak frequency,

$$Q = \omega_p/\Delta\omega \tag{4.24}$$

where ω_p is the peak frequency and $\Delta\omega$ is the bandwidth. A high Q corresponds to oscillations of greater regularity. We calculate the Q for the diagonal entries of the PSD matrix. Let k_i be half the maximal power $k_i = \frac{1}{2}P_{ii}(\omega_p^i)$ for each $i = 1, 2$. We calculate the bandwidth or the full-width at half-maximum (FWHM) using the k_i and Eq. (4.22) to get

$$(\Delta\omega)_i = \sqrt{(2d/k_i - q) - 2\sqrt{r - 2d\Gamma_i/k_i}} \tag{4.25}$$

Using Eq. (4.22), the peak frequencies are given by the positive square roots of the positive roots of the two quadratic equations $z^2 + 2\Gamma_i z + (\Gamma_i q - r) = 0$ (for $i = 1, 2$) where $z = \omega^2$ and Γ_i, q and r are as defined in the previous section. The peak frequency and the FWHM together give the Q. Figure 4.6 shows a scan of the quality factor against population size and against the inverse of population size (inset). As one would expect, Q is low for high noise amplitudes and starts increasing as the noise decreases, keeping in mind that the relative noise amplitude varies as the inverse of the square root of the size of the population. However, the graph then has a maximum and then decreases for

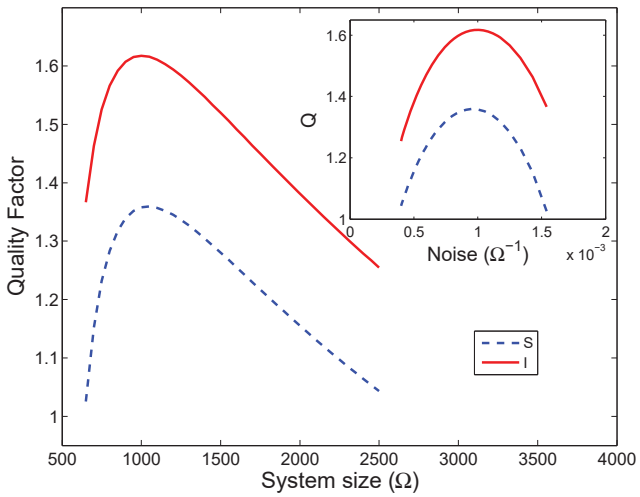

Figure 4.6: Quality factor for the susceptibles (plotted for 200 runs) against population size (Ω) and (inset) against inverse of population size. Parameter values are $\beta = 0.0021, \alpha = 0.1, \gamma = 1.0$. The peaks for S and I are respectively at $\Omega = 1040$ and $\Omega = 1000$.

high amplitudes of noise. This is stochastic coherence. The coefficient of variation, C_V, is the ratio of the variance and the mean of the times T between successive zeros of a temporal signal. A sharp peak in the histogram of the intervals between zero crossings, then, indicates a strongly coherent signal. C_V is a dimensionless measure of this,

$$C_V = \frac{\sqrt{\langle T^2 \rangle - \langle T \rangle^2}}{\langle T \rangle} \tag{4.26}$$

A low C_V indicates a high degree of coherence in the signal. Similar measures are used in the literature (for example [85] and [86]). Figure 4.7 shows the C_V for the mean crossing time of the numerical signal of the susceptibles scanned against population size and (inset) against its inverse . The plot shows a minimum which indicates stochastic coherence and hence numerically supports the analytical result given by the Q.

Although this non-intuitive variation of the coherence of the quasicycles with the size of the population has a stochastic origin, it is controlled purely by the deterministic part of the dynamics. The analysis using the Q and the C_V require a knowledge of the diffusion

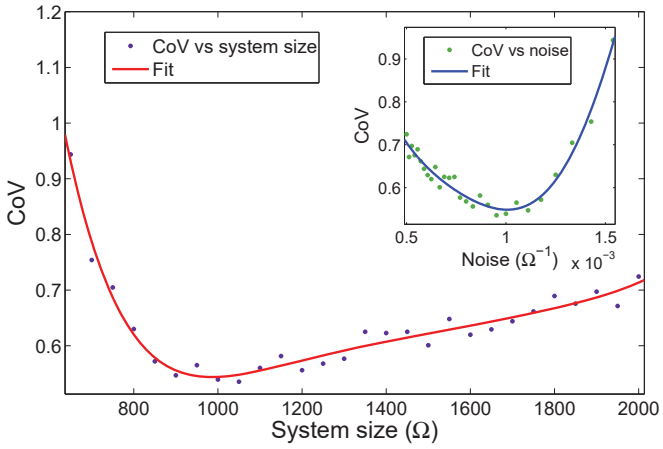

Figure 4.7: Coefficient of Variation for the susceptibles (plotted for 200 runs) against population size (Ω) and (inset) against inverse of population size. The solid line is a fifth-order polynomial fit. Parameter values are $\beta = 0.002, \alpha = 0.1, \gamma = 1.0$. The C_V peak for S, computed from the minimum of the fifth-order polynomial fit, is at $\Omega = 985$. The C_V plot for the infected (not given here) shows a peak (in the sixth-order fit used there) at $\Omega = 1135$. This agrees well with the peaks obtained for the plot of the quality factor, Fig. (4.6).

matrix **B**. However, after the two-step linearization procedure, the entire non-trivial dependence on the population size is contained only in the spectrum of the linearized drift matrix, while the diffusion matrix scales linearly with Ω, as given by Eqs. (4.13) and (4.14). Thus, any non-monotonicities in the fluctuations arise purely from the deterministic part of the dynamics, while the noise merely excites these modes. For a system which can be reduced to a standard multivariate Ornstein-Uhlenbeck process, the linearized drift matrix is identical to the linearized Jacobian matrix. This motivates the use of the ratio $|\mathrm{Im}(\lambda)/\mathrm{Re}(\lambda)|$ in determining the size of the population at which stochastic coherence is observed. This allows us to study stochastic coherence from the deterministic part of the dynamics.

We observe that in Fig. (4.8) the ratio $|\mathrm{Im}(\lambda)/\mathrm{Re}(\lambda)|$, when scanned against the size of the population (Ω), shows a peak which occurs at $\Omega = 1000$ for parameter values $\beta = 0.0021$, $\alpha = 0.1$ and $\gamma = 1.0$. We see that this value matches well with the peaks in Figs. 4.6 and 4.7, within numerical errors. We have calculated the peak value of the ratio in terms of

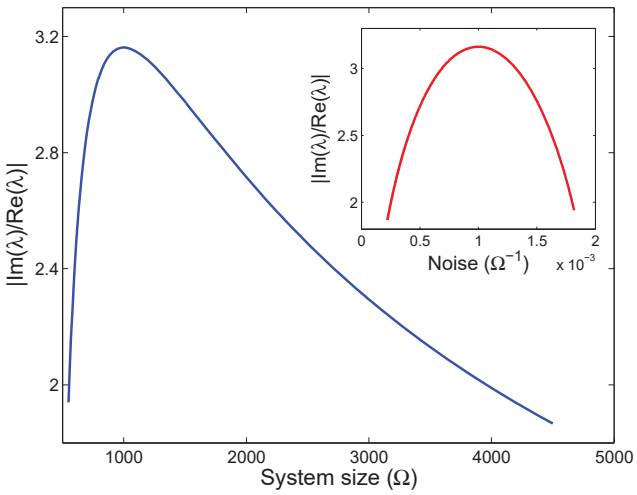

Figure 4.8: Absolute value of the ratio of the imaginary and real parts of the eigenvalues of the linearized Jacobian matrix plotted against population size (Ω) and (inset) against inverse of population size. Parameter values are $\beta = 0.0021, \alpha = 0.1, \gamma = 1.0$. There is a peak at $\Omega = 1000$ corresponding to the stochastic coherence point, which agrees quite well with the values provided by the quality factor and coefficient of variation plots, Figs. (4.6) and (4.7).

the model parameters. If Ω_p is the population size at stochastic coherence, then

$$\Omega_p = \frac{\alpha + 2\gamma}{\beta} \tag{4.27}$$

Since the ratio is always positive, there is stochastic coherence for all values of parameters for which quasicycles exist. We have previously observed a similar curious maximization of orderliness at intermediate noise amplitudes in Chapter (3).

4.6 Detailed balance violation necessary for quasicycles

Quasicycles and stochastic coherence are not possible unless detailed balance is violated in the master equation. Typically, variables characterizing biological systems are even under time-reversal, $x(-t) = x(t)$, and this is true for the variables of the SIRS model. If the system is in state $\mathbf{n}_0$ at time $t_0 = 0$ (say) and is in state $\mathbf{n}$ at some later time t, then the

joint probability of the forward transition ($\mathbf{n}_0(t_0) \rightarrow \mathbf{n}(t)$) is $P(\mathbf{n}, t; \mathbf{n}_0, 0)$ while that of the reverse transition ($\mathbf{n}(t_0) \rightarrow \mathbf{n}_0(t)$) is $P(\mathbf{n}_0, t; \mathbf{n}, 0)$, provided all time-reversal parities are even. Microscopic reversibility implies that at equilibrium the steady state forward and reverse joint probabilities must be equal. This is the condition for detailed balance and for a Markov process can be written as

$$P(\mathbf{n}, t|\mathbf{n}_0, 0)P_s(\mathbf{n}_0) = P(\mathbf{n}_0, t|\mathbf{n}, 0)P_s(\mathbf{n}) \tag{4.28}$$

where the subscript 's' denotes steady state. Expressing this condition macroscopically in terms of the correlation function, expanding in Taylor series, and keeping the first order terms one obtains [89] the Onsager relations

$$\mathbf{A\Sigma} = \mathbf{\Sigma A}^T \tag{4.29}$$

which is the macroscopic condition for equilibrium. This condition requires the drift matrix to be related by a similarity transformation to a symmetric matrix [37] and hence restricts its spectrum to the real axis. Since it is not possible to have quasicycles without having complex eigenvalues, the violation of detailed balance is a necessary condition for the existence of noise-induced oscillations, and has been observed earlier in predator-prey systems [90].

Recalling that $\mathbf{S} = \mathbf{A\Sigma} + \frac{1}{2}\mathbf{B}$ and using the symmetry properties of $\mathbf{\Sigma}$ and $\mathbf{B}$ we can write down the following expression for $\mathbf{S}$ [91]

$$\mathbf{S} = \frac{1}{2}(\mathbf{A\Sigma} - \mathbf{\Sigma A}^T) \tag{4.30}$$

which is a measure of the deviation from detailed balance. The SIRS $\mathbf{S}$ matrix (Eq. 4.17) can never be zero for any choice of parameters under the endemic condition $\beta\Omega > \gamma$. Thus the SIRS model always violates detailed balance and therefore allows for quasicycles for any choice of parameters.

The steady state probability current $\mathbf{J}_s(\mathbf{x})$ for the multivariate OU process obeys $\boldsymbol{\nabla}\cdot\mathbf{J}_s = 0$ and is given by the equation

$$\mathbf{J}_s(\mathbf{x}) = P_s(\mathbf{x})\left(\mathbf{A} + \frac{1}{2}\mathbf{B}\boldsymbol{\Sigma}^{-1}\right) = P_s(\mathbf{x})\left(\mathbf{S}\boldsymbol{\Sigma}^{-1}\right)\mathbf{x} \tag{4.31}$$

where $P_s(\mathbf{x})$ is the steady state probability configuration given by $P_s(\mathbf{x}) = \mathcal{N}\exp\left(-\frac{1}{2}\mathbf{x}^{\mathrm{T}}\boldsymbol{\Sigma}^{-1}\mathbf{x}\right)$, $\mathcal{N}$ being the normalization. Since $\mathbf{S} \neq 0$ is always true, we have in general $\mathbf{J}_s(\mathbf{x}) \neq 0$. This divergenceless steady state probability current can be expressed as a circulation, and thus opens up the possibility of having system-wide probability currents that keeps the SIRS in a state of *cyclic balance* [91] making quasicycles possible.

4.7 Non-normality increases variance

We have already noted that the violation of detailed balance is necessary for quasicycles. Here we further note that detailed balance violation has another consequence, that of enhancement of fluctuation amplitudes. With detailed balance the drift matrix $\mathbf{A}$ is similar to a symmetric matrix, and is therefore normal ($\mathbf{A}\mathbf{A}^T = \mathbf{A}^T\mathbf{A}$). In the absence of detailed balance, the drift matrix is no longer symmetric, and in this case is also non-normal.

As has been noted by Ioannou [92], the variance of a non-normal system driven by diagonal white noise is larger than its normal counterpart. Consider two stationary multivariate Ornstein-Uhlenbeck processes with drift and diffusion matrices $(\mathbf{A}_1, \mathbf{B})$ and $(\mathbf{A}_2, \mathbf{B})$ where $\mathbf{A}_1$ is non-normal but shares the same eigenvalues as the normal $\mathbf{A}_2$. Then, Schur decompositions of the two matrices gives $\mathbf{A}_1 = \mathbf{U}(\mathbf{D}+\mathbf{T})\mathbf{U}^\dagger$ and $\mathbf{A}_2 = \mathbf{U}\mathbf{D}\mathbf{U}^\dagger$ where $\mathbf{U}$ is unitary, $\mathbf{D}$ is diagonal matrix of eigenvalues and $\mathbf{T}$ is strictly upper triangular. Restricting the forcing to be diagonally correlated white noise ($\mathbf{B} = \mathbb{I}$), Ioannou shows that $\mathrm{Tr}(\boldsymbol{\Sigma}_1) \geq \mathrm{Tr}(\boldsymbol{\Sigma}_2)$, where $\boldsymbol{\Sigma}_1$ and $\boldsymbol{\Sigma}_2$ are the respective covariance matrices and $\mathrm{Tr}(\ldots)$ denotes the trace of a matrix. For a general $\mathbf{B}$ which is not necessarily diagonal, $\boldsymbol{\Sigma}_1 = \mathbf{A}_1^{-1}\left(\mathbf{S} - \frac{1}{2}\mathbf{B}\right)$ and

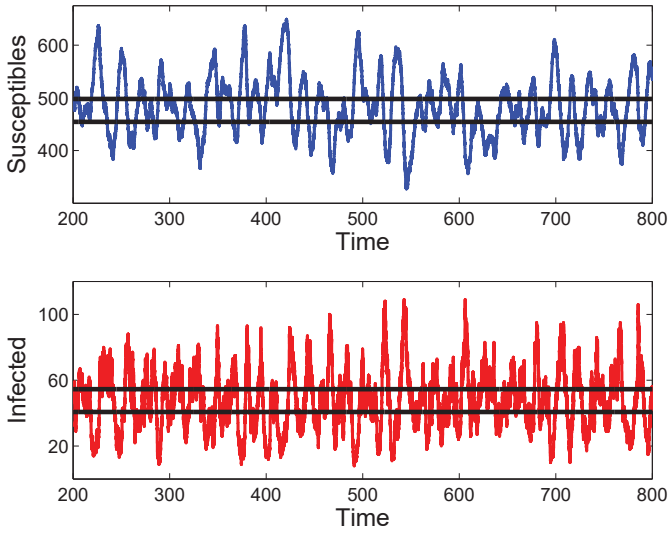

Figure 4.9: Enhanced variance of time-traces of susceptibles and infected for parameter values $\beta = 0.0021, \alpha = 0.1, \gamma = 1.0$ with population size $\Omega = 1000$. The solid black lines correspond to $\overline{n} \pm \sqrt{\overline{n}}$, where $\overline{n}$ is the mean.

$\mathbf{\Sigma}_2 = -\frac{1}{2}\mathbf{A}_2^{-1}\mathbf{B}$. We have calculated the ratio of the traces of $\mathbf{\Sigma}_1$ and $\mathbf{\Sigma}_2$.

$$\frac{\mathrm{Tr}(\mathbf{\Sigma}_1)}{\mathrm{Tr}(\mathbf{\Sigma}_2)} = 1 + \frac{\mathrm{Tr}\left(\mathbf{A}_1^{-1}\mathbf{S} + \frac{1}{2\Delta}\mathbf{U}\mathbf{T}\mathbf{U}^{\dagger}\mathbf{B}\right)}{\mathrm{Tr}\left(\mathbf{\Sigma}_2\right)} \tag{4.32}$$

where Δ is the determinant of $\mathbf{A}_1$. This expression is valid only when the spectrum of $\mathbf{A}_1$ is purely real. For the SIRS model, this ratio is greater than unity.

Individual time-traces also show an increase in variance. Figure (4.9) shows time-traces of S and I where the fluctuations are seen to be higher than the expected standard deviation values ($\overline{n} \pm \sqrt{\overline{n}}$, where $\overline{n}$ is the mean) marked by the black lines.

4.8 Conclusion

In this chapter, we have analyzed a closed endemic model for sustained, though asymptotically incoherent, oscillations in the population classes. These oscillations are generated

through fluctuations brought about by internal demographic stochasticity which destabilize the endemic fixed point. The closed nature of the problem allows one to deal with a simplified lower-dimensional problem, an aspect we have exploited systematically by showing how the master equation can be marginalized using the constraint. This model also lends itself to a two-stage linearization procedure, at the end of which it is reduced to a multivariate Ornstein-Uhlenbeck form. This results in the identification of the linearized drift matrix with the deterministic Jacobian matrix linearized about the endemic fixed point and permits the analysis of stochastic behaviour from the deterministic behaviour.

Noise-induced oscillations or quasicycles are possible only if the eigenvalues of the linearized Jacobian matrix are complex. These oscillations are distinct from those produced by external periodic agencies because their phases decorrelate asymptotically. Quasicycles can be reliably detected only if the oscillation time period is at least of the same order as the decorrelation time scale, as otherwise the decay dominates over the oscillation. Strong quasicycles are seen when the imaginary parts of the eigenvalues are larger than the real parts.

Stochastic coherence, or the non-trivial maximization of regularity of the oscillations at intermediate relative noise amplitudes (or equivalently at intermediate population sizes), is a striking aspect of the SIRS quasicycles. We have seen this both analytically from the relative strength of the peak of the power spectral density and numerically by directly computing the signal-to-noise ratio of the time-traces of each population class. This analysis requires a knowledge of the intrinsic noise in the system, namely the diffusion matrix **B**. However, we find that, for systems which can be reduced to a standard multivariate Ornstein-Uhlenbeck form by the two-stage linearization procedure mentioned earlier, it is possible to predict stochastic coherence purely from the deterministic analysis. Any non-trivial dependence on population size is contained only in the eigenvalues of the linearized drift matrix or equivalently the linearized Jacobian matrix, while the diffusion

matrix scales linearly with the population size. Thus, any non-monotonicities in fluctuations arise entirely from the deterministic part of the dynamics, i.e. the spectrum of the drift matrix. The noise merely excites these modes. This motivates the maximization of the ratio $|\mathrm{Im}(\lambda)/\mathrm{Re}(\lambda)|$ in the investigation of the population size value at which stochastic coherence is observed. Numerical results support this procedure. Therefore, we conclude that it is possible to make predictions about non-trivial behaviour of such systems in the stochastic regime by simply analyzing the linearized deterministic dynamics.

The violation of detailed balance is a necessary condition for the existence of quasicycles. Analysis of the drift, diffusion and $\mathbf{S}$ matrices indicates that the population system described by the SIRS model is always out of equilibrium and allows for quasicycles about the endemic fixed point for any choice of model parameters. The violation of detailed balance due to the non-normal nature of the system dynamics is manifest in the enhancement of fluctuation amplitudes of the populations. We have given an expression for the ratio of the trace of the non-normal covariance matrix over its normal counterpart, restricted to parameter values where the Jacobian spectrum is purely real. Numerics indicate that this ratio is greater than unity for the SIRS model.

Chapter 5

Irreducible representations of active matter flows

In this chapter, we present the most general representation of Stokes flow around a finite-sized spherical microswimmer as an expansion in irreducible Cartesian multipoles of the surface stress. The orthogonality and completeness of the tensorial multipoles results provides simple relations between the stresses and velocities that allows us to identify the multipoles necessary and sufficient for translation and rotation. Knowing the rigid body motion we are thus able to reconstruct, using only a few irreducible multipoles, the complex time-dependent flows observed in experiment. The power dissipation and swimming efficiency obtained in terms of these multipoles are in good agreement with experiment. We exploit the rotational invariance manifest in the Cartesian tensor expansion to derive a general constitutive equation for the stress tensor of an active micropolar continuum. In particular, our constitutive equation contains antisymmetric stresses not considered previously. Remarkably, however, these antisymmetric stresses separately conserve orbital and intrinsic angular momenta.

5.1 Chemomechanically active flows around swimming microorganisms

The collective dynamics of microscopic particles that swim in viscous fluids by converting chemical energy to mechanical work is a topic of current interest in non-equilibrium statistical mechanics [93, 24, 94, 95, 96, 97, 98, 99]. Biological and biomimetic examples of such "active" particles include, in increasing order of size, molecular motors [16], active nanobeads [18, 19, 21, 20] and swimming microorganisms. Momentum conservation and the lack of inertia at the microscopic scale implies that the fluid flow around such particles must be both force-free and torque-free, thus constraining it to decay no slower than the inverse square of the distance from the particle. Thus, at distances large compared to the particle size the dominant contribution to the flow is from the dipolar stresslet [100]. Continuum theories, applicable at scales much larger than the particle size, employ the stresslet flow to obtain the long-wavelength, long-time features of the collective dynamics of microswimmer suspensions [23, 25].

However, recent experiments, that resolve the flow around swimming microorganisms in unprecedented spatial and temporal detail, reveal near field features that cannot be captured by a purely stresslet description [101, 102, 103]. The complex flow around Chlamydomonas has easily identifiable qualitative features like stagnation points and strong lateral circulations that vary periodically with time. Both Chlamydomonas and Volvox rotate about their axis [102, 101] and thus must generate swirling flows while swimming. The flow around a generic translating and rotating microswimmer is then time-dependent with both axisymmetric and swirling components.

Lighthill and Blake provided an axisymmetric, time-dependent solution for Stokes flow around a spherical particle that, however, leaves out swirling components [104, 105]. Lamb's general solution accounts for these missing components but is formulated as an expansion in velocity point multipoles [106]. These multipoles do not directly provide a

simple representation of the flow around a finite-sized particle but must be combined in non-trivial ways to do so. Both Blake and Lamb present their solution in terms of spherical harmonics which do not transform as ordinary Cartesian tensors, further complicating their application to experimental flows. Motivated by these shortcomings, we carry out the following study.

5.2 Boundary integral representation of Stokes equation

Creeping flow around a particle obeys the Stokes equation,

$$\nabla \cdot \boldsymbol{\sigma} = -\nabla p + \eta \nabla^2 \mathbf{u} = 0 \tag{5.1a}$$

$$\nabla \cdot \mathbf{u} = 0 \tag{5.1b}$$

where $\mathbf{u}$ is the flow within the volume V, $\boldsymbol{\sigma}$ is the stress, p is the pressure and η is the viscosity. Chemomechanical activity can regulate either the velocity $\mathbf{u}^S$ or the stress $\boldsymbol{\sigma}^S$ on the surface S of the particle, which requires Dirichlet or Neumann boundary conditions, respectively. In either case, the flow in the bulk can be expressed as an integral over the boundary S, where a single layer density $\mathbf{q}(\mathbf{r})$ is convolved with the dyadic Green's function $\mathbf{G}(\mathbf{r}) = (\mathbb{I} + \hat{\mathbf{r}}\,\hat{\mathbf{r}})/|\mathbf{r}|^2$ [49, 48, 50],

$$\int_{S'} \mathbf{G}(\mathbf{r} - \mathbf{r}') \cdot \mathbf{q}(\mathbf{r}')\, \mathrm{d}S' = -8\pi\eta \begin{cases} \mathbf{u}(\mathbf{r}), & \mathbf{r} \in V \\ \mathbf{u}^S(\mathbf{r}), & \mathbf{r} \in S, \end{cases} \tag{5.2}$$

where $\mathbf{r}$ is the field point in the bulk V, $\mathbf{r}'$ is the source point on the surface S, and $\hat{\mathbf{r}}$ is the unit vector. Eq. (5.2), $\mathbf{r} \in V$, provides a complete solution for the Neumann problem with known single layer density. For the Dirichlet problem, Eq. (5.2), $\mathbf{r} \in S$, must be solved to obtain the unknown single layer density in terms of the prescribed boundary velocity $\mathbf{u}^S$.

5.3 Expansion of surface stress in irreducible Cartesian basis

If surface stresses $\boldsymbol{\sigma}^S$ are known, then the Neumann problem can be solved for spherical boundaries by expanding the single layer density in a spherical harmonic basis. A manifestly rotational covariant representation of such a basis is provided by irreducible Cartesian tensors $\overline{\hat{\mathbf{r}}^{(p)}}$, which obey the orthogonality condition

$$\left\langle \overline{\hat{\mathbf{r}}^{(p)}}\, \overline{\hat{\mathbf{r}}^{(q)}} \right\rangle = \frac{p!}{(2p+1)!!}\, \delta_{p,q}\, \boldsymbol{\Delta}^{(p,p)}. \tag{5.3}$$

The surface average $\langle \ldots \rangle = (1/4\pi a^2) \int \mathrm{d}S$, while the rank $2p$ tensor $\boldsymbol{\Delta}^{(p,p)}$ projects any p-th rank tensor $\widehat{\mathbf{r}}^{(p)}$ to its irreducible form $\overline{\hat{\mathbf{r}}^{(p)}}$ [107, 108]. Expanding $\mathbf{q}(\mathbf{r})$ in this basis, we get

$$\mathbf{q}(\mathbf{r}) = \sum_{p=0}^{\infty} \frac{(2p+1)!!}{4\pi a^2}\, \overline{\hat{\mathbf{r}}^{(p)}} \odot \mathbf{Q}^{(p+1)}, \quad \mathbf{r} \in S, \tag{5.4}$$

where the multipole moments $Q^{(p+1)}_{i\alpha_1 \ldots \alpha_p}$, symmetric and traceless in the last p indices, are given by

$$\mathbf{Q}^{(p+1)} = \frac{1}{p!} \int_S \mathbf{q}(\mathbf{r})\, \overline{\hat{\mathbf{r}}^{(p)}}\, \mathrm{d}S. \tag{5.5}$$

In Eq. (5.4), the symbol $\odot$ represents a p-fold contraction between a p-th rank tensor and another of higher rank, contracting the last index of the first tensor with the first index of the latter till p indices are contracted, such that $\overline{\hat{\mathbf{r}}^{(p)}} \odot \mathbf{Q}^{(p+1)} = \overline{\widehat{r}_{\alpha_1 \alpha_2 \ldots \alpha_{p-1} \alpha_p}}\, Q^{(p+1)}_{\alpha_p \alpha_{p-1} \ldots \alpha_2 \alpha_1 i}$. We now insert Eq. (5.4) into Eq. (5.2), $\mathbf{r} \in V$, and obtain

$$8\pi\eta\, \mathbf{u}(\mathbf{r}) = -\sum_{p=0}^{\infty} \frac{(2p+1)!!}{4\pi a^2} \int_{S'} \mathbf{G}(\mathbf{r}-\mathbf{r}') \cdot \mathbf{Q}^{(p+1)} \odot \overline{\hat{\mathbf{r}}^{(p)}}\, \mathrm{d}S' \tag{5.6}$$

Writing this in terms of the Fourier transform of the Green's function, $\mathbf{G}(\mathbf{k}) = 8\pi(\mathbb{I} - \hat{\mathbf{k}}\,\hat{\mathbf{k}})/|\mathbf{k}|^2$, we get

$$8\pi\eta\,\mathbf{u}(\mathbf{r}) = -\sum_{p=0}^{\infty} \frac{(2p+1)!!}{4\pi a^2} \int_k \frac{\mathrm{d}^3k}{(2\pi)^3}\, e^{i\mathbf{k}\cdot\mathbf{r}}\, \mathbf{G}(\mathbf{k}) \cdot \mathbf{Q}^{(p+1)} \odot \int_{S'} \mathrm{d}S'\, e^{-i\mathbf{k}\cdot\mathbf{r}'}\, \overline{\hat{\mathbf{r}}^{(p)}} \tag{5.7}$$

We expand the plane wave in spherical Bessel functions,

$$e^{i\mathbf{k}\cdot\mathbf{r}} = \sum_{m=0}^{\infty} \frac{(i)^m(2m+1)!!}{m!}\, j_m(kr)\, \overline{\hat{\mathbf{k}}^{(m)}} \odot \overline{\hat{\mathbf{r}}^{(m)}}, \tag{5.8}$$

and thus obtain

$$\begin{aligned} 8\pi\eta\,\mathbf{u}(\mathbf{r}) &= -\sum_{p=0}^{\infty}\sum_{m=0}^{\infty} \frac{(-i)^m(2p+1)!!(2m+1)!!}{m!} \\ &\quad \times \int \frac{\mathrm{d}^3k}{(2\pi)^3}\, e^{i\mathbf{k}\cdot\mathbf{r}}\, j_m(ka)\, \mathbf{G}(\mathbf{k}) \cdot \mathbf{Q}^{(p+1)} \odot \left\langle \overline{\hat{\mathbf{r}}^{(p)}}\, \overline{\hat{\mathbf{r}}^{(m)}} \right\rangle \odot \overline{\hat{\mathbf{k}}^{(m)}} \\ &= -\sum_{p=0}^{\infty} (-i)^p(2p+1)!! \int \frac{\mathrm{d}^3k}{(2\pi)^3}\, e^{i\mathbf{k}\cdot\mathbf{r}}\, j_p(ka)\, \mathbf{G}(\mathbf{k}) \cdot \mathbf{Q}^{(p+1)} \odot \hat{\mathbf{k}}^{(p)}. \end{aligned} \tag{5.9}$$

Here $\mathbf{\Delta}^{(p,p)} \odot \overline{\hat{\mathbf{k}}^{(p)}} = \overline{\hat{\mathbf{k}}^{(p)}}$, and $\mathbf{Q}^{(p+1)} \odot \overline{\hat{\mathbf{k}}^{(p)}} \equiv \mathbf{Q}^{(p+1)} \odot \hat{\mathbf{k}}^{(p)}$ since $\mathbf{Q}^{(p+1)}$ is already symmetrized and detraced in its trailing $p-1$ indices. The spherical Bessel function can be expanded in polynomials of the wavenumber k and truncated,

$$j_p(ka) = \frac{a^p k^p}{(2p+1)!!}\left[1 - \frac{a^2k^2}{4p+6} + O(k^4)\right] = \frac{a^p k^p}{(2p+1)!!}\left(1 - \frac{a^2k^2}{4p+6}\right) \tag{5.10}$$

since $k^4\mathbf{G}(\mathbf{k}) = 0$ from biharmonicity. Substituting this in Eq. (5.9),

$$8\pi\eta\,\mathbf{u}(\mathbf{r}) = -\sum_{p=0}^{\infty} a^p\, \mathbf{Q}^{(p+1)} \odot \int \frac{\mathrm{d}^3k}{(2\pi)^3}\, e^{i\mathbf{k}\cdot\mathbf{r}}\, (-i\mathbf{k})^{(p)} \cdot \left(1 - \frac{a^2k^2}{4p+6}\right)\mathbf{G}(\mathbf{k}), \tag{5.11}$$

and taking the inverse transform we get the required flow equation

$$8\pi\eta\,\mathbf{u}(\mathbf{r}) = -\sum_{p=0}^{\infty} a^p\, \mathbf{Q}^{(p+1)} \odot (-\boldsymbol{\nabla})^{(p)} \cdot \left(1 + \frac{a^2}{4p+6}\nabla^2\right)\mathbf{G}(\mathbf{r}) \tag{5.12}$$

The flow at any order p, $\mathbf{u}_p$, has contributions which decay as r^{-p} and $r^{-(p+2)}$. Thus the stress multipole expansion automatically generates the Faxén corrections $a^2\nabla^2\mathbf{G}(\mathbf{r})/(4p+6)$ that must be manually reconstructed when expanding in the velocity multipoles of Lamb's general solution [106].

5.4 Fundamental irreducible components of active Stokes flow

The general solution in Eq. (5.12) can be simplified by decomposing the reducible single layer moments into irreducible tensors. Any p-th rank tensor $\mathbf{Q}^{(p)}$ can be decomposed into irreducible tensors $\mathbf{Q}^{(p)}_{j,r}$, of weight $j \leq p$ with $2j+1$ independent components, subtending a j dimensional irreducible representation of the rotation group $SO(3)$ [109, 110, 111]. The seniority index r is needed when more than one weight j representation occurs in the decomposition. The general decomposition is then the direct sum $\mathbf{Q}^{(p)} = \oplus_{j,r}\mathbf{Q}^{(p)}_{j,r}$ [109, 110, 111]. The tensors corresponding to weights 1, 2 and 3 are known as vectors, deviators, and septors respectively and can be further classified by their parity as polar (true) or axial (psuedo) tensors. The constraints imposed by incompressibility, biharmonicity and spherical symmetry imply that only the first three irreducible parts contribute. Here we focus on the minimal set of multipoles required to produce active translations and rotations. This requires us to enumerate all rank 3 irreducible multipoles $p \leq 2$ and the rank 4 pseudoseptorial multipole for $p = 3$, which, as we shall soon see, is responsible for particle rotations. The other two rank 4 irreducible multipoles, the deviator and the nonor, do not contribute any new locomotory mode and is thus not considered in this treatment.

The decompositions we require are, [109, 110, 111, 112]

$$Q^{(1)}_i = F_i, \tag{5.13a}$$

$$Q^{(2)}_{i\alpha} = \frac{1}{a}\left[S_{i\alpha} - \frac{1}{2}\epsilon_{i\alpha\nu}T_\nu\right], \tag{5.13b}$$

$$Q^{(3)}_{i\alpha\beta} = \frac{1}{a^2}\left[\Gamma_{i\alpha\beta} + \frac{2}{3}\left(\epsilon_{i\alpha\nu}\Psi_{\nu\beta} + \epsilon_{i\beta\nu}\Psi_{\nu\alpha}\right) + \frac{1}{10}\left(-2d_i\delta_{\alpha\beta} + 3d_\alpha\delta_{\beta i} + 3d_\beta\delta_{i\alpha}\right)\right] \tag{5.13c}$$

$$Q^{(4;3)}_{i\,\alpha\beta\gamma} = -\frac{1}{4a^3}\left(\epsilon_{i\alpha\nu}\Lambda_{\nu\beta\gamma} + \epsilon_{i\beta\nu}\Lambda_{\nu\gamma\alpha} + \epsilon_{i\gamma\nu}\Lambda_{\nu\beta\alpha}\right). \tag{5.13d}$$

where $\boldsymbol{\epsilon}$ is the rank-3 antisymmetric Levi-Civita tensor. Here $Q^{(4;3)}$ represents the rank 4, weight 3 tensor. The force $\mathbf{F}$, the torque $\mathbf{T}$, stresslet $\mathbf{S}$ and the potential dipole $\mathbf{d}$ are familiar irreducible multipoles. The new irreducible multipoles introduced here are the second rank pseudodeviatoric torque dipole $\boldsymbol{\Psi}$ or the "vortlet", the third rank septorial stresslet dipole $\boldsymbol{\Gamma}$ or the "septlet", and the third rank pseudoseptorial multipole $\boldsymbol{\Lambda}$ or the "spinlet". Using these decompositions and Eq. (5.12), force-free torque-free flows decaying no faster than r^{-5} are expressed as

$$\begin{aligned} 8\pi\eta\,\mathbf{u}^{\mathrm{a}}(\mathbf{r}) = &\left(1 + \frac{a^2}{10}\nabla^2\right)\boldsymbol{\nabla}\mathbf{G}\odot\mathbf{S} + \frac{1}{5}\nabla^2\mathbf{G}\cdot\mathbf{d} + \frac{4}{3}\left(\boldsymbol{\Psi}\cdot\boldsymbol{\nabla}\right)\cdot\left(\boldsymbol{\nabla}\times\mathbf{G}\right) \\ &- \left(1 + \frac{a^2}{14}\nabla^2\right)\boldsymbol{\nabla}\boldsymbol{\nabla}\mathbf{G}\odot\boldsymbol{\Gamma} - \frac{3}{4}\left(\boldsymbol{\Lambda} : \boldsymbol{\nabla}\boldsymbol{\nabla}\right)\cdot\left(\boldsymbol{\nabla}\times\mathbf{G}\right). \end{aligned} \tag{5.14}$$

There are a total of 27 independent coefficients, with individual multipoles contributing $5, 3, 5, 7$ and 7 independent coefficients respectively. The stresslet $\mathbf{S}$ completely characterizes active flows decaying as r^{-2}. The potential dipole $\mathbf{d}$, the vortlet $\boldsymbol{\Psi}$ and the septlet $\boldsymbol{\Gamma}$ together completely characterize flows decaying as r^{-3}. The spinlet $\boldsymbol{\Lambda}$ produces a flow decaying as r^{-4}. The vortlet and the spinlet produce swirling flows which have not been considered before.

Substituting $\mathbf{G}(\mathbf{r}) = (\mathbb{I} + \hat{\mathbf{r}}\,\hat{\mathbf{r}})/|\mathbf{r}|^2$ into Eq. (5.14), we get

$$\begin{aligned} 8\pi\eta\,\mathbf{u}^{\mathrm{a}}(\mathbf{r}) = &-\frac{6}{5r^2}\left(\frac{a^2}{r^2}\right)\Big(\mathbf{S}\cdot\hat{\mathbf{r}}\Big) - \frac{3}{r^2}\left(1-\frac{a^2}{r^2}\right)\Big(\mathbf{S}:\hat{\mathbf{r}}\,\hat{\mathbf{r}}\Big)\hat{\mathbf{r}} + \frac{2}{5r^3}\Big[\,\mathbf{d} - 3(\mathbf{d}\cdot\hat{\mathbf{r}})\,\hat{\mathbf{r}}\,\Big] \\ &- \frac{8}{3r^3}\,(\hat{\mathbf{r}}\times\boldsymbol{\Psi}\cdot\hat{\mathbf{r}}) + \frac{3}{r^3}\left(1-\frac{15a^2}{7r^2}\right)\Big(\boldsymbol{\Gamma}\odot\hat{\mathbf{r}}\hat{\mathbf{r}}\Big) - \frac{15}{r^3}\left(1-\frac{a^2}{r^2}\right)\Big(\boldsymbol{\Gamma}\odot\hat{\mathbf{r}}\,\hat{\mathbf{r}}\,\hat{\mathbf{r}}\Big)\hat{\mathbf{r}} \\ &- \frac{6}{r^4}\Big(\hat{\mathbf{r}}\times\boldsymbol{\Lambda}:\hat{\mathbf{r}}\,\hat{\mathbf{r}}\Big) \end{aligned} \tag{5.15}$$

It is straightforward to calculate the vorticity $\boldsymbol{\omega} = \boldsymbol{\nabla}\times\mathbf{u}^{\mathrm{a}}$ of the flow using Eq. (5.15). All the fundamental multipoles contribute towards the vorticity except for $\mathbf{d}$ which, by definition, produces potential or irrotational flows. Noting that the Stokes equation guarantees $\boldsymbol{\nabla}\times\nabla^2\mathbf{G} = 0$, we get

$$\begin{aligned} 8\pi\eta\,\boldsymbol{\omega}(\mathbf{r}) = &\frac{2}{r^3}\Big(\hat{\mathbf{r}}\times\mathbf{S}\cdot\hat{\mathbf{r}}\Big) + \frac{8}{3r^4}\Big[6\,\boldsymbol{\Psi}\cdot\hat{\mathbf{r}} - 5\Big(\boldsymbol{\Psi}:\hat{\mathbf{r}}\hat{\mathbf{r}}\Big)\hat{\mathbf{r}}\Big] \\ &+ \frac{30}{r^4}\Big(\hat{\mathbf{r}}\times\boldsymbol{\Gamma}\odot\hat{\mathbf{r}}\,\hat{\mathbf{r}}\Big) + \frac{6}{r^4}\Big[7\Big(\boldsymbol{\Lambda}\odot\hat{\mathbf{r}}\hat{\mathbf{r}}\hat{\mathbf{r}}\Big)\hat{\mathbf{r}} - 3\boldsymbol{\Lambda}\odot\hat{\mathbf{r}}\hat{\mathbf{r}}\Big] \end{aligned} \tag{5.16}$$

Comparing the fundamental components of the flow with the vorticity, we find a curious exchange of tensorial structure between $\mathbf{S}$ and $\boldsymbol{\Psi}$, and also between $\boldsymbol{\Gamma}$ and $\boldsymbol{\Lambda}$.

5.5 Visualization of uniaxially parametrized multipolar flows

Uniaxial parametrizations are the simplest representations of the stress multipoles and help visualize the irreducible flows. If $\hat{\mathbf{p}}$ determines the parametrization direction, then

the uniaxial parametrizations that preserve symmetry and tracelessness conditions are

$$\mathbf{S} = S_0\left(\hat{\mathbf{p}}\hat{\mathbf{p}} - \frac{1}{3}\mathbb{I}\right) \tag{5.17a}$$

$$\mathbf{d} = d_0\hat{\mathbf{p}} \tag{5.17b}$$

$$\mathbf{\Psi} = \Psi_0\left(\hat{\mathbf{p}}\hat{\mathbf{p}} - \frac{1}{3}\mathbb{I}\right) \tag{5.17c}$$

$$\mathbf{\Gamma} = \Gamma_0\left(\hat{\mathbf{p}}\hat{\mathbf{p}}\hat{\mathbf{p}} - \frac{3}{5}\overbrace{\hat{\mathbf{p}}\mathbb{I}}\right) \tag{5.17d}$$

$$\mathbf{\Lambda} = \Lambda_0\left(\hat{\mathbf{p}}\hat{\mathbf{p}}\hat{\mathbf{p}} - \frac{3}{5}\overbrace{\hat{\mathbf{p}}\mathbb{I}}\right) \tag{5.17e}$$

where $\overbrace{\ldots}$ denotes complete symmetrization. The stresslet strength S_0 and the septlet strength Γ_0 are true scalars, while the vortlet strength Ψ_0 and the spinlet strength Λ_0 are pseudoscalars. Substituting these in Eq. (5.14), we obtain uniaxial flows. Stresslet, potential dipole and septlet flows are shown in Fig. (5.1), while swirling flows due to the vortlet and the spinlet are shown in Fig. (5.2).

5.6 Relation between surface stress and velocity multipoles

If the velocities on the boundaries are known, then the resulting Dirichlet problem, Eq. (5.2), $\mathbf{r} \in S$, is solved by expanding the prescribed the surface velocity $\mathbf{u}^S(\mathbf{r})$ in the same irreducible basis $\overline{\hat{\mathbf{r}}^{(p)}}$,

$$\mathbf{u}^S(\mathbf{r}) = \sum_{p=0}^{\infty} \frac{1}{p!}\,\overline{\hat{\mathbf{r}}^{(p)}} \odot \mathbf{V}^{(p+1)} \tag{5.18}$$

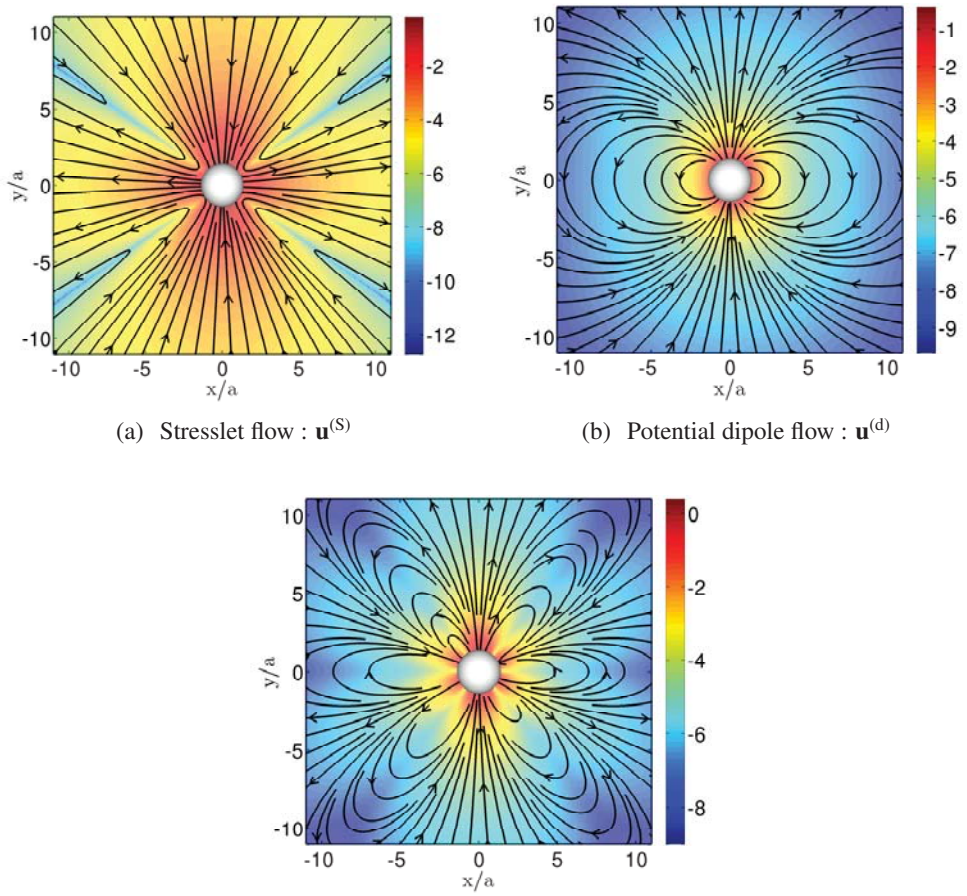

(a) Stresslet flow : $\mathbf{u}^{(S)}$

(b) Potential dipole flow : $\mathbf{u}^{(d)}$

(c) Septlet flow : $\mathbf{u}^{(\Gamma)}$

Figure 5.1: Cross-sections of long-range hydrodynamic flows around an active particle of radius a generated by irreducible moments of the single layer density, Eq. (11) of main text. Streamlines show the direction of the flow while the background color represents the natural logarithm of the strength of the flow. The contractile stresslet $\mathbf{S}$, uniaxially parametrized in $\widehat{\mathbf{e}}_{\mathbf{y}}$, generates "puller" flows that neither translate nor rotate the particle, panel (a), and decay as r^{-2}. The flows due to the potential dipole $\mathbf{d}$, panel (b), and the uniaxially parametrized septlet $\mathbf{\Gamma}$, panel (c), generate a net translational effect on the particle along the parametrization direction $\widehat{\mathbf{e}}_{\mathbf{y}}$. These decay as r^{-3}.

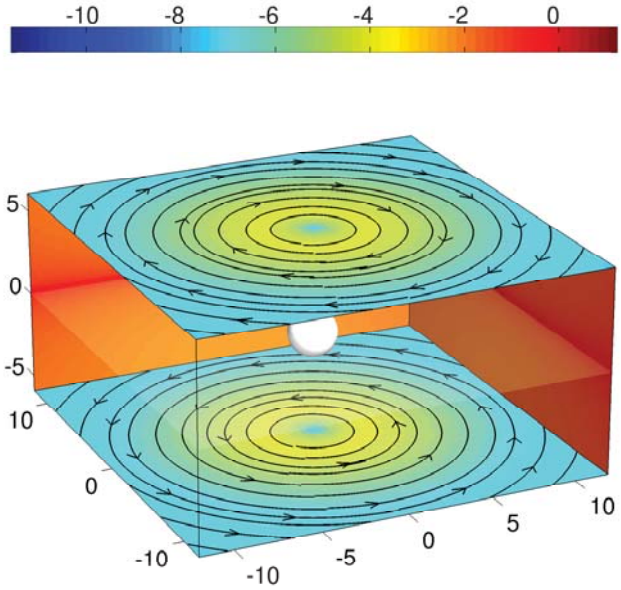

(a) Vortlet flow : $\mathbf{u}^{(\Psi)}$

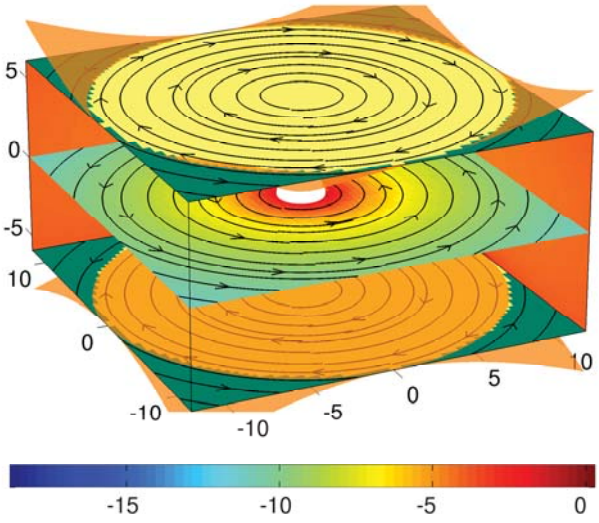

(b) Spinlet flow : $\mathbf{u}^{(\Lambda)}$

Figure 5.2: Swirling flows around an active particle of radius a generated by (a) a vortlet $\mathbf{\Psi}$ and (b) a spinlet $\mathbf{\Lambda}$, Eq. (5.14), both uniaxially parametrized. Streamlines show the direction of the flow while the background color represents the natural logarithm of the strength of the flow. The vortlet is a dipole of rotlets and thus produces r^{-3} flows that rotate in opposite directions above and below the equatorial plane. Since the net flow over the surface of the sphere is zero, this multipole does not contribute to particle self-rotation. The spinlet produces r^{-4} flows that rotate in the same direction at the particle surface but switch directions across the isosurface $\cos^2\theta - 1/5$, where θ is the polar angle. We predict that this multipole is responsible for self-rotations in active particles, as well as swirling flows around Volvox.

where the multipole moments $V^{(p+1)}_{i\alpha_1\ldots\alpha_p}$, symmetric and traceless in the last p indices, are given by

$$\mathbf{V}^{(p+1)} = (2p+1)!!\langle \mathbf{u}^{\mathrm{S}}\, \overline{\hat{\mathbf{r}}^{(p)}}\, \rangle. \tag{5.19}$$

Equating Eq. (5.18) and Eq. (5.9) on S, and expanding the plane wave in spherical Bessel functions once again, we get

$$\begin{aligned} 8\pi\eta \sum_{m=0}^{\infty} \frac{1}{m!}\, \overline{\hat{\mathbf{r}}^{(m)}} \odot \mathbf{V}^{(m+1)} = &- \sum_{p=0}^{\infty}\sum_{n=0}^{\infty} \frac{1}{n!} i^{n-p}(2p+1)!!(2n+1)!! \\ &\times \int \frac{d^3k}{(2\pi)^3} j_n(ka) j_p(ka)\, \overline{\hat{\mathbf{k}}^{(n)}} \odot \overline{\hat{\mathbf{r}}^{(n)}}\, \mathbf{G}(\mathbf{k}) \cdot \hat{\mathbf{k}}^{(p)} \odot \mathbf{Q}^{(p+1)} \end{aligned} \tag{5.20}$$

Using the spherical Bessel function identity

$$\int_0^{\infty} \frac{dk}{2\pi} j_n(ka) j_p(ka) = \frac{1}{4a(2n+1)} \delta_{n,p} \tag{5.21}$$

and orthogonality, Eq. (5.3), we get

$$8\pi\eta \frac{1}{(2p+1)!!} \mathbf{V}^{(p+1)} = -\frac{(2p-1)!!}{4\pi a} \int \frac{k^2 \mathrm{d}\Omega_k}{4\pi}\, \hat{\mathbf{k}}^{(p)}\, \mathbf{G}(\mathbf{k}) \cdot \hat{\mathbf{k}}^{(p)} \odot\, \mathbf{Q}^{(p+1)} \tag{5.22}$$

Since $k^2\mathbf{G}(\mathbf{k}) = 8\pi(\mathbb{I} - \hat{\mathbf{k}}\hat{\mathbf{k}})$, we finally get the desired relation

$$\mathbf{V}^{(p+1)} = \boldsymbol{\mathcal{G}}^{(p+1,\,p+1)} \odot \mathbf{Q}^{(p+1)} \tag{5.23}$$

where the $2(p+1)$ rank tensor $\boldsymbol{\mathcal{G}}$ is given by [113]

$$\boldsymbol{\mathcal{G}}^{(p+1,\,p+1)} = -\frac{(2p-1)!!(2p+1)!!}{(4\pi\eta a)} \int \frac{d\Omega}{4\pi}\, \overline{\hat{\mathbf{r}}^{(p)}}\, (\mathbb{I} - \hat{\mathbf{r}}\hat{\mathbf{r}})\, \overline{\hat{\mathbf{r}}^{(p)}} \tag{5.24}$$

We now expand both sides of Eq. (5.23) in irreducible multipoles and obtain relations between irreducible velocity and stress multipoles.

5.7 Irreducible description of active particle motion

Active translations $\mathbf{V}$ and rotations $\boldsymbol{\Omega}$ of the *particle* can be obtained from the linear relation between the velocity and stress multipoles at the boundary, where $\mathbf{u}^S(\mathbf{r}) = \mathbf{V} + a\boldsymbol{\Omega}\times\widehat{\mathbf{r}} + \mathbf{v}^a(\mathbf{r})$ and $\mathbf{v}^a$ is an activity induced surface velocity. We get, from Eq. (5.23),

$$\mathbf{F} = -6\pi\eta a\left(\mathbf{V} + \langle \mathbf{v}^{\mathrm{a}}\rangle\right) \tag{5.25a}$$

$$\mathbf{T} = -8\pi\eta a^2\left(a\boldsymbol{\Omega} - \frac{3}{2}\left\langle \mathbf{v}^{\mathrm{a}}\times\widehat{\mathbf{r}}\right\rangle\right) \tag{5.25b}$$

$$\mathbf{S} = -10\pi\eta a^2\left\langle \mathbf{v}^{\mathrm{a}}\widehat{\mathbf{r}} + (\mathbf{v}^{\mathrm{a}}\widehat{\mathbf{r}})^{\mathrm{T}}\right\rangle \tag{5.25c}$$

$$\mathbf{d} = -30\pi\eta a^3\left\langle (\mathbf{v}^{\mathrm{a}}\cdot\widehat{\mathbf{r}})\widehat{\mathbf{r}} - \frac{1}{3}\mathbf{v}^{\mathrm{a}}\right\rangle \tag{5.25d}$$

$$\boldsymbol{\Psi} = 5\pi\eta a^3\left\langle (\mathbf{v}^{\mathrm{a}}\times\widehat{\mathbf{r}})\widehat{\mathbf{r}} + \{(\mathbf{v}^{\mathrm{a}}\times\widehat{\mathbf{r}})\widehat{\mathbf{r}}\}^{\mathrm{T}}\right\rangle \tag{5.25e}$$

$$\boldsymbol{\Gamma} = -\frac{35}{2}\pi\eta a^3\left\langle \overbrace{\mathbf{v}^{\mathrm{a}}\widehat{\mathbf{r}}\widehat{\mathbf{r}}} - \frac{2}{5}(\mathbf{v}^{\mathrm{a}}\cdot\widehat{\mathbf{r}})\,\overbrace{\widehat{\mathbf{r}}\mathbb{I}} - \frac{1}{5}\,\overbrace{\mathbf{v}^{\mathrm{a}}\mathbb{I}}\right\rangle \tag{5.25f}$$

$$\boldsymbol{\Lambda} = 14\pi\eta a^4\left\langle \overbrace{(\mathbf{v}^{\mathrm{a}}\times\widehat{\mathbf{r}})\widehat{\mathbf{r}}\widehat{\mathbf{r}}} - \frac{3}{5}\,\overbrace{(\mathbf{v}^{\mathrm{a}}\times\widehat{\mathbf{r}})\mathbb{I}}\right\rangle. \tag{5.25g}$$

The first two relations above show that a force-free torque-free particle acquires translation and rotational motion only if the surface averages of the $\mathbf{v}^{\mathrm{a}}$ and $\mathbf{v}^{\mathrm{a}}\times\hat{\mathbf{r}}$ are non-zero [114, 115, 116], that is,

$$\mathbf{V} = -\langle \mathbf{v}^{\mathrm{a}}\rangle \tag{5.26a}$$

$$\boldsymbol{\Omega} = -\frac{3}{2a}\left\langle \widehat{\mathbf{n}}\times\mathbf{v}^{\mathrm{a}}\right\rangle \tag{5.26b}$$

The remaining relations appear to be new. The utility of these relations is that, given the active $\mathbf{V}$ and $\boldsymbol{\Omega}$, they determine the minimal external flow $\mathbf{u}^{\mathrm{a}}(\mathbf{r})$. This $\mathbf{u}^{\mathrm{a}}(\mathbf{r})$ is the sum of a potential dipole of strength $\mathbf{d} = -30\pi\eta a^3\left[\langle(\mathbf{v}^{\mathrm{a}}\cdot\widehat{\mathbf{r}})\widehat{\mathbf{r}}\rangle + \frac{1}{3}\mathbf{V}\right]$ and a spinlet of strength $\boldsymbol{\Lambda} = 14\pi\eta a^4[\langle\overbrace{(\mathbf{v}^{\mathrm{a}}\times\widehat{\mathbf{r}})\widehat{\mathbf{r}}\widehat{\mathbf{r}}}\rangle - \frac{2a}{5}\,\overbrace{\boldsymbol{\Omega}\mathbb{I}}\,]$ The stresslet $\mathbf{S}$, the septlet $\boldsymbol{\Gamma}$ and the vortlet $\boldsymbol{\Psi}$ modify the external flow without affecting $\mathbf{V}$ and $\boldsymbol{\Omega}$. However, they contribute to long range flows and, thus, influence interparticle hydrodynamic interactions. Eqns. (5.25) provide a manifestly rotational invariant relationship between the external flow and the

rigid body motion, $\mathbf{V}$ and $\mathbf{\Omega}$, and active surface velocity $\mathbf{v}^{\mathrm{a}}$ of the particle. Previous work only considered the relationship between rigid body motion and surface velocity confined to purely axisymmetric flows, thus missing the crucial active swirling flow components considered here.

5.8 Power dissipated into the fluid

The power dissipated into the fluid is given by

$$\dot{W} = -\int \mathbf{q} \cdot \mathbf{u}^S \, \mathrm{d}S. \tag{5.27}$$

Inserting the boundary integral equation for the velocity into the above gives

$$8\pi\eta \, \dot{W} = \int \mathbf{q}(\mathbf{x}) \cdot \mathbf{G}(\mathbf{x} - \mathbf{x}') \cdot \mathbf{q}(\mathbf{x}') \, \mathrm{d}S \, \mathrm{d}S'. \tag{5.28}$$

Expanding the single layer density in irreducible tensors, we finally get after some algebra,

$$\dot{W} = -\frac{1}{4\pi\eta a} \sum_{p=0}^{\infty} (2p-1)!!(2p+1)!! \; \mathbf{Q}^{(p+1)} \odot \left\{ \int \frac{\mathrm{d}\Omega_k}{4\pi} \; \overline{\widehat{\mathbf{k}}^{(p)}} \left(\mathbb{I} - \hat{\mathbf{k}}\hat{\mathbf{k}} \right) \overline{\widehat{\mathbf{k}}^{(p)}} \right\} \odot \mathbf{Q}^{(p+1)}. \tag{5.29}$$

This can be immediately recast in a more succinct form,

$$\dot{W} = \sum_{p=0}^{\infty} \mathbf{Q}^{(p+1)} \odot \boldsymbol{\mathcal{G}}^{(p+1,\,p+1)} \odot \mathbf{Q}^{(p+1)} \tag{5.30}$$

Resolving into relevant irreducible multipoles, we get

$$\dot{W} = -\frac{3}{20\pi\eta a^3}\mathbf{S}\odot\mathbf{S} - \frac{3}{10\pi\eta a^5}\mathbf{d}\odot\mathbf{d} - \frac{32}{3\pi\eta a^5}\mathbf{\Psi}\odot\mathbf{\Psi} - \frac{6}{7\pi\eta a^5}\mathbf{\Gamma}\odot\mathbf{\Gamma} - \frac{675}{16\pi\eta a^7}\mathbf{\Lambda}\odot\mathbf{\Lambda}. \tag{5.31}$$

In the next two sections, we use Eqs. (5.14), (5.25) and (5.31) to analyze the time-dependent oscillatory motion of Chlamydomonas that produces long range approximately axisymmetric flow and the rotational motion of Volvox that produces a short range swirling flow.

5.9 Oscillatory flows around Chlamydomonas

The flow around the microorganism Chlamydomonas has recently been measured in detail to reveal a flow field that is "complex and highly time-dependent" [102]. We are able to capture the essential features of this flow by superposing flows due to the potential dipole, stresslet, and septlet with time-varying strengths. Assuming particle motion to occur along the y-axis the multipoles are parametrized uniaxially as $\mathbf{S} = S_0(t)(\widehat{\mathbf{yy}} - \frac{1}{3}\mathbb{I})$, $\mathbf{d} = d_0(t)\widehat{\mathbf{y}}$ and $\mathbf{\Gamma} = \Gamma_0(t)(\widehat{\mathbf{yyy}} - \frac{3}{5}\overbrace{\widehat{\mathbf{y}}\mathbb{I}}^{})$. The data of [102] shows that the translation speed can be very well parametrized by the first two Fourier modes,

$$V(t) = \frac{a_0}{2}\left[1 + \frac{2a_1}{a_0}\cos(\omega t) + \frac{2a_2}{a_0}\cos(2\omega t) + \frac{2b_1}{a_0}\sin(\omega t) + \frac{2b_2}{a_0}\sin(2\omega t)\right] \tag{5.32}$$

where the values are given by $a_0 = 247.7\mu m s^{-1}$, $a_1 = -86.81$, $a_2 = -31.9$, $b_1 = 305.6$ and $b_2 = -21.1$, all in units of $\mu m s^{-1}$. We show the values and the corresponding fit in Fig. (5.4).

Using Eqs. (5.26a) and (5.25d), we extract the strength of the potential dipole using the minimal representation, $d_0(t) = -10\pi\eta a^3\langle v^a(t)\rangle$. We estimate the stresslet and the septlet

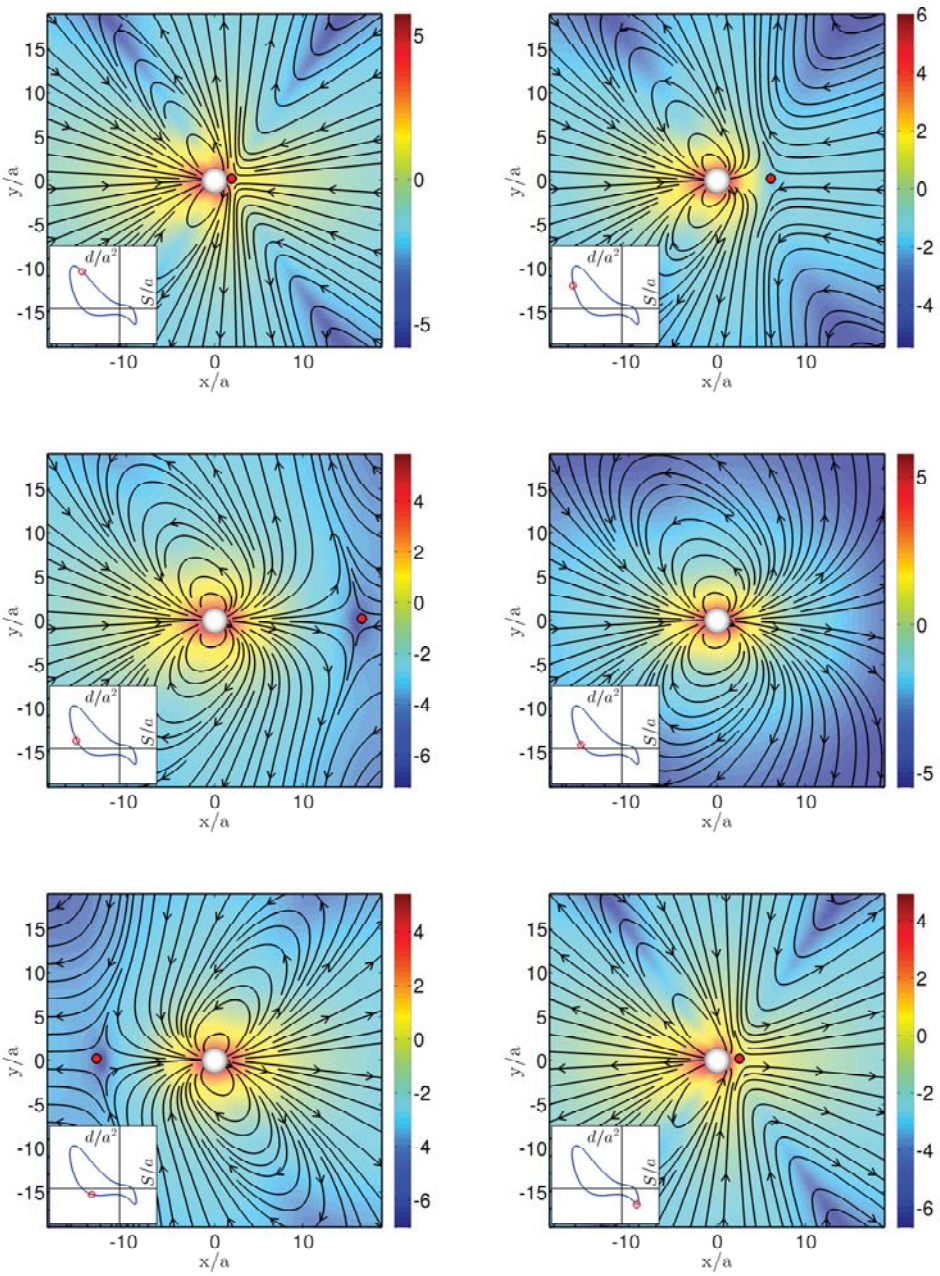

Figure 5.3: Cross-sections of long-range hydrodynamic flows around a spherical active particle of radius a generated by a linear combination of time-dependent stresslet $\mathbf{S}$, potential dipole $\mathbf{d}$ and septlet $\mathbf{\Gamma}$. Streamlines show the direction of the flow while the background color represents the natural logarithm of the strength of the flow. The mutual variation $\mathbf{S}/a$ and $\mathbf{d}/a^2$ is shown in the inset. The red dot indicates the approximate position of the stagnation point. These flow fields are in good agreement with experimentally measured flow fields around a swimming Chlamydomonas [102]. The inset shows the variation of the potential dipole and the stresslet; the blue line shows the overall variation, while the red circle shows the values for that frame.

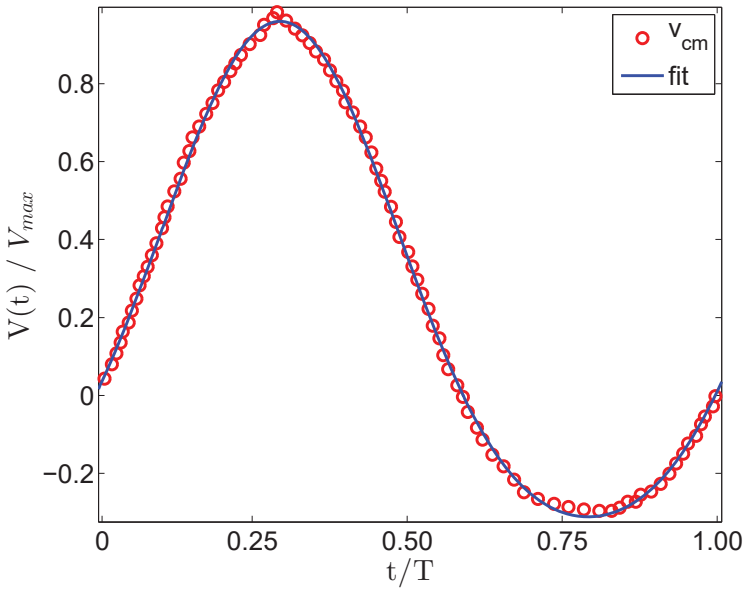

Figure 5.4: Estimation of the centre of mass velocity of Chlamydomonas reinhardtii from flow speeds measured using particle image velocimetry [102]. Red circles are data values, while the blue line is the Fourier fit, Eq. (5.32), with coefficients as given in the text.

strengths from the position of the stagnation point, and then obtain the total flow from a linear combination of $\mathbf{u}^{(S)}$, $\mathbf{u}^{(d)}$ and $\mathbf{u}^{(\Gamma)}$. The result, shown in the video and Fig. (5.3) effectively captures essential features of the flow around a swimming Chlamydomonas [102]. Using Eq. (5.31), we write the power dissipated by the Chlamydomonas as

$$\dot{W}^{\mathrm{Ch}}(t) = \frac{3}{20\pi\eta a^3}\mathbf{S}\odot\mathbf{S} + \frac{3}{10\pi\eta a^5}\mathbf{d}\odot\mathbf{d} + \frac{6}{7\pi\eta a^5}\mathbf{\Gamma}\odot\mathbf{\Gamma} \tag{5.33}$$

The instantaneous efficiency of translation, defined as ratio of power expended by an external force to maintain a rigid sphere in uniform motion with speed V to that expended chemomechanically to maintain the same speed [104], is computed to be

$$\epsilon^{\mathrm{Ch}}(t) = \frac{6\pi\eta a V^2}{\dot{W}^{\mathrm{Ch}}(t)} \tag{5.34}$$

Since $\mathbf{d}\odot\mathbf{d} = 100\pi^2\eta^2 a^6 V^2$ for purely tangential surface flows, the maximum translational efficiency of a Chlamydomonas is 20%.

The time variation of $d_0(t)$ and $S_0(t)$ can be plotted as an orbit in the (d_0, S_0) plane, as shown in panel (a) of Fig. (5.5). The stagnation point is ahead of the particle when when the orbit is in the second and fourth quadrants, $d_0 S_0 < 0$, while it is behind the particle when the orbit is in the first or third quadrants, $d_0 S_0 > 0$. The particle moves forward (backward) when the orbit is in the left (right) half plane. The instantaneous power dissipation, Eq. (5.33), is plotted in panel (b), Fig. (5.5). On average, a Chlamydomonas of size 3.5μm swimming at 134μms^{-1} in water at 20°C dissipates approximately 6 fW of power. Both the instantaneous power variation and the average power values are in good agreement with experimental findings [102]. The instantaneous efficiency of translation, defined as ratio of power expended by an external force to maintain a rigid sphere in uniform motion with speed V to that expended chemomechanically to maintain the same speed [104], $\epsilon(t) = 6\pi\eta a V^2/\dot{W}(t)$, is plotted in panel (c), Fig. (5.5). The efficiency is maximum towards the middle and end of the cycle, with the maximum value being close to the theoretical maximum of 20%. The power dissipation as function of the speed, shown in panel (d) of Fig. (5.5), shows the expected quadratic dependence.

5.10 Swirling flows

Like most microorganisms, *Volvox carteri* rotates around its own axis as it swims. Using the minimal representation for the spinlet strength, $\Lambda_0 = -(28/5)\pi\eta a^5\Omega$, and parametrizing uniaxially, $\mathbf{\Lambda} = \Lambda_0(t)(\widetilde{\mathbf{yyy}} - \frac{3}{5}\overbrace{\widehat{\mathbf{y}\mathbb{I}}})$, we are able to capture the short-ranged swirling flow field responsible for self-rotation, Fig. (5.2(b)). Swirling flows due to the vortlet do not contribute to Volvox rotation since they produce swirling flows that spin in opposite directions on the particle surface and thus cancel out, Fig. (5.2(a)). Rotation induced by spinlet swirling flows have a maximum swimming efficiency of 3% in the Lighthill sense [104]. Representing the volvox by a uniaxial spinlet whose strength has been computed using its minimal representation, we calculate the rotational power dissipated by a Volvox of size 200μm rotating at 1rads^{-1} in water at 20°C to be approximately 170 fW. Swirling

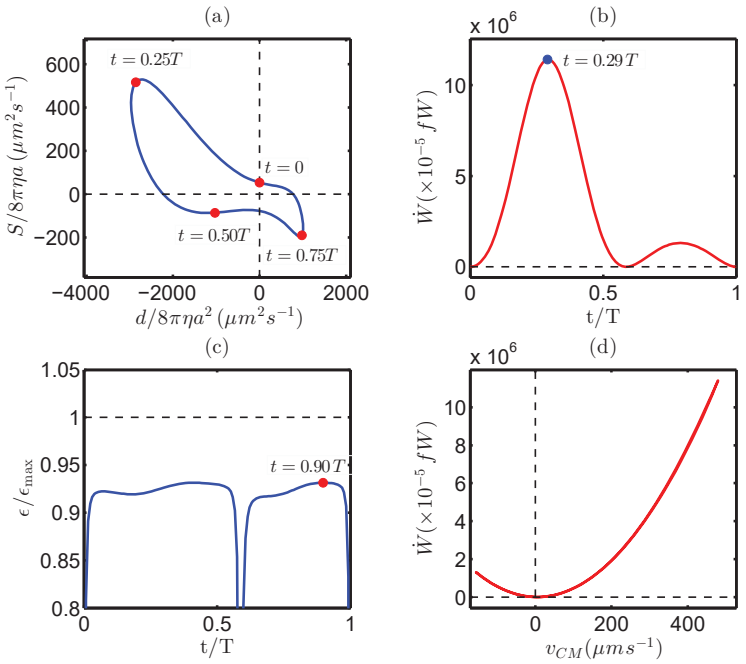

Figure 5.5: Power dissipated and swimming efficiency of Chlamydomonas, computed using a linear combination of a stresslet, a potential dipole and a septlet. Panel (a) shows the variation of the strength of the potential dipole against the stresslet strength, the former estimated from particle image velocimetry data of Chlamydomonas swimming [102]. Panel (b) shows the time variation of the dissipated power, while (d) shows the variation of the power against the translational velocity. Panel (c) shows the relative efficiency which exhibits maxima near the middle and end of the cycle.

flows around Volvox, if experimentally measured, can shed light on the swimming mechanism that must produce the antisymmetric velocity moments on the particle surface.

5.11 Active stress densities

Continuum hydrodynamic descriptions of active matter with stresses of the form $\boldsymbol{\sigma} = -p\mathbb{I} + \eta\left[\boldsymbol{\nabla}\mathbf{v} + (\boldsymbol{\nabla}\mathbf{v})^{\mathrm{T}}\right] + \boldsymbol{\sigma}^{\mathrm{a}}$ were first proposed in [117]. The active stress $\boldsymbol{\sigma}^{\mathrm{a}}$ represents work done on the fluid by the particle. To increase the fluid kinetic energy the solenoidal part of the divergence of the active stress must be nonzero [117]. Constitutive equations for the active stress with this property can be derived by by identifying $\boldsymbol{\nabla}\cdot\boldsymbol{\sigma}^{a}$ with the inhomogeneous force

$$\mathbf{f}_p(\mathbf{r}) = (-1)^{p+1}a^p\,\mathbf{Q}^{(p+1)}\odot\boldsymbol{\nabla}^{(p)}\left[1 + a^2\nabla^2/(4p+6)\right]\delta(\mathbf{r}) \tag{5.35}$$

Writing the active stress in terms of symmetric and antisymmetric parts as $\boldsymbol{\sigma}^{a} = \boldsymbol{\sigma}^{s} + \boldsymbol{\epsilon}\cdot\mathbf{A}$ we obtain

$$\boldsymbol{\sigma}^{s}(\mathbf{r}) = \left(1 + \frac{a^2\nabla^2}{10}\right)\mathbf{S} + \frac{2}{5}\,\widetilde{\boldsymbol{\nabla}\mathbf{d}} - \left(1 + \frac{a^2\nabla^2}{14}\right)\boldsymbol{\nabla}\cdot\boldsymbol{\Gamma} \tag{5.36a}$$

$$\mathbf{A}(\mathbf{r}) = \frac{4}{3}\left(1 + \frac{a^2\nabla^2}{14}\right)\boldsymbol{\nabla}\cdot\boldsymbol{\Psi} - \frac{3}{4}\left(1 + \frac{a^2\nabla^2}{18}\right)\boldsymbol{\nabla}\boldsymbol{\nabla} : \boldsymbol{\Lambda} \tag{5.36b}$$

where tensorial densities are now defined for a suspension of n particles located at $\mathbf{r}_n$ as $\mathbf{S}(\mathbf{r}) = \sum_n \mathbf{S}_n\delta(\mathbf{r}-\mathbf{r}_n)$ and similarly for the remaining multipoles.

Symmetric states of active stress have been considered previously in the literature [23, 118, 28] in the $a \to 0$ limit and for uniaxial stresslets and the potential dipole. Our derivation shows that stresslet contribution includes a finite size correction and is generally biaxial. The septlet, not considered previously, contributes at the same order in gradients as the potential dipole and produces a long range r^{-3} flow. Thus, it is of equal importance as the potential dipole for collective hydrodynamics.

Antisymmetric states of active stress, to the best of our knowledge, have not been considered in the literature before , though antisymmetric stresses in passive nematics have been studied [119, 120]. Angular momentum conservation dictates that such states of stress can exist only when the medium has an internal "spin" angular momentum $\mathbf{l}$ over and above the orbital angular momentum $\mathbf{r}\times\mathbf{v}$. Antisymmetric stresses couple spin angular momentum to linear momentum through the pair of conservation equations $\partial\mathbf{v} = \boldsymbol{\sigma}^s + \boldsymbol{\nabla}\times\mathbf{A}$, $\partial\mathbf{l} = \boldsymbol{\nabla}\cdot\mathbf{c} - \mathbf{A}$. This implies that self-rotating particles, through their hydrodynamic interaction, can set up spontaneous macroscopic flows in suspension. This is macroscopic manifestation of the translational velocity $(1 + a^2\nabla^2/6)\,\mathbf{u}^{(\Lambda)}$ of a passive particle at $\mathbf{r}$ induced by a spinlet at the origin.

Further, self-rotating particles with spinlets and/or particles with septlets must be described in the continuum by third rank tensorial theories. Thus the new stress terms above allow us to generalize current second-order tensorial theories of active matter [23, 25] to higher-order tensorial order theories of active multipolar continua. For swimming microorganisms like Chlamydomonas generating time-varying flows, the stress multipoles appearing in Eq. (5.36) are time-dependent, and so is the stress tensor $\boldsymbol{\sigma}^a$. In a collection of such active particles, the phase of the stress tensor thus depends on the relative locations of individual particles. Tuned correctly, this can lead to long-range hydrodynamically synchronized oscillations or rotations in an collection of microswimmers.

5.12 Conclusion

The close agreement of our results for the flow field, power dissipation, and efficiencies with those of [102, 103] shows the efficacy of our minimal irreducible multipole expansion for studying complex time-dependent flows around active particles. This expansion forms the basis of a method to obtain many-body hydrodynamic interactions in a suspension of finite-sized microswimmers. The method can be used to obtain the rheology of

a microswimmer suspension including hydrodynamic interactions to second order in volume fraction. We urge the experimental verification of the swirling flows around rotating microswimmers and the separate conservation of orbital and angular momentum that we have reported here.

Chapter 6

Instabilities of active and sedimenting passive filaments

In this chapter we construct a filament out of individual active spheres by coupling them with local elastic potentials and write down its equation of motion in the limit $a \to 0$ using a minimal stresslet description. Numerical simulations of this equation have revealed [121] that the active filament is hydrodynamically destabilized and displays a complex combinations of translational and rotational motions that, when constrained by clamping one end of the filament, evolve into periodic biomimetic oscillations [122]. Here we demonstrate the necessity of hydrodynamic interactions (HI) for oscillatory filament motions through a continuum spectral analysis under the free-draining approximation. We further linearize the discrete equation of motion and use it to study the stability of a *passive* filament sedimenting under an external force.

6.1 Stokes flow due an active filament

In Ch. (5) we have studied flows in a viscous fluid generated due to spherical particles that convert chemical energy into mechanical work. Our formulation has enabled us to

analyze and reproduce flows due to microorganisms such as Chlamydomonas and Volvox. There are ample instances in biology, however, where the conversion of chemical to mechanical energy is not confined to a particle-like element but is, instead, distributed over a line-like element. Such a situation arises, for example, in a microtubule with a row of molecular motors converting energy while walking on it. The mechanical energy thus obtained not only produces motion of the motors but also generates reaction forces on the microtubule, which can deform elastically in response. Since both motor and microtubule are surrounded by a fluid, hydrodynamic interactions between the motors and between segments of the microtubule destabilize the system, leading to autonomous motility. This combination of elasticity, autonomous motility through energy conversion and hydrodynamics is found in biological as well as biomimetic contexts.

Biological examples of such motion include prokaryotic bacteria [123] as well as eukaryotic sperm cells [124, 125], which employ rhythmic flagellar beating for locomotion in viscous fluids. Bacterial flagella rotate rigidly in corkscrew fashion [126, 127], while spermatic flagella behave more like flexible oars [128] with their beating mostly confined to a plane [129, 130, 131]. Oscillatory motility in clamped flagella can arise spontaneously and, with an unlimited supply of energy, can persist indefinitely without any external or internal regulatory pacemaker mechanism [125, 132]. Recent biomimetic examples are provided by mixtures of motors which crosslink and walk on polymer bundles. A remarkable cilia-like beating phenomenon is observed in these systems [26, 27]. A polymer in which the monomeric units are autocatalytic nanorods provides a nonbiological example of energy conversion on linear elastic elements. Though such elements are yet to be realized in the laboratory, active elements coupled to passive components through covalent bonds have been synthesized [19] and may lead to new kinds of nanomachines [20].

Motivated by these biological and biomimetic examples, we have studied a semiflexible elastic filament immersed in a viscous fluid with active spheres distributed along its length. Extending our treatment of Ch. (5), we have written an equation of motion for the

filament that incorporates the effects of nonlinear elastic deformation, active processes and nonlocal Stokesian hydrodynamic interactions. A thorough numerical study of the dynamics of such filaments has been carried out in [121] and [122] in the limit of $a \to 0$, where a is the radius of an individual sphere. It has been shown that an initially straight filament, either free at both ends or clamped at one end, is hydrodynamically unstable to transverse perturbations. The autonomous motility of the free filament of the former, when constrained by a clamp, resulted in biomimetic beating of the type discussed above. In the following sections we set up the equation of motion for an active filament and analyze it spectrally, both in the discrete and continuum limits.

6.2 Equation of motion for an active filament

We begin by extending our single-particle flow equation of Ch. (5) to that for N particles. The total flow at any bulk point $\mathbf{r}$ due to N particles is, thanks to the linearity of the Stokes equation, a simple linear sum of the flows due to each particle. Thus we extend our boundary integral formalism to write

$$8\pi\eta\,\mathbf{u}(\mathbf{r}) = -\sum_{j=1}^{N}\int_{S_j}\mathbf{G}(\mathbf{r}-\mathbf{r}_j)\cdot\mathbf{q}_j\,\mathrm{d}S_j \tag{6.1}$$

where $\mathbf{r}_j$ are the coordinates of any point on the surface of particle j centred at $\mathbf{R}_j$. The motion of the ith particle can now be obtained by equating $\mathbf{r} = \mathbf{r}_i$ and using the boundary condition $\mathbf{u}^S(\mathbf{r}_i) = \mathbf{V} + a\boldsymbol{\Omega}\times\hat{\mathbf{r}}_i + \mathbf{v}^{\mathrm{a}}(\mathbf{r}_i)$,

$$\mathbf{V}_i + \langle\mathbf{v}^{\mathrm{a}}\rangle_i = -\frac{1}{6\pi\eta a}\int_{S_j}\mathbf{q}_j\,\mathrm{d}S_j - \frac{1}{8\pi\eta}\left\langle\sum_{j\neq i}\int_{S_j}\mathbf{G}(\mathbf{r}_i-\mathbf{r}_j)\cdot\mathbf{q}_j\,\mathrm{d}S_j\right\rangle_{S_i} \tag{6.2}$$

where we have averaged over the surface of the ith sphere. Since $\nabla^4\mathbf{u} = 0$ for Stokes flow, we use the mean value theorem for biharmonic functions to evaluate the surface mean

over S_i :

$$\begin{aligned}\mathbf{V}_i + \langle \mathbf{v}^{\mathrm{a}} \rangle_i &= \frac{\mathbf{f}_i^{\mathrm{ext}}}{6\pi\eta a} - \frac{1}{8\pi\eta}\left(1 + \frac{a^2}{6}\nabla_i^2\right)\sum_{j\neq i}\int_{S_j} \mathbf{G}(\mathbf{R}_i - \mathbf{r}_j)\cdot\mathbf{q}_j \,\mathrm{d}S_j \\ &= \frac{\mathbf{f}_i^{\mathrm{ext}}}{6\pi\eta a} - \frac{1}{8\pi\eta}\left(1 + \frac{a^2}{6}\nabla_i^2\right)\sum_{j\neq i}\sum_{p=0}^{\infty} a^p\, \mathbf{Q}^{(p+1)} \odot \boldsymbol{\nabla}_j^{(p)} \cdot \left(1 + \frac{a^2}{4p+6}\nabla_j^2\right)\mathbf{G}(\mathbf{R}_i - \mathbf{r}_j)\end{aligned} \tag{6.3}$$

where we have used Eq. (5.12). Here we have equated the surface integral of the traction jump with the net external force $\mathbf{f}^{\mathrm{ext}}$ on the particle. Expanding into irreducible components, we obtain

$$\begin{aligned}8\pi\eta\left(\mathbf{V}_i + \langle \mathbf{v}^{\mathrm{a}} \rangle_i\right) = \frac{4\mathbf{f}_i^{\mathrm{ext}}}{3a} - \left(1 + \frac{a^2}{6}\nabla_i^2\right)\sum_{j\neq i}\Bigg[&\left(1 + \frac{a^2}{6}\nabla_j^2\right)\mathbf{G}(\mathbf{R}_i - \mathbf{R}_j)\cdot\mathbf{F}_j \\ &+ \left(1 + \frac{a^2}{10}\nabla_j^2\right)\boldsymbol{\nabla}_j\mathbf{G}(\mathbf{R}_i - \mathbf{R}_j)\odot\mathbf{S}_j \\ &+ \frac{1}{5}\nabla_j^2\,\mathbf{G}(\mathbf{R}_i - \mathbf{R}_j)\cdot\mathbf{d}_j \\ &- \left(1 + \frac{a^2}{14}\nabla_j^2\right)\boldsymbol{\nabla}_j\boldsymbol{\nabla}_j\mathbf{G}(\mathbf{R}_i - \mathbf{R}_j)\odot\boldsymbol{\Gamma}_j\Bigg]\end{aligned} \tag{6.4}$$

where we have retained only translational multipoles upto long-range order , that is, upto r^{-3}, and have identified the stokeslet $\mathbf{F}$ with the external force $\mathbf{f}^{\mathrm{ext}}$. This is the equation of motion for a collection of N active spheres, each of finite radius a, under some external force and interacting hydrodynamically.

We simplify the analysis by taking the limit $a \to 0$, which allows us to neglect the Faxén corrections. We now create a filament out of these active point particles by introducing local elastic and nonlocal self-avoiding potentials,

$$U(\mathbf{R}_1, \ldots, \mathbf{R}_N) = \sum_{j=1}^{N-1} U_{\mathrm{S}}(\mathbf{b}_j) + \sum_{j=1}^{N-2} U_{\mathrm{B}}(\mathbf{b}_j, \mathbf{b}_{j+1}) + \frac{1}{2}\sum_{j,i=1}^{N} U_{\mathrm{LJ}}(\mathbf{R}_i - \mathbf{R}_j). \tag{6.5}$$

The two-body harmonic spring potential $U_{\mathrm{S}}(\mathbf{b}_j) = \frac{1}{2}k(b_j - b_0)^2$ penalizes departures of b_j, the modulus of the bond vector $\mathbf{b}_j = |\mathbf{R}_j - \mathbf{R}_{j+1}|$, from its equilibrium value of b_0.

The three-body bending potential $U_{\mathrm{B}}(\mathbf{b}_j, \mathbf{b}_{j+1}) = \bar{\kappa}(1 - \cos\phi_j)$ penalizes departures of the angle ϕ_j between consecutive bond vectors from its equilibrium value of zero. The rigidity parameter $\bar{\kappa}$ is related to the bending rigidity as $\kappa = b_0\bar{\kappa}$. The repulsive Lennard-Jones potential U_{LJ} vanishes if the distance between beads $R_{ij} = |\mathbf{R}_j - \mathbf{R}_i|$ exceeds σ_{LJ}. The i-th bead thus experiences a force $\mathbf{F}_i = -\partial U/\partial \mathbf{R}_i$ when the filament stretches or bends from its equilibrium position. With the above choice of potential the connected beads approximate an inextensible, semiflexible, self-avoiding filament. The equation of motion for this filament can then be written as

$$8\pi\eta\,\partial_t \mathbf{R}_i = \sum_{j=1}^{N}\Bigg[\mathbf{G}(\mathbf{R}_i - \mathbf{R}_j)\cdot\mathbf{F}_j - \boldsymbol{\nabla}_j\mathbf{G}(\mathbf{R}_i - \mathbf{R}_j)\odot\mathbf{S}_j \\ - \frac{1}{5}\nabla_j^2\,\mathbf{G}(\mathbf{R}_i - \mathbf{R}_j)\cdot\mathbf{d}_j + \boldsymbol{\nabla}_j\boldsymbol{\nabla}_j\mathbf{G}(\mathbf{R}_i - \mathbf{R}_j)\odot\boldsymbol{\Gamma}_j\Bigg] \tag{6.6}$$

where the stokeslet term arises because of elasticity and self-avoidance, and the rest are purely active terms. The numerical analysis of [121] and [122] has been carried out using the stokeslet and stresslet terms of this equation. We shall base our stability analysis on the same truncated $O(r^{-2})$ equation.

6.3 Continuum equation of motion in the free-draining approximation

The equation of motion for the active filament with the stresslet as the lone active multipole is

$$8\pi\eta\,\partial_t \mathbf{R}_i = \sum_{j=1}^{N}\Big[\mathbf{G}(\mathbf{R}_i - \mathbf{R}_j)\cdot\mathbf{F}_j - \boldsymbol{\nabla}_j\mathbf{G}(\mathbf{R}_i - \mathbf{R}_j)\odot\mathbf{S}_j\Big] \tag{6.7}$$

In the free-draining approximation, we consider only diagonal contributions from the stokeslet and the nearest-neighbor contributions from the stresslet. Thus we get

$$8\pi\eta\,\partial_t \mathbf{R}_i = \frac{4\mathbf{F}_i}{3a} - \boldsymbol{\nabla}_i \mathbf{G}(\mathbf{R}_i - \mathbf{R}_{i-1}) \odot \mathbf{S}_{i-1} - \boldsymbol{\nabla}_i \mathbf{G}(\mathbf{R}_i - \mathbf{R}_{i+1}) \odot \mathbf{S}_{i+1} \tag{6.8}$$

where a is the effective bead radius, which we set equal to b_0. The flow contribution from the nearest neighbors are proportional to the local curvature $\varkappa$ and point outwards along the local unit normal $\hat{\mathbf{n}}$ [121]. Therefore,

$$8\pi\eta\,\partial_t \mathbf{R}_i = \frac{4\mathbf{F}_i}{3b_0} - \frac{2S_0}{b_0}\varkappa\hat{\mathbf{n}}. \tag{6.9}$$

Here S_0 is the stresslet strength and has been taken such that $S_0 > 0$ represents an extensile "pusher" stresslet, and $S_0 < 0$ represents a contractile "puller" stresslet.

We convert this equation to continuum form by converting the particle index to the arclength parameter, $i \to s$, and then using $\mathbf{R}_i \to \mathbf{R}(s,t)$ and $\varkappa\mathbf{n} \to \partial_s \mathbf{R}$ to represent a point on the filament and the local curvature respectively. The Hamiltonian for the elastic term is

$$H = \frac{\epsilon}{2}\int \mathrm{d}s(\partial_s^2 \mathbf{R})^2 \tag{6.10}$$

where ϵ is the bending constant. Using Hamilton's principle, the equation of motion is

$$\partial_t \mathbf{R}(s,t) = -\frac{\kappa L}{6\pi\eta b_0}\partial_s^4 \mathbf{R} - \frac{S_0}{4b_0}\partial_s^2 \mathbf{R} \tag{6.11}$$

where $L = (N-1)b_0$ is the total filament length and $\kappa = \epsilon L$ is the bending rigidity defined earlier. We nondimensionalize the arclength parameter by the filament length L and time by $\kappa/6\pi\eta L^3 b_0$, where $\Gamma_\kappa = \kappa/\eta L^3 b_0$ is the elastic relaxation rate [121]. We finally obtain

$$\partial_t \mathbf{R}(s,t) = -\left(\partial_s^4 + \alpha\partial_s^2\right)\mathbf{R}(s,t) \tag{6.12}$$

where $\alpha = 3LS_0/2\kappa$, a scaled measure of the relative strength of the activity, is the continuum analogue of the activity number introduced in [121]. Separating variables, $\mathbf{R}(s,t) = T(t)\,\mathbf{u}(s)$, and writing $\dot{T}(t)\,\mathbf{u}(s) = -T(t)\,[\mathbf{u}''''(s) + \alpha\mathbf{u}''(s)] = \lambda$ where λ sets the timescale and primes imply differentiation with respect to s, we immediately obtain the temporal evolution

$$T(t) = e^{\lambda t}T(0). \tag{6.13}$$

The spatial part takes the Rayleigh-like form

$$\mathbf{u}''''(s) + \alpha\mathbf{u}''(s) + \lambda\mathbf{u}(s) = 0 \tag{6.14}$$

In the absence of activity, this reduces to the Euler-Bernoulli solution [133] of the biharmonic operator.

6.4 Hydrodynamic interactions necessary for active filament oscillations

It is immediately obvious from the temporal equation, Eq. (6.13), that the filament is linearly unstable to small perturbations if $Re(\lambda) > 0$. In addition, the λ must be complex to admit oscillatory modes. Expanding the spatial part in eigenfunctions, $\mathbf{u}(s) = \sum_n \mathbf{a}_n u_n(s)$ where $\mathbf{a}_n$ are the amplitudes and the mode shapes $u_n(s)$ are eigenfunctions of the differential operator $\mathcal{L} = \partial_s^4 + \alpha\partial_s^2$. The trial solution

$$u_n(s) = \sum_{j=1}^{4} A_{j,n} e^{ik_{j,n}s} \tag{6.15}$$

gives the dispersion relation $k_{j,n}^4 - \alpha k_{j,n}^2 + \lambda_n = 0$ where the wavenumbers $k_{j,n}$ are

$$k_{1,n} = +\sqrt{\frac{1}{2}\left(\alpha + \sqrt{\alpha^2 - 4\lambda_n}\right)} \qquad k_{2,n} = +\sqrt{\frac{1}{2}\left(\alpha - \sqrt{\alpha^2 - 4\lambda_n}\right)}$$
$$k_{3,n} = -\sqrt{\frac{1}{2}\left(\alpha + \sqrt{\alpha^2 - 4\lambda_n}\right)} \qquad k_{4,n} = -\sqrt{\frac{1}{2}\left(\alpha - \sqrt{\alpha^2 - 4\lambda_n}\right)}. \tag{6.16}$$

This gives $k_{3,n} = -k_{1,n}$ and $k_{4,n} = -k_{2,n}$ so that are only two independent wavenumbers per mode. Also, $k_{1,n}^2 + k_{2,n}^2 = \alpha$ and $k_{1,n}^2 k_{2,n}^2 = \lambda$. The mode shapes are therefore

$$u_n(s) = C_{1,n}\cos(k_{1,n}s) + C_{2,n}\sin(k_{1,n}s) + C_{3,n}\cos(k_{2,n}s) + C_{4,n}\sin(k_{2,n}s) \tag{6.17}$$

where $C_{1,n} = (A_{1,n} + A_{3,n})$, $C_{2,n} = i(A_{1,n} - A_{3,n})$, $C_{3,n} = (A_{2,n} + A_{4,n})$ and $C_{4,n} = i(A_{2,n} - A_{4,n})$ are real. Using this equation, we can obtain the eigenspectrum for any set of boundary conditions.

The complex motion of the free filament [121] and the oscillatory motion of the clamped filament [122] are possible only if the spectrum is complex. Such oscillatory modes are not possible if, for those boundary conditions, the differential operator $\mathcal{L}$ is self-adjoint. This is true if, for all mode numbers n and m, the integral

$$\mathcal{I} = \int_0^1 \mathrm{d}s\Big[u_m(s)\mathcal{L}(u_n(s)) - u_n(s)\mathcal{L}(u_m(s))\Big] = 0 \tag{6.18}$$

for the particular boundary condition employed. For the free-draining active filament we have

$$\mathcal{I} = \int_0^1 \mathrm{d}s\Big[u_m(s)\left\{u_n''''(s) + \alpha u_n''(s)\right\} - u_n(s)\left\{u_m''''(s) + \alpha u_m''(s)\right\}\Big] \tag{6.19}$$

Integrating by parts, we get

$$\mathcal{I} = \left[u_m(s) \left\{ u_n'''(s) + \alpha u_n'(s) \right\} - u_n(s) \left\{ u_m'''(s) + \alpha u_m'(s) \right\} - u_m'(s) u_n''(s) + u_n'(s) u_m''(s) \right]_0^1 \tag{6.20}$$

Each end of the filament can be free to move, can be clamped or hinged to a support, or can be allowed to slide along the support. The corresponding boundary conditions are [133]

$$\text{Free}: \; u_n'' = 0 \; ; \; u_n''' + \alpha u_n' = 0 \tag{6.21a}$$

$$\text{Clamped}: \; u_n = 0 \; ; \; u_n' = 0 \tag{6.21b}$$

$$\text{Hinged}: \; u_n = 0 \; ; \; u_n'' = 0 \tag{6.21c}$$

$$\text{Sliding}: \; u_n' = 0 \; ; \; u_n''' = 0 \tag{6.21d}$$

Substituting these in Eq. (6.20) we find that $\mathcal{I} = 0$ for any pair of combinations and that $\mathcal{L}$ is always self-adjoint. This remarkable result shows that an active filament cannot have oscillatory modes under the free-draining approximation, and hence demonstrates the necessity of hydrodynamic interactions for biomimetic beating.

6.5 Linearized discrete equation of motion of an active filament

It is not, to the best of our knowledge, possible to write down a continuum equation of motion for the active filament with complete hydrodynamic interactions (HI). However, our analysis of the previous section highlights the necessity of HI in filament oscillations. This requires a spectral analysis of the discrete equation of motion, Eq. (6.7). A numerical linear stability analysis of this equation, carried out in [122] for a filament clamped at one end, failed to observe oscillatory instabilities in the absence of HI and thus reiterated the

result of the previous section. Here we linearize Eq. (6.7) analytically and analyze the eigenvalues and eigenmodes of the linearized Jacobian matrix.

We redefine notation so that $\mathbf{r}_i$ now denotes the position of the i-th active bead, $\mathbf{R}_i$ denotes the steady state position and $\boldsymbol{\rho}_i$ denotes small displacements from the steady state, $\mathbf{r}_i = \mathbf{R}_i + \boldsymbol{\rho}_i$ for all i. Taylor expanding about $\mathbf{R}_j$ to first order in $\boldsymbol{\rho}_j$, we get expression like $\mathbf{G}(\mathbf{r}_i - \mathbf{r}_j) = \mathbf{G}(\mathbf{R}_i - \mathbf{R}_j) + \nabla_j \mathbf{G}(\mathbf{R}_i - \mathbf{R}_j) \cdot \boldsymbol{\rho}_j$, where $\nabla_j \mathbf{G}(\mathbf{R}_i - \mathbf{R}_j) = \nabla_j \mathbf{G}(\mathbf{r}_i - \mathbf{r}_j)\,|_{\boldsymbol{\rho}=\mathbf{0}}$. The linearized equation of motion becomes

$$8\pi\eta\, \partial_t \boldsymbol{\rho}_i = \sum_{j=1}^{N} \Big[\mathbf{G}(\mathbf{R}_i - \mathbf{R}_j) \cdot \boldsymbol{\nabla}\mathbf{F}_j + \boldsymbol{\nabla}\mathbf{G}(\mathbf{R}_i - \mathbf{R}_j) \cdot \Big(\mathbf{F}_j + \boldsymbol{\nabla}\mathbf{S}_j\Big) + \boldsymbol{\nabla}\boldsymbol{\nabla}\mathbf{G}(\mathbf{R}_i - \mathbf{R}_j) \cdot \mathbf{S}_j \Big] \cdot \boldsymbol{\rho}_j. \tag{6.22}$$

The eigenvalues of the linearized Jacobian matrix of the filament, $\mathbf{J} = \mathbf{G} \cdot \boldsymbol{\nabla}\mathbf{F} + \boldsymbol{\nabla}\mathbf{G} \cdot (\mathbf{F} + \boldsymbol{\nabla}\mathbf{S}) + \boldsymbol{\nabla}\boldsymbol{\nabla}\mathbf{G} \cdot \mathbf{S}$ determine the stability of the active filament.

6.6 Spectral analysis of a passive sedimenting filament

Since a numerical analysis of the stability of the *active* filament has already been carried out [122], here we employ the linearized Jacobian to study the stability of the equivalent *passive* filament sedimenting under some external force, for example, gravity. The corresponding linearized equation of motion is

$$8\pi\eta\, \partial_t \boldsymbol{\rho} = \mathbf{J}^{passive} \cdot \boldsymbol{\rho} \tag{6.23}$$

where $\mathbf{J}^{passive} = \mathbf{G} \cdot \boldsymbol{\nabla} \Big(\mathbf{F}^{el} + \mathbf{F}^{ext}\Big) + \boldsymbol{\nabla}\mathbf{G} \cdot \Big(\mathbf{F}^{el} + \mathbf{F}^{ext}\Big)$. Here $\mathbf{F}^{el}$ incorporates elastic as well as Lennard-Jones forces. The stability of the filament depends on the interplay of the elastic restoring forces and the external forces, as well as the strength of the HI. Estimating the curvature elastic force as κ/L^2, where $L = (N-1)b_0$ is the length of the filament, we obtain a dimensionless measure of this interplay, the "sedimentation number" $\mathcal{S} = L^2 f_{ext}/\kappa$. This

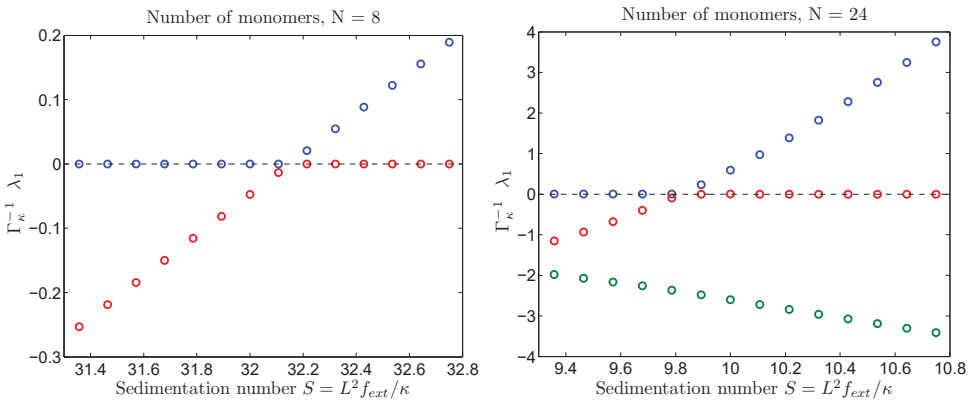

(a) $L = 28$ (b) $L = 92$

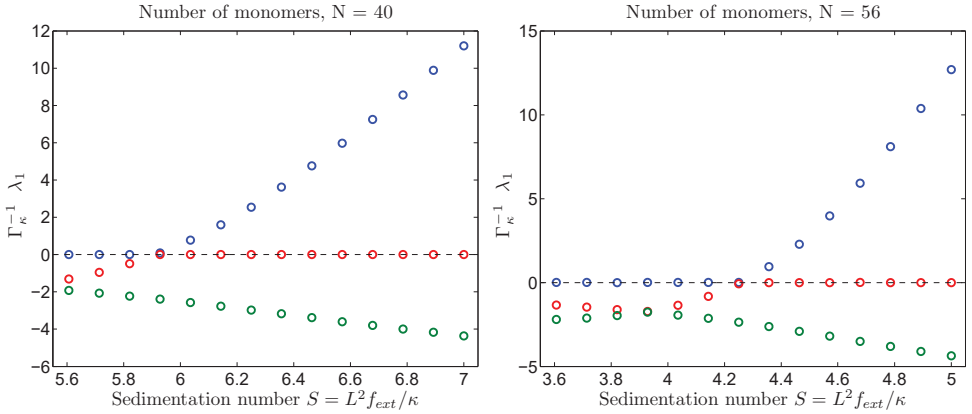

(c) $N = 156$ (d) $N = 220$

Figure 6.1: Variation of the first few eigenvalues of the sedimenting filament with sedimentation number $\mathcal{S}$, plotted for various values of length L. The colors are somewhat misleading in this figure, and do not represent the same mode all the way through. In (a), for example, we have plotted the first and the fourth modes, λ_1 and λ_4. The former, initially indicated by blue markers, is always zero, and lies along the x-axis. The latter, initially indicated by red markers, is initially negative and then rises monotonically with $\mathcal{S}$, crosses over at $\mathcal{S}_c \approx 32.15$, and continues on. We have plotted λ_1, λ_4 and λ_5 (initially green markers) for the other plots. The bending constant is $\kappa = 0.5$, the Lennard-Jones cutoff is $r_{min} = 2$ and the equilibrium bond length is $b_0 = 4$. The elastic timescale is $\Gamma_\kappa = \kappa/\eta L^4$.

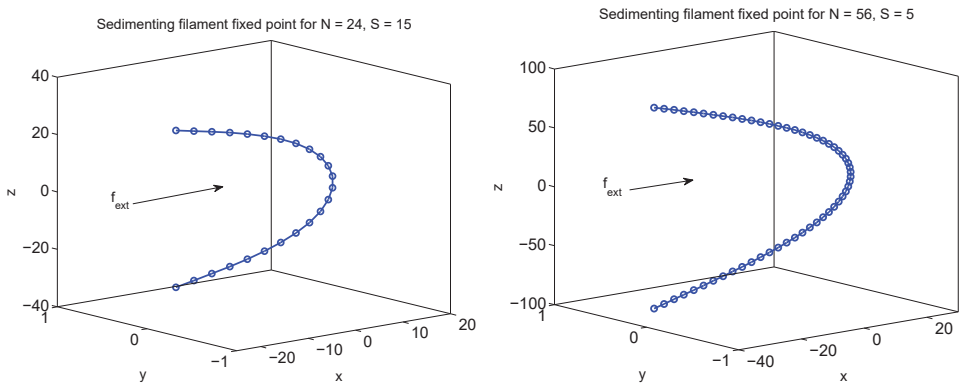

(a) $L = 92, \mathcal{S} = 15$ (b) $L = 220, \mathcal{S} = 5$

Figure 6.2: Bow-shaped fixed point of the sedimenting elastic filament for various values of L and $\mathcal{S}$. The bending constant is $\kappa = 0.5$, the Lennard-Jones cutoff is $r_{min} = 2$ and the equilibrium bond length is $b_0 = 4$.

L	28	60	92	124	156	188	220
$\mathcal{S}_c$	32.15	14.85	9.82	7.37	5.91	4.95	4.26

Table 6.1: Values of the sedimentation number $\mathcal{S}_c$ at which the instability transition takes place, tabulated for various values of length L. Parameter values are bead radius $a = 1$, equilibrium bond length $b_0 = 4$, Lennard-Jones cutoff $r_{min} = 2$, spring constant $k = 1$, and bending constant $\kappa = 0.5$.

is similar to the measure used in [134], and is an analogue of the activity number used in [121] and [122]. The filament is expected to be stable at low values of $\mathcal{S}$ where the elastic restoring force dominates. At higher values, the external force as well as the effect of HI becomes more prominent.

We first lay out the filament horizontally with the beads distributed at equal intervals and $\mathbf{F}^{ext}$ acting downwards. We evolved the system until it reached a steady state bow conformation, shown in Fig. (6.2). We use the coordinates of the beads in this conformation to calculate the spectrum of $\mathbf{J}^{passive}$ for various values of L and $\mathcal{S}$. We observe an instability transition at a critical value $\mathcal{S}_c$ when one of the initially negative eigenvalues become positive, Fig. (6.1). We do not observe such instabilities are not seen if HI is switched off. The critical values $\mathcal{S}_c$ for various L are given in Table (6.1).

6.7 Conclusion

The elastic filament of active elements with hydrodynamic interactions provides one of the simplest minimal models of flagella and cilia, and displays extraordinary lifelike autonomous motility when destabilized. Our analysis of the continuum filament in the free-draining limit shows the importance of hydrodynamic interactions in the realization of such biomimetic motions. We have computed the Jacobian of the linearized discrete equation of motion and have used it to estimate the stability of a sedimenting passive filament. We have found that such a filament, initially laid horizontally in a viscous fluid, destabilizes beyond a critical value of the sedimentation number, a dimensionless measure of the interplay between the external force and elastic restoring force. In the future we intend to study the transition to instability from numerical simulations of Eq. (6.23). We also intend to carry out a more detailed stability analysis of the active filament for various boundary conditions using Eq. (6.22).

Numerical simulations of the filament reveals the transition to instability rather beautifully, and shows a rich flow field structure, as can be seen in these videos.

Chapter 7

Conclusions

In this thesis we have studied various far-from-equilibrium phenomena in living matter both in the macroscale and in the microscale. In the first part of the thesis we have studied the effects of intracellular and population fluctuations in models of enzyme kinetics and epidemics respectively, and have been pleasantly surprised to observe counter-intuitive and ordered effects of intrinsic noise that are possible only in systems far from equilibrium. In particular, we have observed the curious phenomenon of the maximization of orderliness for intermediate noise amplitudes in two very different models that exist at very different length and timescales.

In the second part of the thesis we have studied the motion of chemomechanically active particles that transduce chemical energy into mechanical work. We have solved the Stokes equation for a single chemomechanically active sphere, and have presented active flows in terms of fundamental irreducible components, a minimal combination of which can reproduce essential features of the complex nonequilibrium flow around swimming microorganisms. We have, through stability analysis, shown that hydrodynamic interactions are essential for the nontrivial lifelike motions of active filaments as well as to induce instabilities in sedimenting passive filaments.

In the future, we intend to extend the memory-indicator study of antibunching of intervals

in enzyme kinetics to second order well-mixed enzyme kinetics, allowing for fluctuations in the number of substrate molecules. We also intend the use the technique of Chapter (4) to study the effects of noise in the repressilator [135] model of cellular clocks. We intend to investigate the role of stochastic coherence in the efficiency of such clocks, since the analysis of this Chapter (4) shows that the phenomenon of noise-induced oscillations and stochastic coherence can generically be expected in non-equilibrium birth-death jump Markov processes which can be reduced to the standard multivariate Ornstein-Uhlenbeck form by a successive application of two linearization procedures: the linear noise approximation followed by a linearization about the fixed point of the system. We intend to extend these studies into the spatial domain by allowing diffusion to play a role. For the reaction-diffusion enzyme system we expect to see the formation of patterns. We also intend to look for a continuous phase transition to an absorbing state, and seek to analytically calculate and numerically compute values of critical exponents, hopefully by mapping onto a directed percolation problem. We also hope to study the SIRS epidemic system numerically in linear, planar and cubic geometries, and look for patterns.

In the future we intend to extend the linear relationship between the irreducible multipoles of stress and velocity for a single sphere to a collection of identical active spheres, obtaining the N-body relation $\mathbf{V}_i^{(p+1)} = \mathcal{G}_{ij}^{(p+1,p'+1)} \odot \mathbf{Q}_j^{p'+1}$, where particles are indexed by i and j. We can thus, by using this irreducible formalism, solve the true many-body hydrodynamic problem of N interacting active particles. This will give the hydrodynamically induced corrections to the force multipoles. Thus, a particle may not have a certain stress multipole itself, but, the presence of another particle can induce such a contribution. This is the essence of the hydrodynamic interaction. For the Dirichlet problem, this will require a linear system to be solved, which is the basis of the Stokesian dynamics method in unbounded domains [136] or in periodic boundaries [113]. This work is currently in progress. This entire exercise can be repeated for 1 or N active particles near a wall using appropriate image systems [137].

The inclusion of hydrodynamic interactions immediately allows us to calculate the suspension rheology in the manner of [138, 113, 139] to semi-dilute order. We shall study the stability of an active suspension where stresslets and vortlets can be *biaxially* oriented as well as septlets and spinlets that can be biaxially or even *triaxially* oriented. Our investigations will include the possibility of studying pattern formations and fluid mixing using our minimal irreducible formalism.

Furthermore, it is now clear that stresses in active micropolar continua must have an antisymmetric part due to the coupling between the intrinsic "spin" angular momentum and the linear momentum, and this can lead to the generation of macroscopic flows in a suspension of spinning active particles. Work aimed at constructing appropriate constitutive equations for the stress and the couple stress that arise from the chemomechanical activity of the particles is in progress. We expect to obtain dynamical equations for both the velocity and the intrinsic angular velocity in a generic chemomechanically active fluid and thus derive dispersion relations for the linear hydrodynamic modes.

The study of the stability of active and sedimenting passive filaments can be extended to N filaments interacting hydrodynamically. In the continuum limit, the irreducible formalism can be used for the study of Marangoni effects in active interfaces and active drops.

Finally, tying up the two sub-themes of the thesis together, we intend to study the effects of fluctuations in active suspensions near or far away from walls, with special emphasis on the existence of the Caflisch-Luke paradox of divergent velocity fluctuations in sedimenting suspensions [140, 141].

We have thus encountered some fascinating and nontrivial phenomena exhibited by living matter due to its being out of equilibrium. Life, however, is fleeting and evanescent. A living organism will eventually, and inevitably, come to equilibrium with its surroundings, and die. Herein lies an interesting parallel between the story of life and that of the universe itself, which, at one point of time far into the future must yield to the unstoppable tides of entropy and embrace "heat death". Sadly, or perhaps happily, there will be no life around

to witness that. Or will there? [142]

Appendix A

Useful ingredients

This chapter contains detailed mathematical expressions useful in the study of the hydrodynamics of active Stokes flows. It also contains index forms of expressions used in Ch. (5). Einstein's convention, whereby repeated indices indicate summation, is used by default. The index forms not only provide a quick reference for future calculations, but are also necessary to clarify ambiguities that the tensor notation of the main text might sometimes present.

A.1 Cartesian to spherical polar unit vector transformations

We shall frequently encounter surface integrals of vectorial quantities expressed in spherical polar basis. Since the unit vectors $\hat{\mathbf{r}}$, $\hat{\mathbf{e}}_\theta$ and $\hat{\mathbf{e}}_\phi$ are dependent on the point $\mathbf{r}$, integration is only possible if the vector is expressed in a Cartesian basis. The required transformation

is

$$\begin{pmatrix} \hat{\mathbf{e}}_r \\ \hat{\mathbf{e}}_\theta \\ \hat{\mathbf{e}}_\phi \end{pmatrix} = \begin{pmatrix} \sin\theta\cos\phi & \sin\theta\sin\phi & \cos\theta \\ \cos\theta\cos\phi & \cos\theta\sin\phi & -\sin\theta \\ -\sin\phi & \cos\phi & 0 \end{pmatrix} \begin{pmatrix} \hat{\mathbf{e}}_x \\ \hat{\mathbf{e}}_y \\ \hat{\mathbf{e}}_z \end{pmatrix} \tag{A.1}$$

This can be easily recast in terms of direction cosines : $n_x = x/r = \sin\theta\cos\phi$, $n_y = y/r = \sin\theta\sin\phi$ and $n_z = z/r = \cos\theta$.

$$\begin{pmatrix} \hat{\mathbf{e}}_r \\ \hat{\mathbf{e}}_\theta \\ \hat{\mathbf{e}}_\phi \end{pmatrix} = \begin{pmatrix} n_x & n_y & n_z \\ \partial_\theta n_x & \partial_\theta n_y & \partial_\theta n_z \\ \frac{1}{\sin\theta}\partial_\phi n_x & \frac{1}{\sin\theta}\partial_\phi n_y & \frac{1}{\sin\theta}\partial_\phi n_z \end{pmatrix} \begin{pmatrix} \hat{\mathbf{e}}_x \\ \hat{\mathbf{e}}_y \\ \hat{\mathbf{e}}_z \end{pmatrix} \tag{A.2}$$

which of course reproduces the familiar results $\hat{\mathbf{e}}_\theta = \partial_\theta \widehat{\mathbf{e}}$.

A.2 Green's function and derivatives

The following lists some expressions, in index form, of the derivatives of the Green's function, $\mathbf{G}(\mathbf{r}) = (\mathbb{I} + \hat{\mathbf{r}}\hat{\mathbf{r}})/|\mathbf{r}|^2$ that are extremely useful when computing flows.

$$G_{ij}(\mathbf{r}) = \frac{1}{r}\left(\delta_{ij} + \frac{r_i r_j}{r^2}\right) \tag{A.3a}$$

$$\nabla_\alpha G_{ij}(\mathbf{r}) = \frac{1}{r^3}\left(-r_\alpha\delta_{ij} + r_i\delta_{j\alpha} + r_j\delta_{i\alpha}\right) - \frac{3r_i r_j r_\alpha}{r^5} \tag{A.3b}$$

$$\begin{aligned}\nabla_\alpha\nabla_\beta G_{ij}(\mathbf{r}) = {}& \frac{1}{r^3}\left(-\delta_{ij}\delta_{\alpha\beta} + \delta_{i\beta}\delta_{j\alpha} + \delta_{i\alpha}\delta_{j\beta}\right) + \frac{15r_i r_j r_\alpha r_\beta}{r^7} \\ & - \frac{3}{r^5}\left(-r_\alpha r_\beta\delta_{ij} + r_i r_\alpha\delta_{j\beta} + r_i r_\beta\delta_{j\alpha} + r_j r_\alpha\delta_{i\beta} + r_j r_\beta\delta_{i\alpha} + r_i r_j\delta_{\alpha\beta}\right)\end{aligned} \tag{A.3c}$$

$$\nabla^2 G_{ij}(\mathbf{r}) = \frac{2}{r^3}\delta_{ij} - \frac{6r_i r_j}{r^5} \tag{A.3d}$$

$$\nabla_\alpha\nabla^2 G_{ij} = -\frac{6}{r^5}\left(r_\alpha\delta_{ij} + r_i\delta_{j\alpha} + r_j\delta_{i\alpha}\right) + \frac{30r_i r_j r_\alpha}{r^7} \tag{A.3e}$$

$$\begin{aligned}\nabla_\alpha\nabla_\beta\nabla^2 G_{ij}(\mathbf{r}) = {}& -\frac{6}{r^5}\left(\delta_{ij}\delta_{\alpha\beta} + \delta_{i\beta}\delta_{j\alpha} + \delta_{i\alpha}\delta_{j\beta}\right) - \frac{210\, r_i r_j r_\alpha r_\beta}{r^9} \\ & + \frac{30}{r^7}\left(r_\alpha r_\beta\delta_{ij} + r_i r_\alpha\delta_{j\beta} + r_i r_\beta\delta_{j\alpha} + r_j r_\alpha\delta_{i\beta} + r_j r_\beta\delta_{i\alpha} + r_i r_j\delta_{\alpha\beta}\right)\end{aligned} \tag{A.3f}$$

$$\epsilon_{\nu\alpha j}\nabla_\alpha G_{ij}(\mathbf{r}) = \frac{2}{r^3}\epsilon_{\nu i\mu} r_\mu \tag{A.3g}$$

$$\epsilon_{\nu\alpha j}\nabla_\beta\nabla_\alpha G_{ij}(\mathbf{r}) = \frac{2}{r^3}\epsilon_{\nu i\beta} - \frac{2}{r^5}\epsilon_{\nu i\mu} r_\mu r_\beta \tag{A.3h}$$

A.3 Definitions and embeddings of irreducible stress multipoles

Here we list the definitions of the irreducible stress multipoles in index form.

Force : $$F_i = Q_i^{(1)} \tag{A.4a}$$

Torque : $$T_i = a\epsilon_{i\rho\sigma}Q_{\sigma\rho} \tag{A.4b}$$

Stresslet : $$S_{i\alpha} = \frac{a}{2}\left(Q_{i\alpha} + Q_{\alpha i}\right) \tag{A.4c}$$

Potential Dipole : $$d_i = a^2\,\delta_{\mu\nu}Q_{\mu i\nu} = a^2\,\delta_{\mu\nu}Q_{\mu\nu i} \tag{A.4d}$$

Vortlet : $$D_{i\alpha} = -\frac{a^2}{2}\Big(\epsilon_{i\mu\nu}Q_{\nu\mu\alpha} + \epsilon_{\alpha\mu\nu}Q_{\nu\mu i}\Big) \tag{A.4e}$$

Septlet : $$\Gamma_{i\alpha\beta} = \frac{a^2}{3}\left(Q^{(3)}_{i\alpha\beta} + Q^{(3)}_{\alpha\beta i} + Q^{(3)}_{\beta i\alpha}\right) - \frac{2}{15}\left(d_i\delta_{\alpha\beta} + d_\alpha\delta_{i\beta} + d_\beta\delta_{i\alpha}\right) \tag{A.4f}$$

Spinlet : $$R_{i\alpha\beta} = \frac{a^3}{3}\Big(\epsilon_{i\mu\nu}Q_{\nu\mu\alpha\beta} + \epsilon_{\alpha\mu\nu}Q_{\nu\mu\beta i} + \epsilon_{\beta\mu\nu}Q_{\nu\mu i\alpha}\Big) \tag{A.4g}$$

A.4 Active Stokes flow relations in index notation

Here we provide index forms of some of the important tensorial expressions used in Ch. (5). We begin with the boundary integral, Eq. (5.2),

$$\int_{S'} G_{ij}(\mathbf{r}-\mathbf{r}')q_j(\mathbf{r}')\,\mathrm{d}S' = -8\pi\eta \begin{cases} u_i(\mathbf{r}), & \mathbf{r}\in V \\ u_i^S(\mathbf{r}), & \mathbf{r}\in S, \end{cases} \tag{A.5}$$

The orthogonality of the irreducible Cartesian tensors take the index form

$$\langle \overbrace{\widehat{r}_{i_1 i_2 \ldots i_{p-1} i_p}} \overbrace{\widehat{r}_{j_1 j_2 \ldots j_{q-1} j_q}} \rangle = \frac{p!}{(2p+1)!!}\delta_{p,q}\,\Delta_{i_1 i_2 \ldots i_{p-1} i_p,\, j_1 j_2 \ldots j_{q-1} j_q}. \tag{A.6}$$

The general flow equation, Eq. (5.12), becomes

$$8\pi\eta\, u_i(\mathbf{r}) = (-1)^{p+1}\sum_{p=0}^{\infty} a^p Q_{j\alpha_1\alpha_2\ldots\alpha_{p-1}\alpha_p}\nabla_{\alpha_p\alpha_{p-1}\ldots\alpha_2\alpha_1}\left(1+\frac{a^2}{4p+6}\nabla^2\right)G_{ji} \tag{A.7}$$

The active flow equation containing contribution from $\mathbf{S}$, $\mathbf{d}$, $\boldsymbol{\Upsilon}$, $\boldsymbol{\Gamma}$ and $\boldsymbol{\Lambda}$, Eq. (5.14), is written in index notation as

$$\begin{aligned} 8\pi\eta\, u_i^{\mathrm{a}}(\mathbf{r}) = &\left(1+\frac{a^2}{10}\nabla^2\right)\nabla_\alpha G_{ij}S_{j\alpha} + \frac{1}{5}\nabla^2 G_{ij}d_j + \frac{4}{3}\left(\Upsilon_{\nu\beta}\nabla_\beta\right)\left(\epsilon_{\nu\alpha j}\nabla_\alpha G_{ij}\right) \\ &-\left(1+\frac{a^2}{14}\nabla^2\right)\nabla_\alpha\nabla_\beta G_{ij}\Gamma_{j\alpha\beta} - \frac{3}{4}\left(\Lambda_{\nu\beta\gamma}\nabla_\beta\nabla_\gamma\right)\left(\epsilon_{\nu\alpha j}\nabla_\alpha G_{ij}\right) \end{aligned} \tag{A.8}$$

The Faxén relations, Eq. (5.25), are

$$F_i = -6\pi\eta a\left(V_i + \langle v_i^{\mathrm{a}}\rangle\right) \tag{A.9a}$$

$$T_i = -8\pi\eta a^2\left(a\Omega_i - \frac{3}{2}\left\langle \epsilon_{i\alpha\beta}\, v_\alpha^{\mathrm{a}}\widehat{r}_\beta\right\rangle\right) \tag{A.9b}$$

$$S_{ij} = -10\pi\eta a^2\left\langle v_i^{\mathrm{a}}\widehat{r}_j + v_j^{\mathrm{a}}\widehat{r}_i\right\rangle \tag{A.9c}$$

$$d_i = -30\pi\eta a^3\left\langle v_\alpha^{\mathrm{a}}\widehat{r}_\alpha\widehat{r}_i - \frac{1}{3}v_i^{\mathrm{a}}\right\rangle \tag{A.9d}$$

$$\Upsilon_{ij} = 5\pi\eta a^3\left\langle \epsilon_{i\alpha\beta}\, v_\alpha^{\mathrm{a}}\widehat{r}_\beta\widehat{r}_j + \epsilon_{j\alpha\beta}\, v_\alpha^{\mathrm{a}}\widehat{r}_\beta\widehat{r}_i\right\rangle \tag{A.9e}$$

$$\begin{aligned}\Gamma_{ijk} = -\frac{35\pi\eta a^3}{2}\Big\langle \frac{1}{3}\Big(v_i^{\mathrm{a}}\widehat{r}_j\widehat{r}_k + v_j^{\mathrm{a}}\widehat{r}_k\widehat{r}_i + v_k^{\mathrm{a}}\widehat{r}_i\widehat{r}_j\Big) - \frac{2}{15}v_\alpha^{\mathrm{a}}\widehat{r}_\alpha\Big(\widehat{r}_i\,\delta_{jk} + \widehat{r}_j\,\delta_{ki} + \widehat{r}_k\,\delta_{ij}\Big)\\ - \frac{1}{15}\Big(v_i^{\mathrm{a}}\,\delta_{jk} + v_j^{\mathrm{a}}\,\delta_{ki} + v_k^{\mathrm{a}}\,\delta_{ij}\Big)\Big\rangle\end{aligned} \tag{A.9f}$$

$$\begin{aligned}\Lambda_{ijk} = 14\pi\eta a^4\Big\langle \frac{1}{3}\Big(\epsilon_{i\alpha\beta}\, v_\alpha^{\mathrm{a}}\widehat{r}_\beta\widehat{r}_j\widehat{r}_k + \epsilon_{j\alpha\beta}\, v_\alpha^{\mathrm{a}}\widehat{r}_\beta\widehat{r}_k\widehat{r}_i + \epsilon_{k\alpha\beta}\, v_\alpha^{\mathrm{a}}\widehat{r}_\beta\widehat{r}_i\widehat{r}_j\Big)\\ + \frac{1}{5}\Big(\epsilon_{i\alpha\beta}\, v_\alpha^{\mathrm{a}}\widehat{r}_\beta\,\delta_{jk} + \epsilon_{j\alpha\beta}\, v_\alpha^{\mathrm{a}}\widehat{r}_\beta\,\delta_{ki} + \epsilon_{k\alpha\beta}\, v_\alpha^{\mathrm{a}}\widehat{r}_\beta\,\delta_{ij}\Big)\Big\rangle\end{aligned} \tag{A.9g}$$

The power dissipation relation, Eq. (5.30), is

$$\dot{W} = -\sum_{p=0}^{\infty} Q_{i\,\alpha_1\alpha_2\ldots\alpha_{p-1}\alpha_p}\mathcal{G}_{\alpha_p\alpha_{p-1}\ldots\alpha_2\alpha_1\,i,\,j\beta_1\beta_2\ldots\beta_{p-1}\beta_p}\, Q_{\beta_p\beta_{p-1}\ldots\beta_2\beta_1\,j} \tag{A.10}$$

Finally, the active stress tensor, Eq. (5.36), is

$$\begin{aligned}\sigma^a_{\alpha\beta}(\mathbf{r}) = \left(1 + \frac{a^2\nabla^2}{10}\right)S_{\alpha\beta} + \frac{1}{5}\nabla_\alpha d_\beta - \left(1 + \frac{a^2\nabla^2}{14}\right)\nabla_\nu\Gamma_{\alpha\beta\nu} + \frac{4}{3}\left(1 + \frac{a^2\nabla^2}{14}\right)\epsilon_{\alpha\beta\nu}\nabla_\mu\Upsilon_{\nu\mu}\\ - \frac{3}{4}\left(1 + \frac{a^2\nabla^2}{18}\right)\epsilon_{\alpha\beta\nu}\nabla_{\mu_1}\nabla_{\mu_2}\Lambda_{\nu\mu_1\mu_2}\end{aligned} \tag{A.11}$$

Bibliography

[1] D. Adams, *The Hitchhiker's Guide to the Galaxy*. Pan Macmillan, 2009.

[2] E. Schrödinger, *What is Life?: With Mind and Matter and Autobiographical Sketches*. A Canto Book Series, Cambridge University Press, 1992.

[3] L. Landau and E. Lifshitz, *Statistical Physics*. No. v. 5, Elsevier Science, 1996.

[4] A. Becskei and L. Serrano, "Engineering stability in gene networks by autoregulation," *Nature*, vol. 405, no. 6786, pp. 590–593, 2000.

[5] M. B. Elowitz, A. J. Levine, E. D. Siggia, and P. S. Swain, "Stochastic gene expression in a single cell," *Science*, vol. 297, no. 5584, pp. 1183–1186, 2002.

[6] J. Raser and E. O'Shea, "Noise in gene expression: origins, consequences, and control," *Science*, vol. 309, no. 5743, p. 2010, 2005.

[7] M. F. Wernet, E. O. Mazzoni, A. Çelik, D. M. Duncan, I. Duncan, and C. Desplan, "Stochastic spineless expression creates the retinal mosaic for colour vision," *Nature*, vol. 440, no. 7081, pp. 174–180, 2006.

[8] N. Q. Balaban, J. Merrin, R. Chait, L. Kowalik, and S. Leibler, "Bacterial persistence as a phenotypic switch," *Science*, vol. 305, no. 5690, pp. 1622–1625, 2004.

[9] M. Thattai and A. van Oudenaarden, "Intrinsic noise in gene regulatory networks," *Proceedings of the National Academy of Sciences*, vol. 98, no. 15, pp. 8614–8619, 2001.

[10] E. M. Ozbudak, M. Thattai, I. Kurtser, A. D. Grossman, and A. van Oudenaarden, "Regulation of noise in the expression of a single gene," *Nature genetics*, vol. 31, no. 1, pp. 69–73, 2002.

[11] A. Raj and A. van Oudenaarden, "Nature, nurture, or chance: stochastic gene expression and its consequences," *Cell*, vol. 135, no. 2, pp. 216–226, 2008.

[12] R. Benzi, A. Sutera, and A. Vulpiani, "The mechanism of stochastic resonance," *Journal of Physics A: mathematical and general*, vol. 14, no. 11, p. L453, 1981.

[13] L. Gammaitoni, P. Hänggi, P. Jung, and F. Marchesoni, "Stochastic resonance," *Reviews of modern physics*, vol. 70, no. 1, p. 223, 1998.

[14] J. M. Parrondo, C. Van den Broeck, J. Buceta, and F. J. de La Rubia, "Noise-induced spatial patterns," *Physica A: Statistical Mechanics and its Applications*, vol. 224, no. 1, pp. 153–161, 1996.

[15] A. J. McKane and T. J. Newman, "Predator-prey cycles from resonant amplification of demographic stochasticity," *Phys. Rev. Lett.*, vol. 94, p. 218102, 2005.

[16] F. J. Nédélec, T. Surrey, A. C. Maggs, and S. Leibler, "Self-organization of microtubules and motors," *Nature*, vol. 389, no. 6648, pp. 305–308, 1997.

[17] S. Camazine, J. L. Deneubourg, N. R. Franks, J. Sneyd, G. Theraulaz, and E. Bonabeau, *Self-organization in Biological Systems*. New York: Princeton University Press, 2003.

[18] W. F. Paxton, K. C. Kistler, C. C. Olmeda, A. Sen, S. K. S. Angelo, Y. Cao, T. E. Mallouk, P. E. Lammert, and V. H. Crespi, "Catalytic nanomotors: Autonomous movement of striped nanorods," *J. Am. Chem. Soc.*, vol. 126, no. 41, pp. 13424–13431, 2004.

[19] J. Vicario, R. Eelkema, W. R. Browne, A. Meetsma, R. M. La Crois, and B. L. Feringa, "Catalytic molecular motors: fuelling autonomous movement by a surface

bound synthetic manganese catalase," *Chem. Commun.*, vol. 31, pp. 3936–3938, 2005.

[20] G. A. Ozin, I. Manners, S. Fournier-Bidoz, and A. Arsenault, "Dream nanomachines," *Adv. Mater.*, vol. 17, no. 24, pp. 3011–3018, 2005.

[21] J. M. Catchmark, S. Subramanian, and A. Sen, "Directed rotational motion of microscale objects using interfacial tension gradients continually generated via catalytic reactions," *Small*, vol. 1, no. 2, pp. 202–206, 2005.

[22] J. G. Gibbs and Y. P. Zhao, "Autonomously motile catalytic nanomotors by bubble propulsion," *Appl. Phys. Lett.*, vol. 94, p. 163104, 2009.

[23] R. A. Simha and S. Ramaswamy, "Hydrodynamic Fluctuations and Instabilities in Ordered Suspensions of Self-Propelled Particles," *Phys. Rev. Lett.*, vol. 89, p. 058101, Jul 2002.

[24] L. H. Cisneros, R. Cortez, C. Dombrowski, R. E. Goldstein, and J. O. Kessler, "Fluid dynamics of self-propelled microorganisms, from individuals to concentrated populations," *Exp. Fluids*, vol. 43, no. 5, pp. 737–753, 2007.

[25] D. Saintillan and M. J. Shelley, "Instabilities and Pattern Formation in Active Particle Suspensions: Kinetic Theory and Continuum Simulations," *Phys. Rev. Lett.*, vol. 100, p. 178103, Apr 2008.

[26] T. Sanchez, D. Welch, D. Nicastro, and Z. Dogic, "Cilia-Like Beating of Active Microtubule Bundles," *Science*, vol. 333, no. 6041, p. 456, 2011.

[27] T. Sanchez, D. Chen, S. DeCamp, M. Heymann, and Z. Dogic, "Spontaneous motion in hierarchically assembled active matter," *Nature*, vol. 491, pp. 431–434, 2012.

[28] Y. Hatwalne, S. Ramaswamy, M. Rao, and R. A. Simha, "Rheology of Active-Particle Suspensions," *Phys. Rev. Lett.*, vol. 92, p. 118101, Mar 2004.

[29] M. Cates, S. Fielding, D. Marenduzzo, E. Orlandini, and J. Yeomans, "Shearing active gels close to the isotropic-nematic transition," *Physical review letters*, vol. 101, no. 6, p. 068102, 2008.

[30] R. Stratonovich, *Topics In The Theory Of Random Noise*. Mathematics and Its Applications, Gordon and Breach, 1963.

[31] N. G. van Kampen, *Stochastic processes in physics and chemistry*. Elsevier, 3 ed., 2007.

[32] A. Ramakrishnan, "Stochastic processes relating to particles distributed in a continuous infinity of states," *Math. Proc. Cambridge*, vol. 46, no. 04, pp. 595–602, 1950.

[33] L. Janossy, "On the absorption of a nucleon cascade," in *Proceedings of the Royal Irish Academy. Section A: Mathematical and Physical Sciences*, vol. 53, pp. 181–188, JSTOR, 1950.

[34] H. J. Bhabha, "On the stochastic theory of continuous parametric systems and its application to electron cascades," *Proc. Roy. Soc. A*, vol. 202, pp. 300–332, 1950.

[35] D. J. Daley and D. Vere-Jones, *An Introduction to the Theory of Point Processes*, vol. 1. New York: Springer, 2 ed., 2003.

[36] G. E. Uhlenbeck and L. S. Ornstein, "On the theory of the brownian motion," *Phys. Rev.*, vol. 36, no. 5, p. 823, 1930.

[37] C. W. Gardiner, *Handbook of stochastic methods for physics, chemistry and the natural sciences*. Springer, 3 ed., 2004.

[38] H. Risken, *The Fokker-Planck Equation: Methods of Solution and Applications*. Lecture Notes in Mathematics, Springer Berlin Heidelberg, 1996.

[39] J. L. Doob, "Markoff chains–denumerable case," *Transactions of the American Mathematical Society*, pp. 455–473, 1945.

[40] A. Kolmogoroff, "Über die analytischen methoden in der wahrscheinlichkeitsrechnung," *Mathematische Annalen*, vol. 104, no. 1, pp. 415–458, 1931.

[41] W. Feller, "On the integro-differential equations of purely discontinuous markoff processes," *Transactions of the American Mathematical Society*, vol. 48, no. 3, pp. 488–515, 1940.

[42] D. G. Kendall, "An artificial realization of a simple" birth-and-death" process," *Journal of the Royal Statistical Society. Series B (Methodological)*, vol. 12, no. 1, pp. 116–119, 1950.

[43] M. S. Bartlett, "Stochastic processes or the statistics of change," *Applied Statistics*, pp. 44–64, 1953.

[44] M. S. Bartlett, "Measles periodicity and community size," *J. R. Stat. Soc. A*, vol. 120, no. 1, pp. 48–70, 1957.

[45] D. T. Gillespie, "A general method for numerically simulating the stochastic time evolution of coupled chemical reactions," *J. Comput. Phys.*, vol. 22, no. 4, pp. 403–404, 1976.

[46] D. T. Gillespie, "Exact stochastic simulation of coupled chemical reactions," *J. Phys. Chem*, vol. 81, no. 25, pp. 2340–2361, 1977.

[47] L. Landau and E. Lifshitz, *Fluid Mechanics: Landau and Lifshitz: Course of Theoretical Physics*. No. v. 6, Elsevier Science, 2013.

[48] C. Pozrikidis, *Boundary Integral and Singularity Methods for Linearized Viscous Flow*. Cambridge: Cambridge University Press, 1992.

[49] O. Ladyzhenskaya, *The mathematical theory of viscous incompressible flow*. Mathematics and its applications, Gordon and Breach, 1969.

[50] S. Kim and S. Karrila, *Microhydrodynamics: Principles and Selected Applications*. Dover Civil and Mechanical Engineering Series, Dover Publications, 2005.

[51] C. A. Wurtz, "Sur la papaïne: contribution à l'histoire des ferments solubles," *Compt. Rend. Hebd. Acad. Sci. Paris*, vol. 91, pp. 787–791, 1880.

[52] C. O'Sullivan and F. Tompson, "Lx.-invertase: a contribution to the history of an enzyme or unorganised ferment," *J. Chem. Soc., Trans.*, vol. 57, pp. 834–931, 1890.

[53] A. Brown, "Enzyme action," *J. Chem. Soc.*, vol. 81, pp. 373–386, 1902.

[54] V. Henri, "Theorie generale de l'action de quelques diastases," *Compt. Rend. Hebd. Acad. Sci. Paris*, vol. 135, pp. 916–919, 1902.

[55] L. Michaelis and M. L. Menten, "Die kinetik der inwertin wirkung," *Biochem. Z*, vol. 49, pp. 333–369, 1913.

[56] L. Segel, "On the validity of the steady state assumption of enzyme kinetics," *B. Math. Biol.*, vol. 50, no. 6, pp. 579–593, 1988.

[57] L. Segel and M. Slemrod, "The quasi-steady-state assumption: a case study in perturbation," *SIAM Rev.*, vol. 31, pp. 446–477, 1989.

[58] K. R. Albe, M. H. Butler, and B. E. Wright, "Cellular concentrations of enzymes and their substrates," *J. Theor. Biol.*, vol. 143, no. 2, pp. 163–195, 1990.

[59] I. Tinoco, K. Sauer, J. C. Wang, and J. D. Puglisi, *Physical Chemistry: Principles and Applications in Biological Sciences*. New Jersey: Prentice Hall, 4 ed., 2002.

[60] S. Schnell and P. K. Maini, "A century of enzyme kinetics : Reliability of the *k_m* and *v_max* estimates," *Comments Theor. Biol.*, vol. 8, p. 169, 2003.

[61] E. McCullagh, J. Farlow, C. Fuller, J. Girard, J. Lipinski-Kruszka, D. Lu, T. Noriega, G. Rollins, R. Spitzer, M. Todhunter, and H. El-Samad, "Not all quiet on the noise front," *Nat. Chem. Biol.*, vol. 5, pp. 699–744, 2009.

[62] S. C. Kou, B. J. Cherayil, W. Min, B. P. English, and X. S. Xie, "Single-molecule Michaelis-Menten equations.," *J. Phys. Chem. B*, vol. 109, pp. 19068–81, 2005.

[63] B. P. English, W. Min, A. M. van Oijen, K. T. Lee, G. Luo, H. Sun, B. J. Cherayil, S. C. Kou, and X. S. Xie, "Ever-fluctuating single enzyme molecules: Michaelis-Menten equation revisited.," *Nat. Chem. Biol.*, vol. 2, pp. 87–94, Feb. 2006.

[64] S. Saha, S. Ghose, R. Adhikari, and A. Dua, "Nonrenewal statistics in the catalytic activity of enzyme molecules at mesoscopic concentrations," *Phys. Rev. Lett.*, vol. 107, p. 218301, Nov 2011.

[65] S. Saha, "Stochastic kinetics of enzymes and unimolecular gas-phase reactions," 2013.

[66] H. P. Lu, L. Xun, and X. S. Xie, "Single-molecule enzymatic dynamics," *Science*, vol. 282, pp. 1877–1882, Dec. 1998.

[67] L. Mandel, "Sub-poissonian photon statistics in resonance fluorescence," *Optics Letters*, vol. 4, no. 7, pp. 205–207, 1979.

[68] F. Soler, F. Rodriguez, and G. Zumofen, "Memory in the photon statistics of multilevel quantum systems," *Physical Review A*, vol. 78, no. 5, p. 053813, 2008.

[69] H. Paul, "Photon antibunching," *Rev. Mod. Phys.*, vol. 54, pp. 1061–1102, Oct 1982.

[70] A. F. Bartholomay, "A stochastic approach to statistical kinetics with application to enzyme kinetics," *Biochemistry*, vol. 1, no. 2, pp. 223–230, 1962.

[71] J. D. Murray, *Mathematical Biology: An introduction*, vol. 1. Springer, 3 ed., 2002.

[72] D. Bernoulli, "Essai d'une nouvelle analyse de la mortalité causée par la petite vérole, et des avantages de l'inoculation pour la prévenir," *Histoires et Mémoires de l'Académie Royale des Sciences de Paris*, pp. 1–45, 1760.

[73] W. O. Kermack and A. G. McKendrick, "A contribution to the mathematical theory of epidemics," *Proc. R. Soc. Lond. A*, vol. 115, pp. 700–721, 1927.

[74] M. Kuperman and G. Abramson, "Small world effect in an epidemiological model," *Phys. Rev. Lett.*, vol. 86, pp. 2909–2912, 2001.

[75] R. Pastor-Satorras and A. Vespignani, "Epidemic spreading in scale-free networks," *Phys. Rev. Lett.*, vol. 86, pp. 3200–3203, 2001.

[76] M. Keeling, "The implications of network structure for epidemic dynamics," *Theor. Popul. Biol.*, vol. 67, pp. 1–8, 2005.

[77] G. F. Raggett, "Modelling the Eyam plague," *Bull. Inst. Math. and its Applic.*, vol. 18, pp. 221–226, 1982.

[78] M. S. Bartlett, "Deterministic and stochastic models for recurrent epidemics," *Proc. Third Berkeley Symp. on Math. Statist. and Prob.*, vol. 4, pp. 81–109, 1956.

[79] H. E. Soper, "The interpretation of periodicity in disease prevalence," *J. R. Stat. Soc.*, vol. 92, pp. 34–61, 1929.

[80] E. B. Wilson and J. Worcester, "Damping of epidemic waves," *Proc. Natl. Acad. Sci.*, vol. 31, no. 9, pp. 294–298, 1945.

[81] R. M. Nisbet and W. S. C. Gurney, "A simple mechanism for population cycles," *Nature*, vol. 263, pp. 319–320, 1976.

[82] D. Alonso, A. J. McKane, and M. Pascual, "Stochastic amplification in epidemics," *J. R. Soc. Interface*, vol. 4, no. 14, pp. 575–582, 2007.

[83] G. Rozhnova and A. Nunes, "Fluctuations and oscillations in a simple epidemic model," *Phys. Rev. E*, vol. 79, p. 041922, 2009.

[84] R. M. Nisbet and W. S. C. Gurney, *Modelling fluctuating populations*. Wiley, 1982.

[85] A. S. Pikovsky and J. Kürths, "Coherence resonance in a noise-driven excitable system," *Phys. Rev. Lett.*, vol. 78, no. 5, pp. 775–778, 1997.

[86] R. C. Hilborn and J. D. Erwin, "Stochastic coherence in an oscillatory gene circuit model," *J. Theor. Biol.*, vol. 253, pp. 349–354, 2008.

[87] G. Giacomelli, M. Giudici, S. Balle, and J. R. Tredicce, "Experimental evidence of coherence resonance in an optical system," *Phys. Rev. Lett.*, vol. 84, no. 15, pp. 3298–3301, 2000.

[88] S. Barnett and C. Storey, "Stability analysis of constant linear systems by Lyapunov's second method," *Electron. Lett.*, vol. 2, pp. 165–166, 1966.

[89] M. Lax, "Fluctuations from the nonequilibrium steady state," *Rev. Mod. Phys.*, vol. 32, no. 1, pp. 25–43, 1960.

[90] T. Tomé, Á. L. Rodrigues, E. Arashiro, and M. J. de Oliveira, "The stochastic nature of predator–prey cycles," *Computer Physics Communications*, vol. 180, no. 4, pp. 536–539, 2009.

[91] K. Tomita and H. Tomita, "Irreversible circulation of fluctuations," *Prog. Theor. Phys.*, vol. 51, no. 6, pp. 1731–1749, 1974.

[92] P. J. Ioannou, "Nonnormality increases variance," *J. Atmos. Sci.*, vol. 52, no. 8, pp. 1155–1158, 1995.

[93] T. Pedley and J. Kessler, "Hydrodynamic phenomena in suspensions of swimming microorganisms," *Annu. Rev. Fluid Mech.*, vol. 24, no. 1, pp. 313–358, 1992.

[94] E. Lauga and T. Powers, "The hydrodynamics of swimming microorganisms," *Rep. Prog. Phys.*, vol. 72, no. 9, p. 096601, 2009.

[95] S. Ramaswamy, "The Mechanics and Statistics of Active Matter," *Annu. Rev. Condens. Mat. Phys.*, vol. 1, no. 1, pp. 323–345, 2010.

[96] M. Cates and F. MacKintosh, "Active soft matter," *Soft Matter*, vol. 7, no. 7, pp. 3050–3051, 2011.

[97] D. L. Koch and G. Subramanian, "Collective hydrodynamics of swimming microorganisms: Living fluids," *Annu. Rev. Fluid Mech.*, vol. 43, pp. 637–659, 2011.

[98] E. Lauga and R. Goldstein, "Dance of the microswimmers," *Phys. Today*, vol. 65, no. 9, pp. 30–35, 2012.

[99] M. C. Marchetti, J. F. Joanny, S. Ramaswamy, T. B. Liverpool, J. Prost, M. Rao, and R. A. Simha, "Hydrodynamics of soft active matter," *Rev. Mod. Phys.*, vol. 85, pp. 1143–1189, Jul 2013.

[100] G. Batchelor, "The stress system in a suspension of force-free particles," *J. Fluid Mech.*, vol. 41, no. 3, pp. 545–570, 1970.

[101] K. Drescher, K. C. Leptos, I. Tuval, T. Ishikawa, T. J. Pedley, and R. E. Goldstein, "Dancing volvox: Hydrodynamic bound states of swimming algae," *Phys. Rev. Lett.*, vol. 102, no. 16, p. 168101, 2009.

[102] J. S. Guasto, K. A. Johnson, and J. P. Gollub, "Oscillatory flows induced by microorganisms swimming in two dimensions," *Phys. Rev. Lett.*, vol. 105, no. 16, p. 168102, 2010.

[103] K. Drescher, R. Goldstein, N. Michel, M. Polin, and I. Tuval, "Direct measurement of the flow field around swimming microorganisms," *Phys. Rev. Lett.*, vol. 105, no. 16, p. 168101, 2010.

[104] M. J. Lighthill, "On the squirming motion of nearly spherical deformable bodies through liquids at very small reynolds numbers," *Commun. Pure. Appl. Math.*, vol. 5, no. 2, pp. 109–118, 1952.

[105] J. Blake, "A spherical envelope approach to ciliary propulsion," *J. Fluid Mech.*, vol. 46, no. 1, pp. 199–208, 1971.

[106] H. Lamb, *Hydrodynamics*. University Press, 1916.

[107] S. Hess and W. Köhler, *Formeln zur tensor-rechnung*. Palm & Enke, 1980.

[108] P. Mazur and W. Van Saarloos, "Many-sphere hydrodynamic interactions and mobilities in a suspension," *Physica A: Stat. Mech. Appl.*, vol. 115, no. 1, pp. 21–57, 1982.

[109] J. Coope, R. Snider, and F. McCourt, "Irreducible cartesian tensors," *J. Chem. Phys.*, vol. 43, p. 2269, 1965.

[110] J. Jerphagnon, "Invariants of the Third-Rank Cartesian Tensor: Optical Nonlinear Susceptibilities," *Phys. Rev. B*, vol. 2, no. 4, pp. 1091–1098, 1970.

[111] J. Jerphagnon, D. Chemla, and R. Bonneville, "The description of the physical properties of condensed matter using irreducible tensors," *Adv. Phys.*, vol. 27, no. 4, pp. 609–650, 1978.

[112] D. Andrews and W. Ghoul, "Irreducible fourth-rank cartesian tensors," *Phys. Rev. A*, vol. 25, no. 5, p. 2647, 1982.

[113] A. J. Ladd, "Hydrodynamic interactions in a suspension of spherical particles," *J. Chem. Phys.*, vol. 88, p. 5051, 1988.

[114] H. Brenner, "The stokes resistance of an arbitrary particle," *Chem. Engg. Sci.*, vol. 18, no. 1, pp. 1–25, 1963.

[115] J. Anderson and D. Prieve, "Diffusiophoresis caused by gradients of strongly adsorbing solutes," *Langmuir*, vol. 7, no. 2, pp. 403–406, 1991.

[116] H. A. Stone and A. D. T. Samuel, "Propulsion of microorganisms by surface distortions," *Phys. Rev. Lett.*, vol. 77, pp. 4102–4104, Nov 1996.

[117] B. Finlayson and L. Scriven, "Convective instability by active stress," *Proc. Roy. Soc. A*, vol. 310, no. 1501, pp. 183–219, 1969.

[118] R. A. Simha and S. Ramaswamy, "Statistical hydrodynamics of ordered suspensions of self-propelled particles: waves, giant number fluctuations and instabilities," *Physica A*, vol. 306, pp. 262–269, 2002.

[119] A. Leonov and V. Volkov, "General analysis of linear nematic elasticity," *Journal of Engineering Physics and Thermophysics*, vol. 77, no. 4, pp. 717–726, 2004.

[120] A. Leonov and V. Volkov, "Dissipative soft modes in viscous nematodynamics," *Rheologica acta*, vol. 44, no. 4, pp. 331–341, 2005.

[121] G. Jayaraman, S. Ramachandran, S. Ghose, A. Laskar, M. Saad Bhamla, P. B. Sunil Kumar, and R. Adhikari, "Autonomous Motility of Active Filaments due to Spontaneous Flow-Symmetry Breaking," *Phys. Rev. Lett.*, vol. 109, no. 15, p. 158302, 2012.

[122] A. Laskar, R. Singh, S. Ghose, G. Jayaraman, P. S. Kumar, and R. Adhikari, "Hydrodynamic instabilities provide a generic route to spontaneous biomimetic oscillations in chemomechanically active filaments," *Scientific reports*, vol. 3, 2013.

[123] T. L. Jahn and E. C. Bovee, "Movement and locomotion of microorganisms.," *Annu. Rev. Microbiol.*, vol. 19, no. 304, pp. 21–58, 1965.

[124] J. Gray, "The movement of sea-urchin spermatozoa," *J. Exp. Biol.*, vol. 32, no. 4, pp. 775–801, 1955.

[125] C. B. Lindemann and R. Rikmenspoel, "Sperm Flagella: Autonomous Oscillations of the Contractile System," *Science*, vol. 175, no. 4019, pp. 337–338, 1972.

[126] H. C. Berg and R. A. Anderson, "Bacteria Swim by Rotating their Flagellar Filaments," *Nature*, vol. 245, pp. 380–382, Oct. 1973.

[127] H. C. Berg, "The rotary motor of bacterial flagella," *Annu. Rev. Biochem.*, vol. 72, no. 1, p. 19, 2003.

[128] E. Purcell, "Life at low reynolds number," *Am. J. Phys*, vol. 45, no. 1, pp. 3–11, 1977.

[129] C. J. Brokaw, "Non-sinusoidal bending waves of sperm flagella," *J. Exp. Biol.*, vol. 43, no. 1, pp. 155–169, 1965.

[130] C. Brennen and H. Winet, "Fluid mechanics of propulsion by cilia and flagella," *Annu. Rev. Fluid Mech.*, vol. 9, no. 1, pp. 339–398, 1977.

[131] C. J. Brokaw, "Microtubule sliding in swimming sperm flagella: direct and indirect measurements on sea urchin and tunicate spermatozoa.," *J. Cell. Biol.*, vol. 114, no. 6, pp. 1201–15, 1991.

[132] M. Fujimura and M. Okuno, "Requirement of the fixed end for spontaneous beating in flagella.," *J. Exp. Biol.*, vol. 209, no. Pt 7, pp. 1336–43, 2006.

[133] S. Han, H. Benaroya, and T. Wei, "Dynamics of transversely vibrating beams using four engineering theories," *Journal of Sound and Vibration*, vol. 225, no. 5, pp. 935–988, 1999.

[134] M. C. Lagomarsino, I. Pagonabarraga, and C. P. Lowe, "Hydrodynamic induced deformation and orientation of a microscopic elastic filament," *Phys. Rev. Lett.*, vol. 94, no. 14, p. 148104, 2005.

[135] M. B. Elowitz and S. Leibler, "A synthetic oscillatory network of transcriptional regulators," *Nature*, vol. 403, no. 6767, pp. 335–338, 2000.

[136] J. F. Brady and G. Bossis, "Stokesian dynamics," *Annual review of fluid mechanics*, vol. 20, pp. 111–157, 1988.

[137] J. Blake, "A note on the image system for a stokeslet in a no-slip boundary," in *Proc. Camb. Phil. Soc*, vol. 70, pp. 303–310, Cambridge Univ Press, 1971.

[138] C. Beenakker, "The effective viscosity of a concentrated suspension of spheres (and its relation to diffusion)," *Physica A: Statistical Mechanics and its Applications*, vol. 128, no. 1, pp. 48–81, 1984.

[139] T. Ishikawa and T. Pedley, "The rheology of a semi-dilute suspension of swimming model micro-organisms," *Journal of Fluid Mechanics*, vol. 588, no. 1, pp. 399–435, 2007.

[140] A. J. Ladd, "Hydrodynamic screening in sedimenting suspensions of non-brownian spheres," *Physical review letters*, vol. 76, no. 8, p. 1392, 1996.

[141] A. Ladd, "Effects of container walls on the velocity fluctuations of sedimenting spheres," *Physical review letters*, vol. 88, no. 4, p. 048301, 2002.

[142] I. Asimov, *The Last Question*. 1956.